

Development of plasmonic
nanomaterial-based biosensors and
bioresponsive materials for diagnostics
and molecular-scale technologies

Roger Molto Pallares

Supervisors

Professor Nguyen T. K. Thanh

Professor Xiao Di Su

A thesis submitted to the University College London
for the degree of Doctor of Philosophy,
Department of Chemistry,
University College London
2016

Declaration of originality

“I, Roger Molto Pallares, declare in lieu of an oath that I have written this thesis myself and that I have not used any sources or resources other than stated for its preparation. I further declare that I have clearly indicated all direct and indirect quotations. This thesis has not been submitted elsewhere for examination purposes.”

August 2016

Roger Molto Pallares

*Per a la iaia,
per ser sempre un exemple.*

Abstract

Anisotropic metal nanoparticles have been successfully used in a wide range of biomedical applications, such as diagnostics and therapy, because of their unique optical and electronic properties. Even though there is a wide range of morphologies synthetically available, the understanding of the mechanism behind the anisotropic growth of the nanoparticles is still incomplete. Regarding their application in diagnostics, metallic nanoparticle-based biosensors are facing new challenges, such as the discovery of novel circulating cancer biomarkers (e.g. cell-free DNA), which require sensitivities that cannot be achieved by traditional approaches. The research of this thesis covers current challenges in three specific areas found in the interface between bio- and nanoscience.

(1) Colloidal synthesis, where a novel synthesis of gold nanorods (AuNRs) has been developed by the addition of Hofmeister salts into the growth solution. The thorough characterization of the surfactant micelles in the growth solution provided a better understanding of the role of the surfactant as symmetry breaking component in the anisotropic growth.

(2) Diagnostics and disease prevention, where two new metal nanoparticle-based biosensors have been developed. The first one exploits the control of a photoresponsive fluid over the dimensions of anisotropic gold nanoparticles for UV exposure sensing and erythema prediction, where the nanoparticles are synthesized and used for sensing purpose at the same time. The second one is a AuNR-based biosensor for circulating cell-free DNA with inverse sensitivity, *i.e.* the lower the analyte concentration, the higher the response intensity.

(3) Bio-inspired materials, where a hybrid system made of AuNR-DNA has been designed to study the sequence-specific binding between transcription factors and DNA. This system has been further expanded to build a versatile multi-logic gate platform, capable of performing six different logic operations. Finally, the use of alternative plasmonic nanomaterials for sensing and bio-inspired materials has also been explored.

Acknowledgements

I would like to use this opportunity to express my gratitude to all the people who helped me throughout the course of this thesis.

First of all, I would like to thank my main supervisors Professor Nguyen Thi Kim Thanh and Professor Su Xiao Di, as without their support this thesis could not have been done. They have acted not only as thesis supervisors but also as mentors, and for that I really thank them.

One of the main reasons I had such a wonderful time in London is because of my lab colleagues and friends at the Royal Institution. I would like to thank Cristina for her help in my early beginning for being kind assisting me in and out of the lab. I cannot forget my office colleagues with whom I shared memorable times: Paul, George, Richard, Lara and Liz. I would like to thank the members of the “other” office for the good moments we experienced together: Luke, Sam, Roxanne, Aziliz, Niall, Aans and Victoria. Kris deserves special thanks for bringing always positive energy (and sometimes cookies) to the lab. And also Steve, for his patience and support.

One of the wonderful aspects of this thesis was that I have been fortunate enough to perform half of my research in Singapore, where I shared my time with remarkable people. My colleagues at IMRE deserve special acknowledgment for welcoming and helping me adjust to the new country and culture: Moh Moh, Laura, Sian Yang, Yusong and Sen Wai. I would like to express my gratitude to Michel, Suo Hon and Hui Ru for their help with the TEM measurement; to Say Li and Axwell for their help with the cell-free DNA and for opening me the doors of the Genome Institute when I needed it; to Professor Lanry Yung and his team (Yan Shan, Ying...) for hosting me when the IMRE labs were closed. Special mention to my friends of the Tea-Bugs group: Aled, Ola, Ceilidh, Maggie, Lp, Jo, Hamid, Diana, Jester and Arran. Also, I would like to thank my friends from Ghana: Enock and Kwadwo.

Last but not least, I would like to express my deepest appreciation to my friends and family and especially my parents for their unconditional love and help throughout this time. Lastly, I would like to express my gratitude to my girlfriend Maria for being my strongest supporter in every part of this journey.

Thank you all.

Roger Molto Pallares
London, August 2016

Table of contents

Declaration of originality.....	3
Abstract	5
Acknowledgements.....	6
Table of contents	7
List of figures	12
List of tables	17
List of abbreviations.....	19
Chapter 1: Introduction	22
1.1 Noble metals in medicine.....	23
1.2 Localised surface plasmon resonance.....	24
1.3 Synthesis of MNPs	26
1.3.1 Spherical gold nanoparticles (AuNPs)	27
1.3.2 Gold nanorods (AuNRs)	27
1.3.3 Gold nanostars (AuNSs).....	28
1.3.4 Spherical silver nanoparticles (AgNPs).....	29
1.3.5 Gold (AuNCs) and silver nanoclusters (AgNCs).....	29
1.3.6 Others	30
1.4 Sensing applications.....	31
1.4.1 LSPR-based detection.....	31
1.4.1.1 Aggregation-based sensors	31
1.4.1.2 Refractive index sensors.....	32
1.4.2 Surface enhanced Raman spectroscopy (SERS) sensors	33
1.4.3 Fluorescence-based detection.....	34
1.4.3.1 Plasmon-resonance energy transfer (PRET) sensors	34
1.4.3.2 Metal-enhanced fluorescence sensors.....	35

1.5	MNPs in other bioresponsive technologies	36
1.6	Objectives	37
Chapter 2: Characterisation Techniques		39
2.1	UV-Vis spectroscopy	40
2.2	Fluorescence spectroscopy	41
2.2.1	Fluorescence polarisation.....	41
2.2.2	Sample preparation and measurements	41
2.3	X-ray diffraction (XRD) spectroscopy	42
2.4	Transmission electron microscopy (TEM)	43
2.4.1	High-resolution TEM (HR-TEM).....	44
2.4.2	Cryo-electron microscopy (cryo-TEM)	44
2.4.3	Sample preparation and imaging for TEM and HR-TEM.....	44
2.4.4	Sample preparation and imaging for cryo-TEM.....	44
2.5	Dynamic light scattering and zeta potential	46
2.5.1	Dynamic light scattering (DLS)	46
2.5.2	Zeta potential.....	46
2.5.3	Sample preparation and measurement.....	47
2.6	Capillary viscometer	48
Chapter 3: Fine-tuning of Gold Nanorod Dimensions and Plasmonic Properties Using the Hofmeister Effects		51
3.1	Introduction	52
3.2	Experimental section	54
3.2.1	Materials.....	54
3.2.2	Synthesis of AuNRs.....	54
3.2.3	Characterization	55
3.3	Results and discussion	56
3.3.1	Tuning the L-LSPR band.....	56

3.3.2	Morphology and crystalline structure of the AuNRs	57
3.3.3	Evolution of CTAB micelles	61
3.3.4	Growth mechanism.....	64
3.4	Conclusions.....	68
3.5	Annex	69
Chapter 4: Growth of Anisotropic Gold Nanoparticles in Photoresponsive Fluid for UV Exposure Sensing and Erythema Prediction		72
4.1	Introduction	73
4.2	Experimental section	76
4.2.1	Materials.....	76
4.2.2	Sample irradiation.....	76
4.2.3	Synthesis of AuNRs.....	76
4.2.4	Synthesis of AuNWs.....	77
4.2.5	Simulated sunlight calculations.....	77
4.2.6	Characterization	78
4.3	Results and discussion	79
4.3.1	Growth of AuNRs.....	79
4.3.2	Growth of AuNWs.....	83
4.3.3	Insights into the growth mechanism and the role of OMCA.....	86
4.3.4	In situ growth sensing of UV radiant exposure for erythema prevention...	91
4.4	Conclusions.....	94
4.5	Annex	95
Chapter 5: An Enzyme-free Plasmonic Nanosensor with Inverse Sensitivity for Circulating Cell-free DNA Quantification		98
5.1	Introduction	99
5.2	Experimental section	101
5.2.2	Characterization	101
5.2.3	Synthesis of AuNRs.....	102

5.2.4	Colorimetric detection of dsDNA	102
5.2.5	Fluorescence assays	102
5.3	Results and discussion	103
5.3.1	Inverse response	103
5.3.2	Mechanism behind the inverse sensitivity	105
5.3.3	Tuning the dynamic range	108
5.4	Conclusions.....	111
Chapter 6: Plasmonic Multi-logic Gate Platform Based on Sequence-specific Binding of Transcription Factors and Gold Nanorods		113
6.1	Introduction	114
6.2	Experimental section	116
6.2.1	Materials.....	116
6.2.2	Characterization	116
6.2.3	Synthesis of AuNRs.....	116
6.2.4	Determination of metallic Au concentration.....	117
6.2.5	AuNRs aggregation by dsDNA	117
6.2.6	Protein-dsDNA binding assays	117
6.3	Results and discussion	119
6.3.1	Combination of AuNRs and dsDNA	119
6.3.2	Characterization of protein-dsDNA binding	121
6.3.3	Building a multi-logic gate platform	123
6.4	Conclusions.....	126
6.5	Annex	127
Chapter 7: Hybrid Bioassay Based on Graphene Oxide and Conjugated Polyelectrolytes for Studying Protein-DNA Interactions.....		130
7.1	Introduction	131
7.2	Experimental section	133
7.2.1	Materials.....	133

7.2.2	Characterization	133
7.2.3	CPE fluorescence quenching by GO in the presence of dsDNA	134
7.2.4	Protein-DNA binding assay.....	134
7.2.5	Assay for fluorescence polarisation measurement.....	134
7.3	Results and discussion	135
7.3.1	Fluorescence quenching and recovery between GO and CPE in the absence and presence of dsDNA.....	135
7.3.2	Fluorescence quenching promoted by protein-DNA binding	137
7.4	Conclusions.....	141
Chapter 8: Conclusions and Future Work.....		143
8.1	Conclusions.....	144
8.2	Future work.....	146
Appendix: Publications, contributions to conferences and awards		148
Bibliography.....		150

List of figures

<i>Figure</i>	<i>Description</i>	<i>Page</i>
Fig. 1.1	Schematic representation of electron collective oscillation with incident electromagnetic field.	24
Fig. 1.2	Simulation of electromagnetic field (V/m) for (a) single gold nanoparticle and (b) gold nanoparticle dimer with incident 633 nm wavelength light. (c) Dimer gap distance dependency of field enhancement.	25
Fig. 1.3	TEM images and absorbance spectra of polymer-coated gold nanoparticles with (a) spherical, (b) rod and (c) star morphology.	26
Fig. 1.4	Calculated normalized absorption (γ/NV) spectra of gold nanorods (elongated ellipsoids) with different aspect ratios (R) and dielectric constant of the medium of 2.05.	28
Fig. 1.5	(a) Scheme of analyte-triggered gold nanoparticle aggregation and (b) its corresponding change on the nanoparticle optical properties. (c) Scheme of the analyte binding to gold nanoparticles and (d) change on the differential extinction spectra at 600 nm, due to the variation of the dielectric constant of the nanoparticle surroundings.	32
Fig. 1.6	Scheme of molecular beacon exploiting PRET principle for DNA sensing.	35
Fig. 2.1	Schematic electron path and main components in a TEM.	43
Fig. 2.2	Schematic Cannon-Fenske viscometer.	49
Fig. 3.1	Normalized extinction spectra of AuNRs grown in the presence of additional amount of Hofmeister salts. For (a), (b) and (c) the salt concentrations are 0 mM (blue), 10 mM (red), 20 mM (green), 30 mM (purple), 40 mM (turquoise) and 50 mM (orange) from bottom to top. For (d), the salt concentrations are 0 mM (blue), 5 mM (red), 10 mM (green), 15 mM (purple), 20 mM (turquoise), 25 mM (orange) and 30 mM (grey) from bottom to top. All the spectra have been offset for easier comprehension.	57
Fig. 3.2	TEM images of AuNRs synthesized using our seed-mediated method with different amounts of Hofmeister salts: (a) without Hofmeister salts. (b - f) with NaNO_3 , (g - k) with NaCl and (l - p) with NaHSO_4 in order of increasing added concentration (10 - 50 mM). (q - v) with NaBr in order of increasing added concentration (5 - 30 mM). All scale bars are 50 nm.	58

Fig. 3.3	HR-TEM images of AuNRs synthesized (a) without Hofmeister salts, (b) with NaNO ₃ (50 mM), (c) with NaCl (50 mM), (d) with NaHSO ₄ (50 mM) and (e) with NaBr (30 mM). The insets in the images are the fast Fourier transform patterns of the selected regions. All scale bars are 5 nm.	60
Fig. 3.4	XRD diffraction pattern of AuNRs obtained with and without added Hofmeister salts.	60
Fig. 3.5	(a) Zeta potential, (b) hydrodynamic diameter and (c) relative viscosity of growth solutions in the presence of added Hofmeister salts.	61
Fig. 3.6	Cryo-TEM images of CTAB micelles in the growth solutions with different amounts of Hofmeister salts: (a) without Hofmeister salts. (b and c) with NaNO ₃ , (d and e) with NaCl and (f and g) with NaHSO ₄ in order of increasing added concentration (30 and 50 mM). Some ellipsoidal and rod-like micelles have been highlighted in red and white dashed circles, respectively. All scale bars are 50 nm.	63
Fig. 3.7	Micelle shape distribution (spherical, ellipsoidal and rod-like micelle) in growth solutions at different Hofmeister salt concentrations and the L-LSPR _{max} of the rods grown in those solutions.	63
Fig. 3.8	Micelle zeta potential (circle) after the addition of Hofmeister salts in the growth solution and percentage of shape impurities (diamond) after the growth of the rods in those solutions. The moving averages of both zeta potentials and impurities are represented in solid and dashed lines, respectively.	66
Fig. 4.1	Photoisomerization of OMCA from <i>trans</i> to <i>cis</i> form.	79
Fig. 4.2	(A) TEM images of AuNRs grown in the photoresponsive fluid after UV irradiation for (a) 0, (b) 1, (c) 2.5, (d) 5, (e) 10 and (f) 15 min. AuNR aspect ratios are displayed below the TEM images. Scale bars represent 50 nm. (B) Plot of the length and width of the grown AuNRs. (C) Corresponding absorbance spectra of the AuNRs. (D) Variation of the ratio between the AuNR longitudinal (A _L) and transversal (A _T) LSPR bands as a function of UV exposure time.	80
Fig. 4.3	(A) Absorbance spectra of the AuNRs grown in the photoresponsive fluid over the time. (B) Correlation between the intensity ratio of the AuNR longitudinal (A _L) and transversal (A _T) LSPR bands with reaction time in the presence (blue) and absence (red) of 5 mM <i>trans</i> -OMCA. The UV irradiation time is 0 min. (C) Variation of Au ³⁺ absorbance ratio at 450 and 600 nm, as a function of time in the presence of (blue) <i>cis</i> -OMCA or (red) <i>trans</i> -OMCA under AuNR growth conditions.	81
Fig. 4.4	(A) HR-TEM image of AuNRs synthesized in the photoresponsive fluid. The inset in the image is the fast Fourier transform pattern of the selected region. Scale bar represents 5 nm. (B) XRD pattern of AuNRs obtained in the photoresponsive fluid. Asterisk denotes a substrate peak (Si (444)). The UV irradiation time is 0 min.	82

Fig. 4.5	(A) TEM images of AuNWs grown in the photoresponsive fluid after (a) 0, (b) 1, (c) 2.5, (d) 5, (e) 10 and (f) 15 min of UV irradiation. AuNW aspect ratios are displayed below the TEM images. Scale bars represent 100 nm. (B) Plot of the length and width of grown AuNWs. (C) Absorbance spectra of AuNWs grown in the photoresponsive fluid after 0, 1, 2.5, 5, 10 and 15 min of UV irradiation.	83
Fig. 4.6	(A) Absorbance spectra of the AuNWs grown in the photoresponsive fluid over the time (from 0 to 100 min). (B) Correlation between the absorbance intensity at 975 nm against reaction time. The two phases of AuNW growth, <i>i.e.</i> fast formation of the plasmon bands and their slow increase, are highlighted in blue and green, respectively. The UV irradiation time is 0 min. (C) Variation of Au ³⁺ absorbance ratio at 450 and 600 nm, as a function of time in the presence of (blue) <i>cis</i> -OMCA or (red) <i>trans</i> -OMCA under AuNW growth conditions.	84
Fig. 4.7	(A) TEM image of the AuNWs. The circles highlight the areas of different domains. Scale bar represents 10 nm. (B) HR-TEM image of AuNW with different atomic lattice directions highlighted in white. Scale bar represents 10 nm. (C) HR-TEM image of AuNWs synthesized in the photoresponsive fluid. The inset in the image is the fast Fourier transform pattern of the AuNW. Scale bar represents 5 nm. (D) XRD pattern of AuNWs obtained in the photoresponsive fluid. The UV irradiation time is 0 min.	85
Fig. 4.8	(A) Absorbance spectra of <i>trans</i> -OMCA (in a solution made of 100 mM CTAB and 5 mM <i>trans</i> -OMCA) after being irradiated with UV light for 0, 1, 2.5, 5, 10 and 15 min. The spectrum of <i>cis</i> -OMCA (dashed line) is plotted for reference. (B) Absorbance spectra of 1 mM <i>trans</i> -OMCA (purple) and <i>cis</i> -OMCA (red), and their pH.	86
Fig. 4.9	(A) FTIR spectra of <i>cis</i> -OMCA and <i>trans</i> -OMCA after being irradiated with UV light for 0, 5, 10 or 15 min. (B) ¹ H-NMR spectra of <i>cis</i> -OMCA and <i>trans</i> -OMCA before and after being irradiated for 15 min in DMSO-d ₆ .	87
Fig. 4.10	Spectra of erythral response function (green), sun irradiance at earth's surface (orange), biologically active UV radiation (purple) and <i>trans</i> -OMCA absorbance (blue).	92
Fig. 4.11	(A) Absorbance spectra of AuNRs grown in the photoresponsive fluid after 0, 20, 40, 60 and 80 min of solar simulated irradiation. (B) Variation of the ratio between the AuNR longitudinal (A _L) and transversal (A _T) LSPR bands as a function of non-weighted UV radiant exposure and standard erythral dose. The graph is divided in areas based on the exposure biological effect: harmless exposures (green) and erythema-causing exposures to skin type I (orange), type II (pink), type III (red) and type IV (dark red).	93
Fig. 5.1	Scheme of the response curves of sensors with (A) inverse sensitivity, (B) inversely proportional response and (C) directly proportional response. This scheme has been drawn for clarification purposes and it has not been made from real data.	100

Fig. 5.2	Characterization of AuNRs ($OD_{890} = 0.48$), mixed with different amounts of dsDNA (180bp) in 8 mM Tris buffer. (A) UV-Vis spectra at 0 nM (dashed line), 2, 5, 10, 20 and 40 nM DNA (solid lines). (B) Absorbance ratio intensities at 510 and 890 nm as the function of DNA concentration. The lower and higher concentration regimes are highlighted in green and blue, respectively.	104
Fig. 5.3	Characterization of AuNR aggregation and disaggregation induced by dsDNA. TEM images at dsDNA concentrations of (A) 0, (B) 2, (C) 10 and (D) 20 nM. All scale bars are 50 nm. (E) Measures of AuNR hydrodynamic radius at 0, 2 and 10 nM dsDNA by DLS. The radius distributions have been offset vertically for clarity.	105
Fig. 5.4	Comparison between the effect of dsDNA concentration on the AuNR zeta potential (red) and the A_{510}/A_{890} (blue). The region of concentrations with higher AuNR aggregation is highlighted in pale blue.	105
Fig. 5.5	Excitation and emission spectra of dsDNA-TO ₄₀ (5 nM). Excitation wavelength: 450 nM. Emission wavelength: 600 nm.	106
Fig. 5.6	(A) Fluorescence emission of dsDNA-TO ₄₀ solutions in the absence and presence of AuNRs ($OD_{890} = 0.48$), respectively. (B) Emission intensities of different dsDNA-TO ₄₀ solutions at emission wavelength of 535 nm in the absence (orange) and presence (purple) of AuNRs. (C) Comparison between the fluorescence emission of dsDNA-TO ₄₀ in the presence of AuNR and their aggregation profile. All measures were done with an excitation wavelength of 490 nm.	107
Fig. 5.7	Effect of the dsDNA concentration on the A_{510}/A_{890} of five AuNR solutions. AuNR OD_{890} of 0.05 (turquoise), 0.08 (purple), 0.22 (green), 0.48 (red) and 0.92 (blue).	108
Fig. 6.1	Schematic illustration of one of the logic gates, <i>i.e.</i> OR, performed by the multi-logic gate design. OR logic gate is built by combining dsDNA-AuNRs and ERs, exploiting sequence-specific interactions between ERs and dsDNA.	115
Fig. 6.2	TEM image of AuNRs used in the protein-DNA binding assays. AuNR dimensions are $42.6 (\pm 10.0) \times 10.4 (\pm 1.2)$ nm with aspect ratio of $4.1 (\pm 0.8)$.	119
Fig. 6.3	Characterization of AuNRs mixed with different amounts of dsDNA. (A) UV-Vis spectra of the AuNRs in the presence of 0, 5, 10 and 20 nM DNA. (B) UV-Vis spectra in the presence of 30, 40, 50, 75 and 100 nM DNA. (C) Absorbance intensity ratio at 510 and 885 nm as function of DNA concentration. The lower and higher concentration regimes are highlighted in blue and red, respectively. 10 nM at the lower concentration regime and 75 nM at the higher concentration regime are indicated because these two concentrations are used in the protein-DNA binding characterization experiments.	120
Fig. 6.4	(Red) hydrodynamic diameter (D_H) measured by DLS and (blue) zeta potential of AuNRs as a function of dsDNA concentration. The area with higher AuNR	120

aggregation is highlighted in pale-orange.

Fig. 6.5	Variation of dsDNA-AuNR absorbance ratio intensities at 510 and 885 nm after addition of Tris buffer over time. The volumes of Tris added into the system are the same as the ones added in the protein-dsDNA binding assays, <i>i.e.</i> 4 μ L of 12.5 mM Tris and 6.5 μ L of 50 mM Tris at 10 and 75 nM dsDNA, respectively.	121
Fig. 6.6	AuNR absorbance intensity ratio at 510 and 885 nm as function of ER α concentration at (A) 10 and (B) 75 nM dsDNA.	122
Fig. 6.7	AuNR absorbance ratio intensities at 510 and 885 nm as function of ER β concentration at 10 nM dsDNA.	122
Fig. 6.8	AuNR absorbance ratio intensities at 510 and 885 nm as function of Lysozyme concentration in the presence of dsDNA of (blue) 10 nM and (red) 75 nM.	123
Fig. 6.9	AuNR absorbance ratio intensities at 510 and 885 nm as function of different inputs in (A) OR, (B) NOT, (C) A IMPLY B, (D) BUFFER, (E) TRUE, and (F) FALSE logic gates.	125
Fig. 7.1	Chemical structures of (A) CCPE and (B) ACPE. Emission spectra of (C) CCPE and (ACPE) in the presence (red line) or absence (blue line) of GO.	135
Fig. 7.2	Emission spectra of (A) CCPE and (B) ACPE in the presence of GO and different dsDNA concentrations (<i>i.e.</i> 0, 1, 5, 10, 25, 50, 100, 250, 500 and 1000 nM). (C) Fluorescence variation of CCPE (λ_{max} of 410 nm) and ACPE (λ_{max} of 420 nm) in the presence of GO and different dsDNA concentrations.	136
Fig. 7.3	Zeta potential of GO and CCPE in the presence of different dsDNA concentrations (<i>i.e.</i> 0, 5, 10, 25, 50 and 100 nM).	137
Fig. 7.4	Three step analytical assay based on CCPE and GO for protein-DNA interaction characterization.	138
Fig. 7.5	Emission spectra of CCPE in the presence of GO, dsDNA and different protein concentrations (<i>i.e.</i> 0, 50, 100, 150, 200, 250, 300 and 350 nM). The three proteins added into the assay solution are (A) ER α , (B) FoxA1 and (C) AP-2 γ . (D) Fluorescence variation of CCPE (λ_{max} of 410 nm) in the presence of GO, dsDNA and different protein concentrations.	139
Fig. 7.6	Fluorescence polarisation of FAM-labelled dsDNA in the presence and absence of CCPE, ER α and BSA.	140

List of tables

<i>Table</i>	<i>Description</i>	<i>Page</i>
Table 3.1	Summary of the optical and morphological properties of AuNRs synthesized after the addition of Hofmeister salts into the growth solution.	59
Table 3.2	Summary of the morphological properties of CTAB micelles after the addition of Hofmeister salts into the growth solution. The three micelle morphologies observed by cryo-TEM are spherical (Sph.), ellipsoidal (Ellip.) and rod-shaped (rod).	64
Table S3.1	p -values obtained by Welch t-test (unequal variances t-test), to study if the differences between aspect ratios are statistical significant. The Hofmeister salts have been abbreviated as B (NaBr), N (NaNO ₃), C (NaCl) and S (NaHSO ₄). The number next to the salt is the concentration (mM) added to the growth solution.	69
Table S3.2	Cohen's d -values calculated to study the standardised differences between aspect ratios. The Hofmeister salts have been abbreviated as B (NaBr), N (NaNO ₃), C (NaCl) and S (NaHSO ₄). The number next to the salt is the concentration (mM) added to the growth solution.	70
Table 4.1	¹ H Chemical shifts (δ , ppm) of <i>trans</i> and <i>cis</i> -OMCA in DMSO-d ₆ .	88
Table 4.2	Growth solution pH after UV irradiation.	89
Table 4.3	Hydrodynamic diameter (D_H) of CTAB micelles after UV irradiation.	90
Table 4.4	Parameters affecting the nanoparticle aspect ratio.	91
Table S4.1	p -values obtained by Welch t-test (unequal variances t-test), to study if the differences between AuNR aspect ratios are statistical significant.	95
Table S4.2	Cohen's d -values calculated to study the standardised differences between AuNR aspect ratios.	95
Table S4.3	p -values obtained by Welch t-test (unequal variances t-test), to study if the differences between AuNW aspect ratios are statistical significant.	96
Table S4.4	Cohen's d -values calculated to study the standardised differences between AuNW aspect ratios.	96
Table 5.1	Oligonucleotides sequences	101

Table 5.2	Dynamic ranges of different AuNR solutions and their equivalence for an original 25 μL sample. The dynamic ranges from an original 25 μL sample are compared with several reference values from cancer patients.	110
Table S6.1	p -values obtained by one-sample Student's t -test, to study if the differences between the A_{510}/A_{885} ratios from the logic gate experiments and the reference values are statistical significant.	127
Table S6.2	p -values obtained by Welch t -test (unequal variances t -test), to study if the differences between the A_{510}/A_{885} ratios from the logic 0 and 1 values are statistical significant.	128
Table S6.3	Cohen's d -values calculated to study the standardised differences between the A_{510}/A_{885} ratios from the logic 0 and 1 values.	128
Table 7.1	Oligonucleotides sequences	133

List of abbreviations

6FAM	6-Carboxyfluorescein
ACPE	Anionic conjugated polyelectrolyte
AgNC	Silver nanocluster
AgNP	Silver nanoparticle
AP-2γ	Activating enhancer binding protein 2 gamma
AR	Aspect ratio
AuNC	Gold nanocluster
AuNP	Gold nanoparticle
AuNR	Gold nanorod
AuNS	Gold nanostar
AuNW	Gold nanoworm
BSA	Bovine serum albumin
cfDNA	Cell-free DNA
Cryo-TEM	Cryo-transmission electron microscopy
CCPE	Cationic conjugated polyelectrolyte
CPE	Conjugated polyelectrolyte
CTAB	Hexadecyltrimethylammonium bromide
D_H	Hydrodynamic diameter
DLS	Dynamic light scattering
DMF	N,N-dimethylformamide
DMSO-d₆	Deuterated dimethyl sulfoxide
DNA	Deoxyribonucleic acid
dsDNA	Double stranded DNA
ER	Estrogen receptor
ERE	Estrogen receptor element

FFT	Fast Fourier transform
FoxA1	Forkhead boxA1
FP	Fluorescence polarisation
FRET	Förster resonance energy transfer
FTIR	Fourier transform infrared
GO	Graphene oxide
His-MBP	Hexahistidine-tagged maltose-binding protein
HR-TEM	High-resolution TEM
IR	Infrared
K_d	Dissociation constant
LOD	Limit of detection
LSPR	Localised surface plasmon resonance
L-LSPR	Longitudinal LSPR
MED	Minimal erythematous dose
MNC	Metal nanocluster
MNP	Metal nanoparticle
NMR	Nuclear magnetic resonance
OMCA	ortho-methoxycinnamic acid
PEG	Polyethylene glycol
PRET	Plasmon-resonance energy transfer
PVP	Poly(vinylpyrrolidone)
SED	Standard erythematous dose
SERS	Surface enhanced Raman spectroscopy
SNR	Signal-to-noise ratio
SPR	Surface plasmon resonance
ssDNA	Single stranded DNA
TEM	Transmission electron microscopy

TO	Thiazole orange
UV	Ultraviolet
UVR	UV radiation
XRD	X-ray diffraction

Chapter 1

Introduction

A general introduction to the properties of noble metal nanoparticles, the synthesis of different nanoparticle morphologies, their applications in sensing and bioresponsive materials and the aim of this thesis are given in this chapter.

1.1 Noble metals in medicine

Noble metals have been used in medicine through the history of civilization.^{1,2} For instance, Egyptians were already using gold in dentistry around 4500 years ago,³ Persians used to stock clean water in silver containers in order to avoid contamination⁴ and the Hippocratic corpus, *i.e.* an ancient medical Greek book written in 5th century B.C., described the use of wire gold in jaw fractures.⁵

The modern use of gold and silver in medicine started in the last decade of 19th century, when Dr Koch proved that gold cyanide could be used to inhibit the growth of tuberculosis bacillus *in vitro*.⁶ Nevertheless, only after Dr Møllgaard's *in vivo* studies in the 20s,⁷ the antibacterial capacities of gold salts were fully accepted.⁸ Short after Møllgaard works were published, gold salts and colloid solutions were discovered to be effective against rheumatoid arthritis.^{9,10} Even though the exact mechanism of action is still unknown, these solutions remain being used for arthritis and other inflammatory disease treatment.¹¹

The important progress in colloidal and surface chemistry during the past couple decades has result on a significant volume of basic and applied research of metal nanoparticles.^{12,13} Those present size-related optical and electronic properties¹⁴ and a wide-range of applications,¹² from photonics to bioscience. In the last years, gold and silver nanoparticles have become building blocks for a new generation of analytical and medical technologies,^{15,16} which can play a key role in the next biomedical revolution.

1.2 Localised surface plasmon resonance

The unique optical and electronic properties of metal nanoparticles (MNP) are the result of the collective oscillation of the conduction band electrons when perturbed by an external electromagnetic radiation.¹⁷ This pushes away the electron cloud from its equilibrium position, inducing a surface polarization that promotes the oscillating movement and restores the system's equilibrium (Fig. 1.1). This phenomenon occurs at very specific light frequencies and it is called localised surface plasmon resonance (LSPR).¹⁸ The first quantitative explanation of LSPR appeared in 1908, when Gustav Mie solved Maxwell's electromagnetic equations for small spherical gold particles.¹⁹ Despite that pioneer work, the interest for the unusual optical properties of MNP did not reach widespread popularity until two decades ago, when different morphologies were finally accessible through newly developed synthetic techniques.^{20,21} That new colloid chemistry combined with computing improvements, provided a deeper understanding and refreshed interest on the interaction between MNP and light.

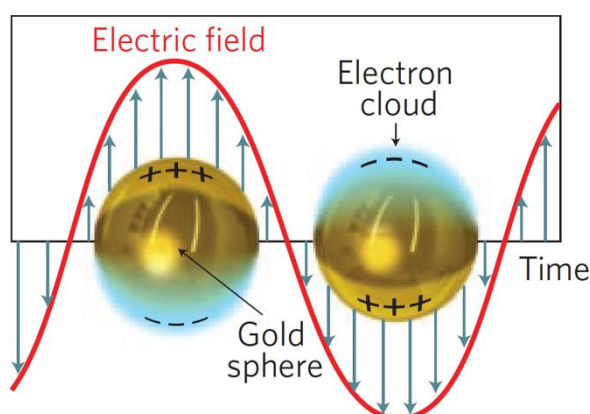


Fig. 1.1. Schematic representation of electron collective oscillation with incident electromagnetic field.²²

The LSPR is sensitive to many parameters, such as size and shape of the nanoparticle,²³ refractive index of the surrounding medium,²⁴ ligands on the surface,²⁵ temperature,²⁶ and interparticle distance.^{27,28} Depending on the nanoparticle's size and shape, the energy of excited plasmons is released by radiative (*i.e.* scattering of light) or non-radiative paths.²⁹ The non-radiative paths include the production of heat, if the nanoparticle is isolated, or electron transfer to adsorbed entities (*e.g.* doping of semiconductors).

Strong far- and near-field effects are produced when the plasmon is excited. The first defines the extinction, scattering and absorption cross section of the nanoparticles. The later affects the surface close vicinity, changing the way particles interact with nearby molecules or other particles. Those near-field effects are widely used in several

analytical techniques, such as surface enhanced Raman spectroscopy (SERS)³⁰ or fluorescence enhancement.³¹ The plasmon fields in nanoparticles are more sensitive to distance (*i.e.* they scale as $1/r^3$, where r is distance from the metal surface) than in bulk metal (*i.e.* scale as $1/r$).³² This strong distance-dependency confines the electromagnetic field around the nanoparticle, becoming a very localised and high-density phenomenon (Fig. 1.2a). When two nanoparticles are placed in close proximity (*i.e.* distances below half nanoparticle diameter) their LSPR couple, changing the behaviour of the plasmon and producing hot spots in the nanoparticle gap (Fig. 1.2b and Fig.1.2c).³³ The stronger electromagnetic field in the nanogap can be used in different ways, such as obtaining more intense Raman scattering signals, which can reach single-molecule sensitivity.³⁴

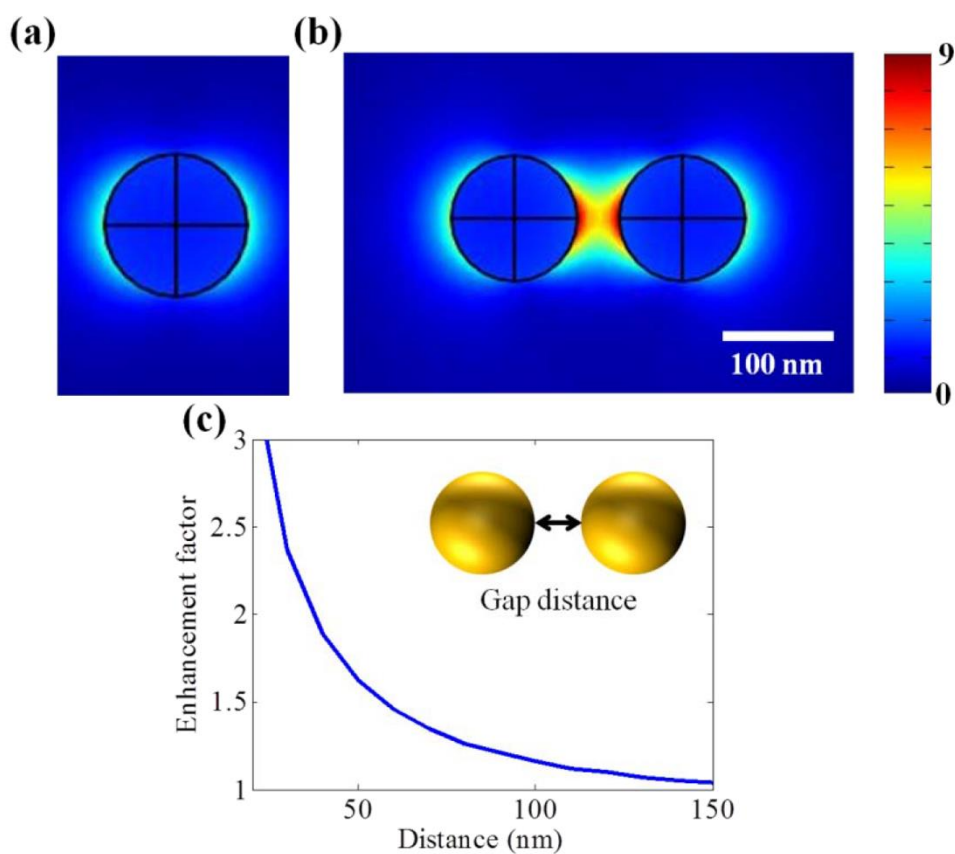


Fig. 1.2. Simulation of electromagnetic field (V/m) for (a) single gold nanoparticle and (b) gold nanoparticle dimer with incident 633 nm wavelength light. (c) Dimer gap distance dependency of field enhancement.³⁵

1.3 Synthesis of MNPs

Gold, silver and copper are attractive candidates for optical technologies because their LSPR band is found in the visible region, in comparison to transition metals, whose plasmon band lies in the UV region.³⁶ Nevertheless, since copper is easily oxidized,³⁷ most MNP work has been focused on gold and silver.

The most common strategy in the synthesis of MNP is the salt-reduction. In this approach, a soluble metal salt is reduced by a reducing agent in the presence of a stabilizing component, which tailors the growth of the crystal and prevents from aggregation and precipitation.

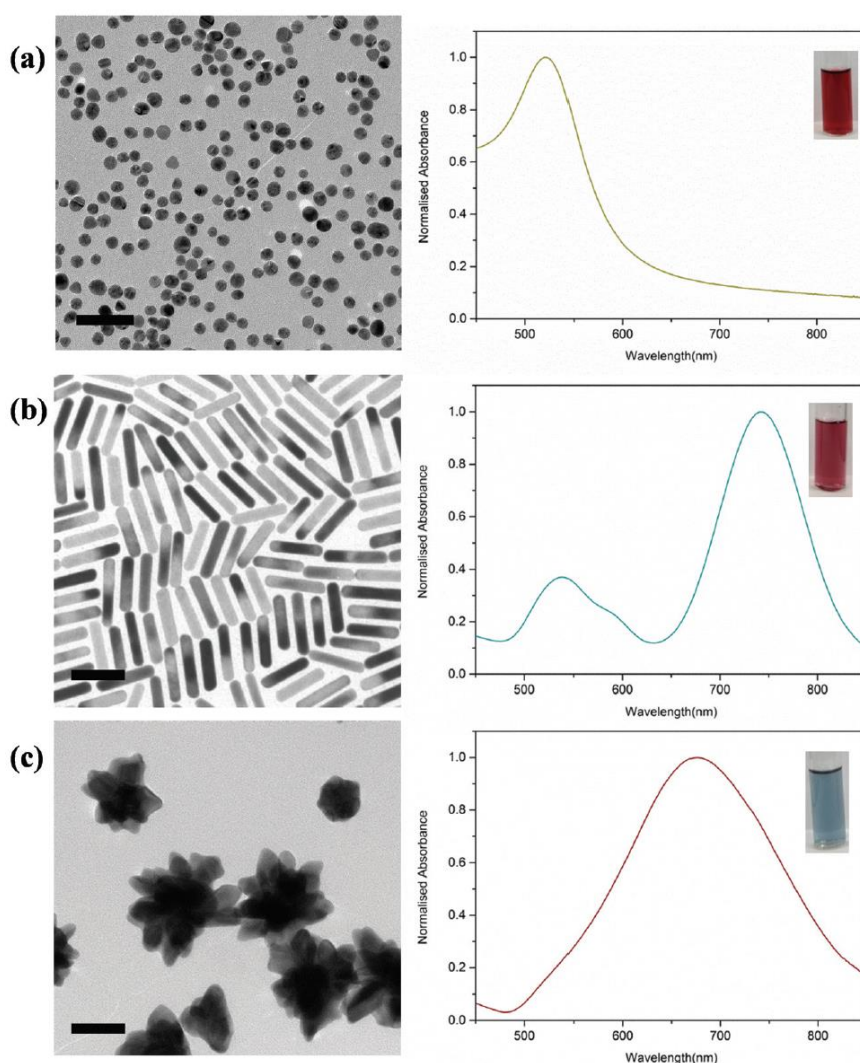


Fig. 1.3. TEM images and absorbance spectra of polymer-coated gold nanoparticles with (a) spherical, (b) rod and (c) star morphology.³⁸

Gold nanoparticles of various shapes (Fig. 1.3) are extensively used in nanosciences due to their reliable syntheses with high control over shape and size, high surface-to-volume ratio and easy functionalization.¹⁵

1.3.1 Spherical gold nanoparticles (AuNPs)

Spherical AuNPs are frequently obtained through Turkevich method.³⁹ In this, Au³⁺ salts are reduced to Au⁰ by citrate at 100 °C. Then, the metallic gold nucleates yielding small AuNPs (~2-4 nm), which aggregate rendering larger particles with diameters around 20 nm. Interestingly, no further stabilizing is required since citrate acts as both reducing and capping agent. Further studies proved that the nanoparticle diameter could be adjusted from 20 to 60 nm by changing the molar ratio between gold and citrate.^{40,41} Although Turkevich original method dates back from 1951, the growth mechanism of the particles is still not fully understood, being the subject of several recent studies.^{42,43}

Another popular synthesis of AuNPs is the Brust-Schiffrin method. Au³⁺ cations (from HAuCl₄) are reduced by NaBH₄ in a two-phase (water/toluene) system, in the presence of alkanethiol. The nanoparticles grow in the toluene phase with diameters ranging from 1 to 3 nm.⁴⁴ This method takes advantage of the strong interaction between gold and thiol group, which provides better colloidal stability. Different nanoparticle's sizes have been obtained by changing the initial reaction conditions⁴⁵ or replacing the alkanethiol for other thiolated ligands.⁴⁶⁻⁴⁸ It is worth to mention that water soluble AuNPs can be obtained by using tiopronin,⁴⁹ Bunte salt derivatives^{50,51} or thiolated tetraethylene glycole derivate⁴⁸ as capping ligands. In addition, an alternative protocol has been published, translating this method into one-phase system.⁵² Lastly, recent progress has combined Brust-Schiffrin method with seed-mediated strategy to obtain monodisperse AuNPs with diameters up to 300 nm.^{53,54}

1.3.2 Gold nanorods (AuNRs)

AuNRs are one of the most common MNPs used for biological applications. The main reason is their customizable longitudinal LSPR (L-LSPR) band, which can be easily shifted (Fig. 1.4) in the NIR optical window (*i.e.* range of wavelengths (700 – 900 nm) that present maximum depth penetration in biological tissues). In addition, AuNRs present stronger NIR absorption than other morphologies and scatter light at smaller sizes.²³

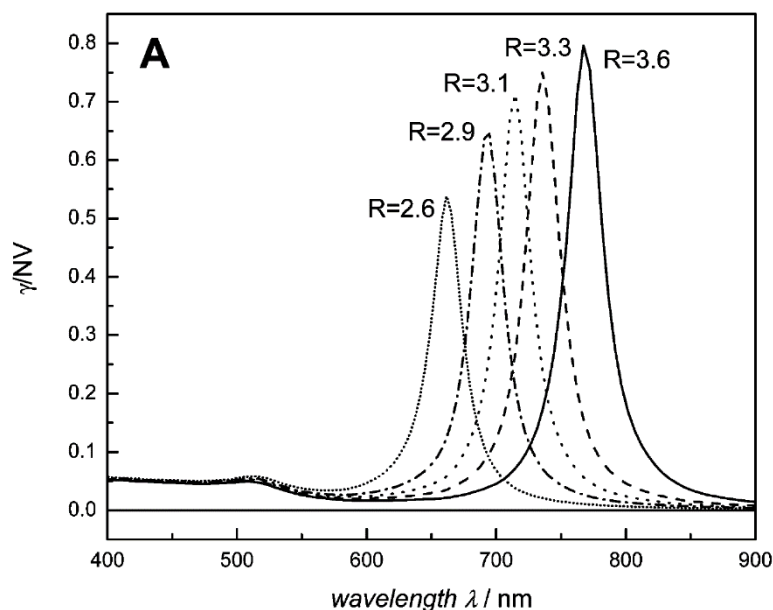


Fig. 1.4. Calculated normalized absorption (γ/NV) spectra of gold nanorods (elongated ellipsoids) with different aspect ratios (R) and dielectric constant of the medium of 2.05.⁵⁵

AuNRs are usually synthesized through seed-mediated method.^{56,57} This is a two-step protocol, where a seed solution is initially prepared by the fast reduction of HAuCl_4 by NaBH_4 . Then, the seeds are used in a second solution (growth solution) as nucleation points for the slow reduction of gold salts by ascorbic acid in the presence of hexadecyltrimethylammonium bromide (CTAB). Murphy *et al.* were the first to report the seed-mediated protocol, using citrate-capped penta-twinned AuNPs as seeds.⁵⁶ Later, El-Sayed *et al.* improved the method by using CTAB-capped single crystal AuNPs as seeds and growing the rods in the presence of AgNO_3 .⁵⁷ Over the years, several approaches have been developed in order to improve the quality of the rods. One of the most successful is modifying the rheological behaviour of the surfactant by the addition of organic⁵⁸ or inorganic salts.⁵⁹ Those additives change the CTAB micellar packing, increasing the monodispersity of the crystals. Alternatively, replacing the ascorbic acid or the CTAB for other reducing agents^{60,61} or ligands^{62,63} have also enhanced the results of the seed-mediated protocol.

1.3.3 Gold nanostars (AuNSs)

AuNSs are composed of a spherical core and several protruding tips.⁶⁴ The optical behaviour of the AuNSs is the combination of the two components, with a small plasmon band originating from the core and a big one from the tips. Interestingly, the position of the main plasmon band strongly depends on the aperture angle and roundness of the tips but little on their number.⁶⁵ The AuNSs are synthesized by seed-

mediated method. In early protocols, the gold salts were reduced by NaBH_4 in the presence of CTAB and seeds.⁶⁴ The stability of the resulting stars could be improved by functionalizing them with polyethylene glycol (PEG).⁶⁶ Since then, a new seed-mediated protocol with high-yield has been developed, where HAuCl_4 is reduced in a concentrated solution of poly(vinylpyrrolidone) (PVP) in *N,N*-dimethylformamide (DMF) and gold seeds.⁶⁵ The main LSPR induce a strong field enhancement near the tip's end.⁶⁷ This has been used to enhance the SERS signal and decrease the detection levels down to zeptomolar.⁶⁸

1.3.4 Spherical silver nanoparticles (AgNPs)

Turkevich method has also been applied for the growth of other MNPs beyond gold.^{69–71} Similarly to the synthesis of AuNPs, citrate acts as both reducing agent and ligand in the synthesis of AgNPs.⁷² While Turkevich protocol yields small and spherical AuNPs, this method produces silver nanoparticles with different shapes and larger sizes (*i.e.* diameters around 60 nm). The shape purity of the resulting AgNPs can be enhanced by dividing the crystal growth in a two-step procedure, where the nucleation and growth phases are performed at high and low pH, respectively.⁷³ Early since the publication of the first synthetic protocols, AgNPs were successfully used as substrate for SERS measurements.^{69,71} Another synthetic route to grow AgNPs includes oleylamine-liquid paraffin system.⁷⁴ In recent years, several silver nanostructures have been obtained by polyol method, where silver nitrate is reduced with ethylene glycol in the presence of PVP.⁷⁵ The final morphology of the nanoparticles can be adjusted by changing the molar ratio between AgNO_3 and PVP.⁷⁶

1.3.5 Gold (AuNCs) and silver nanoclusters (AgNCs)

Metal nanoclusters (MNCs) are a subclass of MNPs that belong to luminescent materials. MNCs are made of few to hundreds of atoms with particle sizes smaller than 2 nm.^{77,78} They present discrete electronic states as a result of strong quantum confinement effects⁷⁹ (due to the sub-2 nm sizes) and strong interaction with ligands.⁸⁰ Thus, MNCs present molecule-like behaviour, such as HOMO-LUMO transitions,⁸¹ strong fluorescence^{82,83} and quantized charging.⁸⁴ Those properties make them ideal candidates for catalysis^{85–87} and optical technologies.^{88,89} The ligand selection in the growth of MNCs is essential to stabilize them and avoid the formation of larger particles. Furthermore, the metal-ligand interaction also affects the final emission of the MNCs.⁹⁰ Since the interaction between thiol groups and gold and silver is very strong,

thiolated small molecules are frequently used as stabilizers. A standard synthetic protocol includes the reduction of gold or silver salts with NaBH_4 in the presence of a thiolated molecule. Some of the most commonly used ligands are glutathione,^{91–93} tiopronin,⁹⁴ phenylethylthiolate⁹⁵ and thiolated-cyclodextrin.⁹⁶ Alternatively dendrimers^{97,98} or biological macromolecules, such as DNA,^{99,100} proteins or peptides^{101,102} have also been used as templates to grow MNCs.

1.3.6 Others

In recent years, aluminium has emerged as a plasmonic candidate for applications involving the UV and visible regions of the spectrum instead of gold and silver.^{103–106} Gold presents two interband transitions at ~ 470 and ~ 330 nm,¹⁰⁷ which act as dissipative channels for the plasmon at high energies.¹⁰⁸ On the other hand, silver supports LSPR in the UV-visible region, however it has relatively low chemical stability.¹⁰⁸ The combination of current technology, which is capable of easily process aluminium, and the low price and high abundance of this metal have increased the interest in the use of aluminium nanoparticles in several analytical fields, such as SERS¹⁰⁹ and fluorescence enhancement-based biosensors.^{110,111}

1.4 Sensing applications

MNPs have been used in many sensing applications due to their ability to absorb and/or scatter light in their LSPR frequencies, which can be customized in the visible and near infrared (IR) regions of the spectrum.¹⁶ The nanoparticles with LSPR found in the visible range are ideal probes for point-of-care diagnostics, since they can be detected by naked eye or inexpensive instruments. On the other hand, nanoparticles that absorb or scatter light in the near IR can be used to detect analytes in biological samples, because their LSPR is located within the biological optical window.

Most sensing techniques are based on analyte-triggered changes in nanoparticle's optical properties. Alternatively, the optical properties of ligands (*e.g.* fluorescent probes or Raman tags) that interact with the core of the nanoparticle are used to generate sensing signals.

1.4.1 LSPR-based detection

The sensitivity of the LSPR to several factors has been used to build different types of MNP-based biosensors. Those can be classified in two groups: Aggregation-based or refractive index sensors.

1.4.1.1 Aggregation-based sensors

The aggregation of the nanoparticles causes inter-particle plasmonic coupling that renders a change in the solution's colour (*i.e.* from red to blue in the case of AuNPs) as the LSPR band red-shifts (Fig. 1.5a and Fig. 1.5b).¹¹² The colour change can be induced by any analyte that directly or indirectly aggregates (or disaggregates) the nanoparticles, and thus serves as a measure of the presence of specific analytes.^{113–115}

Early aggregation-based designs date back from 1990's and were initially focused on the detection of single-stranded oligonucleotides. Two sets of AuNPs were functionalized with two probe strands, and the hybridization between the probes and a target that contained complementary sequences to the two probes triggered the nanoparticles aggregation.¹¹⁷ Mirkin *et al.* were able to obtain sensitivities down to femtomolar with those designs.¹¹⁷ Functionalization of AuNPs with antibodies allowed to detect other antigens such as proteins. This was the principle behind the pregnancy tests commercialized by Carter-Wallace in the early/mid 90's.¹¹⁸ AuNPs were functionalized with antibodies to hCG (*i.e.* a glycoprotein hormone released by the

embryo during the pregnancy) and placed on a latex lateral flow strip. This was the first commercial AuNP-based sensor and still commercially available, sold by Church and Dwight.

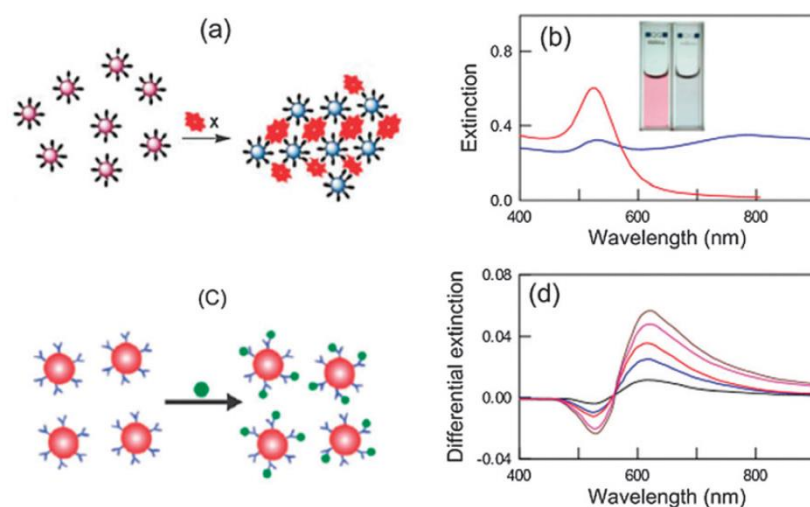


Fig. 1.5. (a) Scheme of analyte-triggered gold nanoparticle aggregation and (b) its corresponding change on the nanoparticle optical properties. (c) Scheme of the analyte binding to gold nanoparticles and (d) change on the differential extinction spectra at 600 nm, due to the variation of the dielectric constant of the nanoparticle surroundings.¹¹⁶

Thanh *et al.* developed an AuNP-based aggregation test for the quantification of anti-protein A in both water and serum.¹¹⁹ This presented similar sensitivity levels to traditional ELISA assays but easier protocol and shorter experimental times. Hirsch *et al.* replaced the spherical nanoparticles for near IR absorbing gold nanoshells, which allowed them to detect immunoglobulins within complex samples such as serum and whole blood.¹²⁰

Since Mirkin *et al.* early reports, aggregation-based assays have become one of the most studied MNP-based designs. They present several key advantages such as label-free protocols, homogeneous solution assays and detection by naked eye or low cost instruments.¹⁶ Nevertheless, they still present few issues that hinder their application in complex matrix, such as variable nanoparticle stability under changes of pH, temperature or ionic strength.¹⁶ The future improvements on nanoparticle colloidal stability will define the limits of MNP aggregation-based designs.

1.4.1.2 Refractive index sensors

Refractive index sensors are based on the change of the dielectric constant of the nanoparticle's vicinity by the analyte. The relation between the LSPR and nanoparticle's local environment is described by the following equation (Eq. 1.1).¹²¹

$$\Delta\lambda_{\text{LSPR}} = m \cdot \Delta n \left[1 - \exp\left(\frac{-2d}{l_d}\right) \right] \quad (\text{Eq. 1.1})$$

where m is the nanoparticle's bulk refractive index, Δn is the change of the refractive index caused by the adsorbate, d is the effective thickness of the adsorbate layer, and l_d is the characteristic electromagnetic-field-decay length. This effect is distance dependent. Therefore, the analyte has to be located in close proximity to the nanoparticle surface to effectively change the refractive index of the surroundings and shift the position of the LSPR band.

The first designs of refractive index sensors were developed in the early 1980s and were used to study events on metal surfaces¹²² and gas sensing.¹²³ Most common designs employ a thin gold surface as plasmonic nanostructure.¹²⁴ Nevertheless, several alternatives using AuNPs,¹²⁵ gold nanocrosses,¹²⁶ gold nanoholes¹²⁷ or silver triangles¹²⁸ have been developed in order to improve the technique's sensitivity. While all those designs are heterogeneous assays, Englebienne *et al.* proved that homogeneous assays could also be performed by coating the AuNPs with a single antibody.^{129,130} The nanoparticles remained in solution after binding to the analyte but their LSPR band shifted due to the change on the environment refractive index. One advantage of homogeneous designs is that the interactions between molecules depend on radial diffusion. This presents faster mass transfer than planar diffusion, which is the main mass transport mechanism when using macroscopic sensing devices, such as SPR. The faster mass transfer allows faster sensing measurements and better characterisation of rapid kinetic events.

1.4.2 Surface enhanced Raman spectroscopy (SERS) sensors

The physical principle behind this technique is the Raman scattering, *i.e.* inelastic scattering of electromagnetic radiation by a target molecule.¹³¹ Since Raman scattering depends on the vibrational modes of the molecule, its signal is characteristic for every target.¹³² Nevertheless, the low efficiency of inelastic scattering of photons hinders the application of this technique for analyte detection and quantification.¹³³ The intensity of Raman scattering can be highly enhanced by placing the analyte near to a metal surface, whose plasmon field is excited.¹³³ This approach is called SERS. Additionally, indirect assays can also be performed by using Raman-active dyes as signal transducers, where their signal is influenced by the analyte.¹³⁴ Isolated AuNPs have been reported enhancing the signal up to $10^3 - 10^4$ and aggregated nanoparticles up to 10^{15} ,¹³⁵ which allows single molecule detection.^{136,137} The formation of hot spots between near AuNPs, where their plasmon fields are coupled, is accounted for the big

scattering enhancements. Interestingly, theoretical experiments indicate that field effects on hot spots can only enhance the SERS signal up to 10^{10} .¹³⁸ Therefore, an additional factor besides the electromagnetic field has to play a role on the SERS signal generation. Otto and Persson proposed a chemical factor, where the ballistic electrons in the metal interact with a strongly chemisorbed molecule.^{139,140}

1.4.3 Fluorescence-based detection

Fluorescence is one of the most well-established techniques in sensing and biomedical diagnostics.¹⁴¹ However, there is still a need for improving its sensitivity.¹⁴² There are several factors that limit its clinical application, such as photobleaching of fluorophores¹⁴³ and autofluorescence of the luminescent samples.¹⁴⁴ Modifying the emission behaviour of fluorophores by coupling them with a metal surface has been applied to overcome those limitations.¹⁴²

1.4.3.1 Plasmon-resonance energy transfer (PRET) sensors

When a donor (e.g. organic dye or quantum dot) is placed near a metal surface, a resonant energy transfer occurs in a similar way to Förster resonance energy transfer (FRET).¹⁴⁵ In addition to the energy transfer, the plasmon also affects the donor radiative lifetime.¹⁴⁵ Both effects contribute to the strong fluorescence quenching, which can be described by the Gersten-Nitzan model.¹⁴⁶ Even though FRET and PRET have similarities, they also present significant differences: PRET shows stronger quenching efficiency, due to the greater molar extinction coefficient of the plasmonic nanoparticles in comparison to organic dyes.²⁹ FRET occurs in a distance range from 1 to 10 nm between the donor and acceptor, while PRET can double that distance.¹⁴⁷ Photoluminescence and luminescence lifetime experiments have proved that the quenching fluorescence of PRET decreases with a metal-dye separation of $1/d^4$, while traditional FRET does with a donor-acceptor distance of $1/d^6$.¹⁴⁸

A wide group of PRET sensors have been designed by combining MNPs with different kind of donors, such as organic dyes,^{149,150} quantum dots,^{151–153} metal nanoclusters^{154,155} and conjugated polyelectrolytes.^{156,157} Those have been applied for the sensing of metal ions,^{149,158} small molecules,^{159,160} proteins,¹⁶¹ bacteria¹⁶² and tracking molecular events, such as protein-DNA binding.¹⁵⁶ Interestingly, PRET has been used in molecular beacons for DNA sensing.¹⁶³ In this, the extremes of a self-complementary probe with hairpin structure are functionalized with a donor and a MNP. The hairpin structure locates the donor near the nanoparticle, yielding a strong

fluorescence quenching. Upon probe hybridization with the target, the hairpin structure opens in a rod-like conformation and separates both donor and acceptor (Fig. 1.6). The fluorescence is restored and the intensity depends on the target concentration. This system can also be used to monitor the cleavage of nucleotides by nucleases.¹⁶⁴

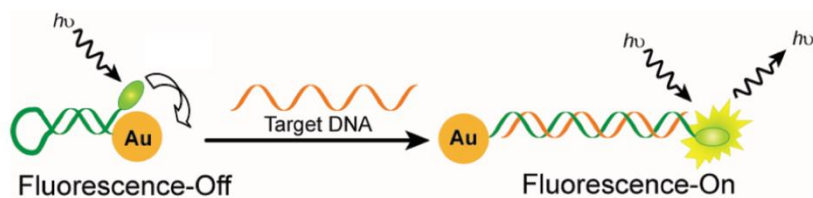


Fig. 1.6. Scheme of molecular beacon exploiting FRET principle for DNA sensing.¹⁵

1.4.3.2 Metal-enhanced fluorescence sensors

In some situations, the electromagnetic coupling between a metal nanoparticle and a fluorophore yields additional de-excitation pathways, which may enhance the fluorophore's excitation rates and/or the radiative decay rates that in turn result in fluorescence enhancement.^{165–167} Both plasmon-induced quenching and fluorescence enhancement compete and are distance dependent phenomena. At short distances, the energy transfer between the fluorophore and plasmon dominates.¹⁶⁸ However, at specific distances from the metal surface the energy transfer is highly reduced, while the electromagnetic field is still strong enough to enhance the fluorescence.^{169,170} A distance range between 10 – 20 nm from the metal surface has been reported presenting the strongest fluorescence enhancement.¹⁶⁸ Additionally, the plasmon band overlapping the fluorophore's emission and absorbance bands is also required for maximum enhancement.¹⁶⁵ Regarding the role of the size and morphology of nanoparticles, the particles with larger scattering cross-section present higher fluorescence enhancement.^{171,172}

Even though metal-enhanced fluorescence sensors are not as common as FRET sensors, some homogeneous assays using this mechanism have been developed for the detection of biomolecules, such as DNA¹⁷³ or proteins.¹⁷⁴

1.5 MNPs in other bioresponsive technologies

A current trend in bioscience and bioengineering is to mimic and apply mechanisms and processes that occur in living organisms to technology.¹⁷⁵ For instance, the surface of metal nanoparticles can be functionalized with oligonucleotides^{117,120} or antibodies¹⁷⁶ to control their aggregation upon biological stimuli. As previously described, this principle has been widely used in biosensing and analytical science.¹⁵ Nevertheless, there are other emerging fields in nanotechnology that exploit similar biomolecular recognition events, such as smart drug delivery,^{177–179} imaging²⁹ or nanocomputing.^{180,181}

Examples of those works include hollow and porous gold nanoparticles filled with cargo molecules, which are released upon biological interaction for smart drug release,^{178,179} or using the change on the optical properties of gold nanoparticles upon addition of biological inputs for performing logic operations.¹⁸⁰

Besides those examples, transferring all the knowledge acquired over the time from biosensing to other biotechnological fields is still a challenge and further work has to be done.

1.6 Objectives

The main goal of this thesis is to develop novel applications of metal nanoparticles in the field of biosensing and bioresponsive materials. This is divided in the following specific objectives:

- Design new syntheses of metal nanoparticles for precise control over their optical properties and morphologies.
- Build new metal nanoparticle-based systems for disease prevention.
- Develop metal nanoparticle-based biosensors for the analysis of novel cancer biomarkers and molecular events.
- Apply the biological interactions exploited in the biosensors to other bioresponsive technologies.
- Expand the biosensing principles to other plasmonic nanomaterials.

Chapter 2

Characterisation Techniques

This chapter describes the common characterisation techniques used for the physical properties determination of the colloidal systems involved in this thesis. Specific details are described in the experimental section of each chapter.

2.1 UV-Vis spectroscopy

UV-Vis spectroscopy measures the sample electromagnetic radiation absorbance in the visible region and the surroundings (*i.e.* near-ultraviolet and near-infrared). The absorbed light pumps electronic transitions from the ground to the excited states. The attenuation of light that goes through a material can be described by the Beer-Lambert law (Eq. 2.1).¹⁸²

$$A = \log\left(\frac{I_0}{I}\right) = \varepsilon cL \quad (\text{Eq. 2.1})$$

where A is the absorbance, I_0 and I are the incident and transmitted intensities of light at a specific wavelength, respectively, ε is the molar absorptivity of the studied species, c is its concentration and L is the path length.

Sample preparation and measurements

The UV-Vis absorbance of the liquid samples was recorded with a spectrometer (the specific model is specified in the *Experimental section* of every chapter). The background absorbance was recorded before the sample's analysis and used as baseline.

2.2 Fluorescence spectroscopy

The technique involves exciting electrons from the studied specie by incident light, and recording the electromagnetic emission produced by the electron transitions from excited to ground states.

2.2.1 Fluorescence polarisation

Fluorescence polarisation is an analytical method that provides information about biomolecular interactions by measuring the degree of a fluorophore polarisation, which is inversely proportional to the fluorophore rotation when is undergoing Brownian motion. When a large biomolecule binds to a dye-labelled dsDNA, the larger volume of the complex hinders the fluorophore movement, increasing its fluorescence polarisation.

2.2.2 Sample preparation and measurements

The emission and excitation of liquid samples were recorded with an Infinite M200 plate reader from Tecan. Black and opaque well-plates were used for the measures.

2.3 X-ray diffraction (XRD) spectroscopy

This technique employs the diffraction of a monochromatic X-ray beam to study the crystal structure of a powder sample. If the sample was monocrystalline, the diffraction pattern would present discrete spots, also known as Laue spots. Nevertheless, because the sample is a powder, the crystals are randomly placed and all the crystalline orientations are present, resulting in a ring-shaped diffraction pattern. The angle between the diffracted rings and the original beam axis is called scattering angle (2θ). This angle is found as variable in Bragg's law equation (Eq. 2.2),¹⁸³ which describes the required conditions for the constructive interference necessary for the XRD.

$$n\lambda = 2d \sin \theta \quad (\text{Eq. 2.2})$$

Where n is an integer multiplier, λ is the incident radiation's wavelength and d is the atomic interplanar distance.

The diffractogram (*i.e.* graphical representation of the diffraction data) can provide both qualitative and quantitative information, based on three variables: (1) Signal intensity as a function of 2θ . (2) The peak's intensity. (3) The diffraction maxima.

Sample preparation and measurements

XRD experiments were performed with a D8 Discover Gadds (Bruker Corporation, Billerica, USA). The samples were prepared by drying a liquid sample on a silicon wafer, and the diffraction data was collected from 20 to 90 2θ (degree).

All the recorded diffractograms were compared to the reference powder data for identification purposes.

2.4 Transmission electron microscopy (TEM)

TEM is a microscopy technique that exploits the interaction between a uniform current density electron beam (*i.e.* energies within a range of 60 to 150 keV) and a thin sample. When the electron beam reaches the sample, part of the electrons are transmitted and the rest are elastically or inelastically scattered.¹⁸⁴ The magnitude of the interaction depends on several factors, such as size, sample density and elemental composition. The final image is built with the information acquired from the transmitted electrons.

TEM can be divided in three big parts: electron gun, lenses and apertures, and image generation system. The electron gun, which consists of LaB₆ rods or tungsten filament with hairpin or pointed shape, emits electrons by thermionic or field emission. Then, the electrons go through the condenser electromagnetic lens and aperture, which provide control over the amount of current in the beam that reaches the sample and the illuminated area. Larger condenser aperture angles result in higher sample illumination but poorer image quality. The resulting electron beam interacts with the sample and is collected and magnified for a set of lenses. It is worth mentioning that the objective aperture controls the electrons that contribute to the image and can be used to improve its contrast. Finally, the image is projected in a phosphorescent screen or CDDD camera.

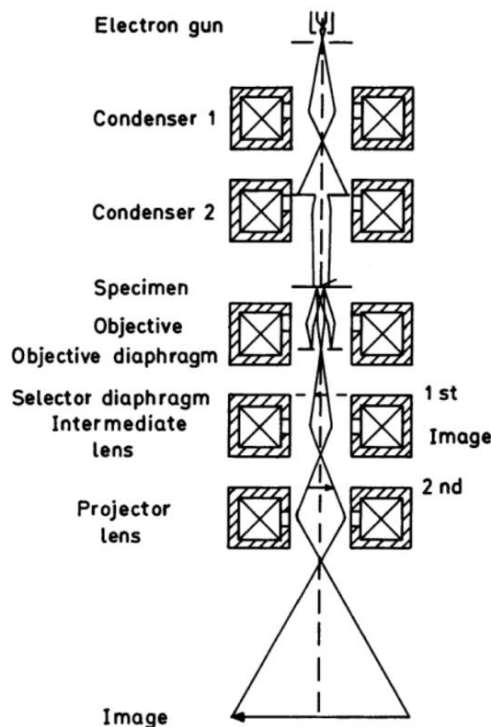


Fig. 2.1. Schematic electron path and main components in a TEM.¹⁸⁴

2.4.1 High-resolution TEM (HR-TEM)

HR-TEM is an imaging mode of electron microscopy that uses phase-contrast imaging, where both transmitted and scattered electrons are combined to produce the image. In comparison to traditional TEM imaging, HR-TEM requires a larger objective aperture in order to employ the scattered electrons.

Phase-contrast imaging is the technique with highest resolution ever developed and allows to detect the arrays of atoms in crystalline structures.

2.4.2 Cryo-electron microscopy (cryo-TEM)

Cryo-TEM is a subclass of TEM that allows visualizing near-unaltered samples in their frozen-native environment by vitrifying them at cryogenic temperatures (liquid nitrogen is usually employed to freeze the samples). This technique is highly used in molecular biology and surfactant chemistry due the lack of factors (*i.e.* staining and sample's preservation in non-physiological environments) that can alter the conformation or assembly of the sample's molecules.

2.4.3 Sample preparation and imaging for TEM and HR-TEM

TEM was employed to study the nanoparticle morphology while HR-TEM was used to assess the crystal structure (the specific models are specified in the *Experimental section* of every chapter). Samples were prepared by dropping the liquid solution containing the nanoparticles onto a carbon coated copper grid. The grid was left to air-dry until the water had fully evaporated.

Alternatively, when the particles presented a high surface charge, the carbon-coated copper grid was dipped in the diluted liquid solution to minimise the nanoparticle accumulation on the grid's edge during the drying step.

Nanoparticle dimensions were determined with ImageJ software (<https://imagej.nih.gov/ij/>) from at least 3 images and measuring more than 300 particles per image.

2.4.4 Sample preparation and imaging for cryo-TEM

Cryo-TEM was used to study the morphology of CTAB micelles in the AuNR growth solutions. The liquid samples were vitrified by a commercial automated plunge-freezer

called Vitrobot (commercialized by FEI Company). This device vitrifies water solutions by cooling them very fast, so water molecules do not have time to form long-range ordered crystal lattices. This results in an amorphous state that is similar to liquid water.¹⁸⁵ Vitrobot accomplish this amorphous state in four steps: (1) placing the liquid sample in the carbon-coated copper grid, (2) removing the excess of liquid in order to produce a thin film, (3) plunge-freezing the grid into the liquid nitrogen and (4) storing the vitrified sample in a storage box that contains liquid nitrogen.

2.5 Dynamic light scattering and zeta potential

2.5.1 Dynamic light scattering (DLS)

DLS, also known as photon correlation spectroscopy, is a technique that calculates the diffusion of small objects or particles undergoing Brownian motion in a solution (diffusion coefficient D). When the particles are smaller than the incident light wavelength, the light is elastically scattered in all directions. DLS measures the scattering fluctuation intensity of a monochromatic light that goes through the sample over time and calculates D . The motion of the particles is then used to calculate the particle size by using Stokes-Einstein equation (Eq. 2.3).¹⁸⁶

$$D_H = \frac{kT}{6\eta\pi r} \quad (\text{Eq. 2.3})$$

In this equation, D_H is the nanoparticle's hydrodynamic diameter, k is the Boltzmann's constant, T is the thermodynamic temperature, η is the solution's viscosity and D is the diffusion coefficient. It is noteworthy that r depends on several factors such as ionic strength and particle size, morphology and surface.

2.5.2 Zeta potential

Zeta potential (ζ -potential, also known as electrokinetic potential) in a colloid system is the electric potential in the interface between the slipping plane, *i.e.* stationary layer of fluid attached to the particle surface, and the medium. The layer of liquid surrounding to the colloid can be divided in two parts: (1) the Stern layer, where the ions are very close to the surface and are strongly attached to it and (2) the diffuse layer, where the ions are loosely attached to the particle. When a particle diffuses through the liquid, the ions in the Stern layer remain attached, while part of the ions in the diffuse layer stay in the bulk fluid. The potential between the moving and stationary ions is the zeta potential, which can be measured by electrophoresis. When an electric field is applied across the colloid solution, the particles within the solution will move towards the electrode of opposite charge with a velocity (electrophoretic mobility U_E) proportional to their zeta potential magnitude. The U_E can be expressed by the following equation (Eq. 2.4).¹⁸⁷

$$U_E = \frac{2\varepsilon z f(ka)}{3\eta} \quad (\text{Eq. 2.4})$$

In this equation, ε is the dielectric constant, z is the zeta potential, $f(ka)$ is Henry's function and η the viscosity of the system.

2.5.3 Sample preparation and measurement

The hydrodynamic diameter and zeta potential of the colloidal samples were recorded with dynamic light scattering spectrometers (the specific models are specified in the *Experimental section* of every chapter). The instruments were periodically validated with polystyrene latex standard provided by the fabricants.

2.6 Capillary viscometer

Capillary viscometers are instruments that calculate the viscosity of a fluid by measuring the time required by a specific volume to flow through the instrument. Those measures require constant control of the temperature during the course of the experiments. Different kind of viscosities (e.g. dynamic, kinematic and relative viscosities) can be measured. In the present thesis, relative viscosity (*i.e.* ratio between the fluid viscosity and the viscosity of the solvent) has been used to characterize the rheological properties of the fluids.

Sample preparation and measurements

The relative viscosity of the samples was measured with a Cannon-Fenske viscometer (Fig. 2.2).

The viscometer was turned upside down and a rubber bulb was placed in the tube L. The sample was suctioned through the tube N and drawn up until reaching the etched ring F. The viscometer was returned to the original upright position and the borders of tube N were cleaned.

The viscometer was introduced into a thermostatic bath with water at 22 °C. Only the upper parts of both L and N tubes were above the water level. When the temperature equilibrium was achieved, some pressure was applied to bring the fluid level above the mark E. The bulb was removed and the flow time (*i.e.* time required for the bottom of the meniscus to move from the mark E to mark F) was timed.

In order to calculate the relative viscosity, the flow time of every fluid was divided by the flow time of the distilled water.

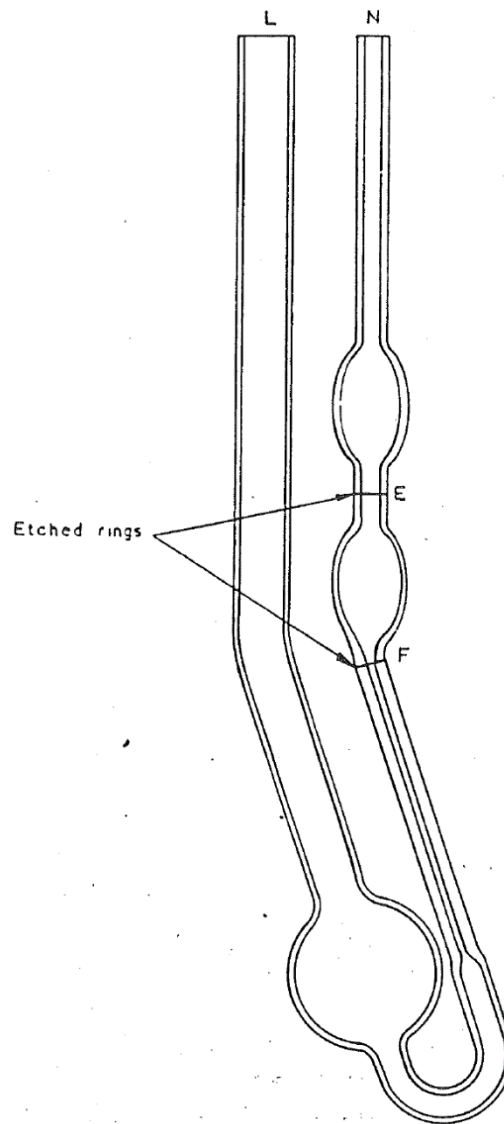


Fig. 2.2. Schematic Cannon-Fenske viscometer.¹⁸⁸

Chapter 3

Fine-tuning of Gold Nanorod Dimensions and Plasmonic Properties Using the Hofmeister Effects

The applications of gold nanorods in sensing and therapeutics require easy syntheses with a precise control over their dimensions. Here, we report a method for the synthesis of highly pure and monodisperse gold nanorods with fine-tuneable dimensions and longitudinal localised surface plasmon resonance by addition of Hofmeister salts into the growth medium. To gain understanding of the anisotropic growth mechanism, we have studied the physical changes of the CTAB micelles induced by the salts using rheology, microscopy and light-scattering techniques.

3.1 Introduction

Over the past decade nanoplasmonic field has been significantly developed due to the introduction of a variety of novel synthetic methods and biofunctionalisation strategies for new morphologies beyond sphere (*i.e.* nanorod, nanostar, nanocross, etc).¹⁸⁹ Anisotropic plasmonic nanoparticles have been the subject of numerous studies because of their unique optical and electronic properties, *e.g.* strong absorbance in the near-infrared,⁶⁷ higher in coupling efficiency¹⁹⁰ or significant increase surface-enhanced Raman spectroscopy signal.¹⁹¹ Among different nanocrystals, gold nanorods (AuNRs) have attracted great attention for their distinct nanoplasmonic properties and successful utilization in a wide range of biological applications such as photothermal therapy,^{192–195} drug delivery,¹⁹⁶ imaging^{18,197–199} and sensing.^{200–202} One of their main features is the longitudinal localised surface plasmon resonance (L-LSPR), the light-induced coherent collective oscillation of the valence electrons through the longitudinal axis, that results in a unique and intense light absorption in a wide wavelength range.^{112,121} This optical property depends highly on the aspect ratio of the rod that can be customised through the controlled synthesis.

The most common synthesis of AuNRs is the seed-mediated method, which was initially developed by Murphy *et al.*²⁰³ and later improved by El-Sayed *et al.*⁵⁷ This seed-mediated method is a two-step procedure. Firstly, gold seeds are obtained by the fast reduction of gold salts by NaBH₄. Subsequently, the obtained gold seeds are used as nucleation points for the slow reduction of the gold salts by ascorbic acid in the presence of CTAB surfactant. Interestingly, depending on the nature and structure of the seeds, different kinds of AuNRs can be obtained. Initially, Murphy *et al.* used citrate-capped penta-twinned gold nanoparticles as a seeds, which yielded twinned crystal rods with {111} faces (silverless synthesis). On the other hand, El-Sayed *et al.* synthesized the seeds in the presence of CTAB, yielding single crystal nanoparticles of 1.5 nm diameter.²⁰⁴ Those seeds were later used to growth single crystal AuNRs in the presence of AgNO₃ (silver assisted synthesis). The exact role of CTAB in the promotion of the anisotropic growth is still unclear. At early stages, El-Sayed *et al.* suggested that the CTAB acted as a soft template.⁵⁷ However, subsequent publications indicated the CTAB adsorption in specific gold facets, favouring specific surface passivation.^{21,56} Furthermore, the shape-sensitivity to CTAB impurities,²⁰⁵ presence of halides^{206,207} and temperature effect^{208,209} were also reported. A big effort has been recently made in order to enhance the tunability and monodispersity of AuNRs. Murray *et al.* reported a synthesis with high control over the nanocrystal

growth through the inclusion of aromatic additives, which changed the micellar packing of the surfactant.⁵⁸ In addition, alternative reducing agents^{60,61} or different surfactants^{62,63} have also been used to increase the quality of the AuNRs.

Interestingly, CTAB molecules self-assemble in spheroid shape micelles in water.²¹⁰ The addition of salts, co-surfactants or other additives can change the micellar behaviour, e.g. transition from sphere to rod or worm-shaped micelles.²¹¹ In the presence of the salts, the micellar changes are caused by the screening of the electrostatic repulsion between the polar heads of the surfactant molecules. A comparison between the effects of different anions on micellar growth showed that they follow the Hofmeister series order,²¹² which is a historical classification of salt capacity to precipitate (also known as *salting out*) or solubilize (also known as *salting in*) proteins in water. The protein solubility is affected by the electrostatic forces of the ions and their capacity to affect the surrounding water structure.²¹³ Traditionally, the anionic *salting out* order of the Hofmeister series has been considered as the following: $\text{SCN}^- > \text{ClO}_4^- > \text{I}^- > \text{ClO}_3^- > \text{NO}_3^- > \text{Br}^- > \text{Cl}^- > \text{HSO}_4^- > \text{SO}_4^{2-}$.

In this chapter, we present a new methodology to fine-tune the AuNRs while keeping the basis of the well-established seed-mediated synthesis. As mentioned earlier, the customisation of monodisperse AuNRs has been generally achieved by using alternative reducing agents, co-surfactants or organic additives. In our method, we successfully employ a fourth strategy: using the Hofmeister salts, which provide precise control over the morphology and optical properties of the crystals. Moreover, for the first time, the CTAB micelle morphology has been studied under AuNR growth conditions, yielding new insights on the anisotropic growth of the rods.

3.2 Experimental section

3.2.1 Materials

The following products were used as received. Sodium nitrate (NaNO_3 , >99%), sodium bromide (NaBr , >99%), sodium chloride (NaCl , >99%), sodium bisulfate (NaHSO_4 , >99%), sodium thiocyanate (NaSCN , >98%), sodium perchlorate (NaClO_4 , >98%), hydrogen tetrachloroaurate trihydrate ($\text{HAuCl}_4 \cdot 3\text{H}_2\text{O}$), silver nitrate (AgNO_3 , 0.1 N), hydrogen chloride (HCl , 37% wt in water), L-ascorbic acid (crystalline), sodium borohydride (NaBH_4 , 98%) were purchased from Sigma-Aldrich. Hexadecyltrimethylammonium bromide (CTAB, >98%) was purchased from Tokyo Chemical Industry.

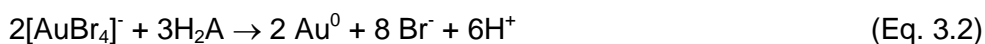
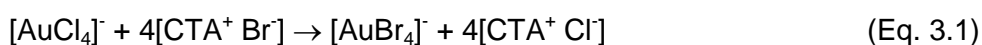
All the water employed in the experiments was obtained with a Mili-Q Integral 5 system. All glassware was cleaned with aqua regia, rinsed extensively with water, and dried before use.

3.2.2 Synthesis of AuNRs

Synthesis of seeds. The reaction was performed at 22 °C. The CTAB solution (5 ml, 0.2 M) was added to a 5.0 mL solution of HAuCl_4 0.5 mM. While the mixture was being vigorously stirred, 0.6 mL of ice-cold NaBH_4 10 mM was added at once. The seed solution was stirred for 30 sec and was left undisturbed for 30 min. Then, the seeds were immediately used to synthesize the gold nanorods. Fresh seeds are necessary to obtain monodisperse AuNRs,²¹⁴ with most syntheses letting the seeds age between 30 min and 2 h.^{56,58,62,63} In addition, CTAB solubility in water is 0.1 M at 20 °C.²¹⁵ Thus, the shorter the aging time is, the less likely the CTAB starts precipitating.

Synthesis of rods. 250 μL of AgNO_3 (4 mM) were added to 5.0 mL solution of CTAB (0.1 M). The solution was kept undisturbed for 15 min, after which 5 mL of HAuCl_4 (1 mM), a specific volume of one of the salt solutions (Table S1) and 12 μL of HCl (37%) were added. Since bromide has higher affinity for gold than chloride, mixing HAuCl_4 with CTAB results on the formation of HAuBr_4 (Eq. 3.1), changing the gold solution colour from yellow (HAuCl_4) to orange (HAuBr_4). After slow stirring, ascorbic acid (75 μL , 79 mM) was introduced into the growth solution, which lost its orange colour and yielded a colourless solution, because of the reduction of Au^{3+} to Au^{1+} . The mixture was vigorously stirred for 30 sec and 60 μL of the seed solution were added. Ascorbic acid

on its own can only reduce Au^{3+} to Au^+ , and it requires nucleation points to reduce gold salts to metallic gold (Eq. 3.2). Finally, the growth solution was vigorously stirred for 30 sec and left undisturbed for 12 h. The gold nanorods were isolated by centrifugation at 8000 rpm for 15 min followed by removal of the supernatant twice. The precipitate was re-dispersed in 10 ml of milli-Q water. It is noteworthy to mention that the stoichiometric ratio between HAuCl_4 and ascorbic acid is 1:1.5 in the gold reduction reaction.²¹⁶ However, this ratio presents fast reaction kinetics, which yields short²¹⁷ and not well monodisperse rods. Due to the fact that we prioritize monodispersity over yield, the 1:1.2 ratio was used with a maximum yield of 80%. Previous researchers have used the same ratio²¹⁸ or even lower.^{58,62}



3.2.3 Characterization

Transmission electron microscopy (TEM) images were acquired with a JEM-1010 microscope operating at 100 kV. High-resolution transmission electron microscopy (HR-TEM) images were obtained with a JEM-2100 microscope operating at 200 kV. Cryo-transmission electron microscopy (cryo-TEM) imaging was performed with a Titan Krios cryo-TEM operating at 300 kV. The study of the nanoparticle and micelle morphology and size distribution was performed by analysing several TEM, HR-TEM or cryo-TEM images for every sample. The optical extinction spectra were recorded using a Spectramax M2/M2^e UV/Vis/NIR spectrophotometer. The dynamic light scattering (DLS) and zeta potential measurements were performed with a Zetasizer Nano Z from Malvern Instruments. The X-ray diffraction (XRD) measurements were performed with D8 Discover Gadds. The viscosity data was obtained with a Cannon-Fenske viscometer.

3.3 Results and discussion

3.3.1 Tuning the L-LSPR band

Even though the exact mechanism involved in the Hofmeister series is not clear, it is widely accepted that the series can be divided into different sections depending on their salting in/out effects.²¹⁹ The first group includes ions with small hydrated radii and salting out capacities (e.g. NH_4^+ or F^-). Following, there is a group with neutral or moderate behaviours (e.g. Cl^- or Na^+). Finally, the last group is composed by bigger ions with lower ionic strength, which presents salting in effect (e.g. SCN^- or Ca^{2+}).

In order to explore the tuning capacities of Hofmeister anions, the following six salts were studied: NaSCN , NaClO_4 , NaNO_3 , NaBr , NaCl and NaHSO_4 . Na^+ was selected to be in all the salts in order to have equalised cation effect in all the experiments. All the anions were monovalent and representatives of the Hofmeister series. SCN^- and ClO_4^- present salting in ability; NO_3^- , Br^- and Cl^- are neutral members of the series and HSO_4^- has salting out capacity.

As described in the Experimental section, AuNRs were synthesised using our own modified version of seed-mediated method,⁵⁷ by introducing the selected salts at different concentrations in the growth solution before the addition of ascorbic acid. The extinction spectra of the resulting AuNRs with NaNO_3 , NaCl , NaHSO_4 and NaBr are plotted in the Fig. 3.1. It is important to note that the growth solution contains some Hofmeister anions from the beginning, such as bromide (from CTAB), nitrate (from AgNO_3) and chloride (from HCl). However, their concentrations are the same in all samples, therefore their effects are equal in all the cases. The concentrations used in the text and figures are the added concentrations of Hofmeister salts.

Among six tested anion salts, SCN^- and ClO_4^- quenched the reduction reaction of gold salt and precipitated the surfactant. The colour change in the growth solution from colourless to red, which is the symbol of the AuNRs formation, was not observed. These observations were in agreement with previous studies, which showed a decrease in the reduction potential of gold ions after their conjugation with SCN^- ²²⁰ and an aggregation of the dodecyltrimethylammonium bromide (cationic surfactant with 12 aliphatic carbons instead of 16 like CTAB) induced by SCN^- and its precipitation by ClO_4^- .²²¹ The rest of the four salts did allow the synthesis of AuNRs and more importantly tuned the L-LSPR band either to longer or shorter wavelengths.

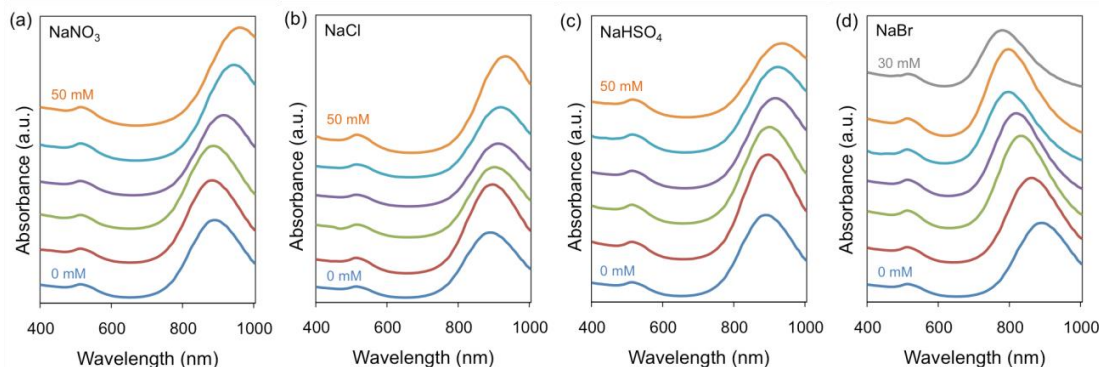


Fig. 3.1. Normalized extinction spectra of AuNRs grown in the presence of additional amount of Hofmeister salts. For (a), (b) and (c) the salt concentrations are 0 mM (blue), 10 mM (red), 20 mM (green), 30 mM (purple), 40 mM (turquoise) and 50 mM (orange) from bottom to top. For (d), the salt concentrations are 0 mM (blue), 5 mM (red), 10 mM (green), 15 mM (purple), 20 mM (turquoise), 25 mM (orange) and 30 mM (grey) from bottom to top. All the spectra have been offset for easier comprehension.

NaNO_3 , NaCl and NaHSO_4 red-shifted the L-LSPR, with bigger changes coming from the addition of 50 mM NaNO_3 ($\Delta_{\text{L-LSPR}} = 76$ nm). The addition of 50 mM NaCl or 50 mM NaHSO_4 produced similar effects with $\Delta_{\text{L-LSPR}}$ up to 44 and 49 nm, respectively. NaBr had the biggest impact on the L-LSPR peak, *i.e.* blue-shifting it up to 107 nm from lowest to highest salt concentration. In contrast to the other salts, the maximum concentration of the added NaBr in the growth solution was 30 mM. Above this amount, spheroid shape particles were mainly obtained. It is worth mentioning that the low intensity of the bands around 510 nm indicates the high shape purity of the samples.

Finally, since Hofmeister series only include few representatives, the behaviour of other ions can be estimated by comparing their hydrated radii and salting in or salting out abilities with the ions contained in the series. This can be used as a tool for predicting the influence of salts in the growth of AuNRs.

3.3.2 Morphology and crystalline structure of the AuNRs

Fig. 3.2 shows the TEM images of the monodisperse AuNRs with small shape impurities (average below 6%) obtained by our modified El-Sayed synthesis. As expected, the variations on the aspect ratios are coherent with the shifts of the L-LSPR band induced by the salts (Table 3.1). Thereby, NaNO_3 (0-50 mM) leads to the biggest aspect ratio increases from 4.1 up to 4.8. NaCl and NaHSO_4 (0-50 mM) lead to similar increases in aspect ratio up to 4.7 and 4.6, respectively. On the other hand NaBr (0-30 mM) leads to a decrease of the aspect ratio from 4.1 to 3.3.

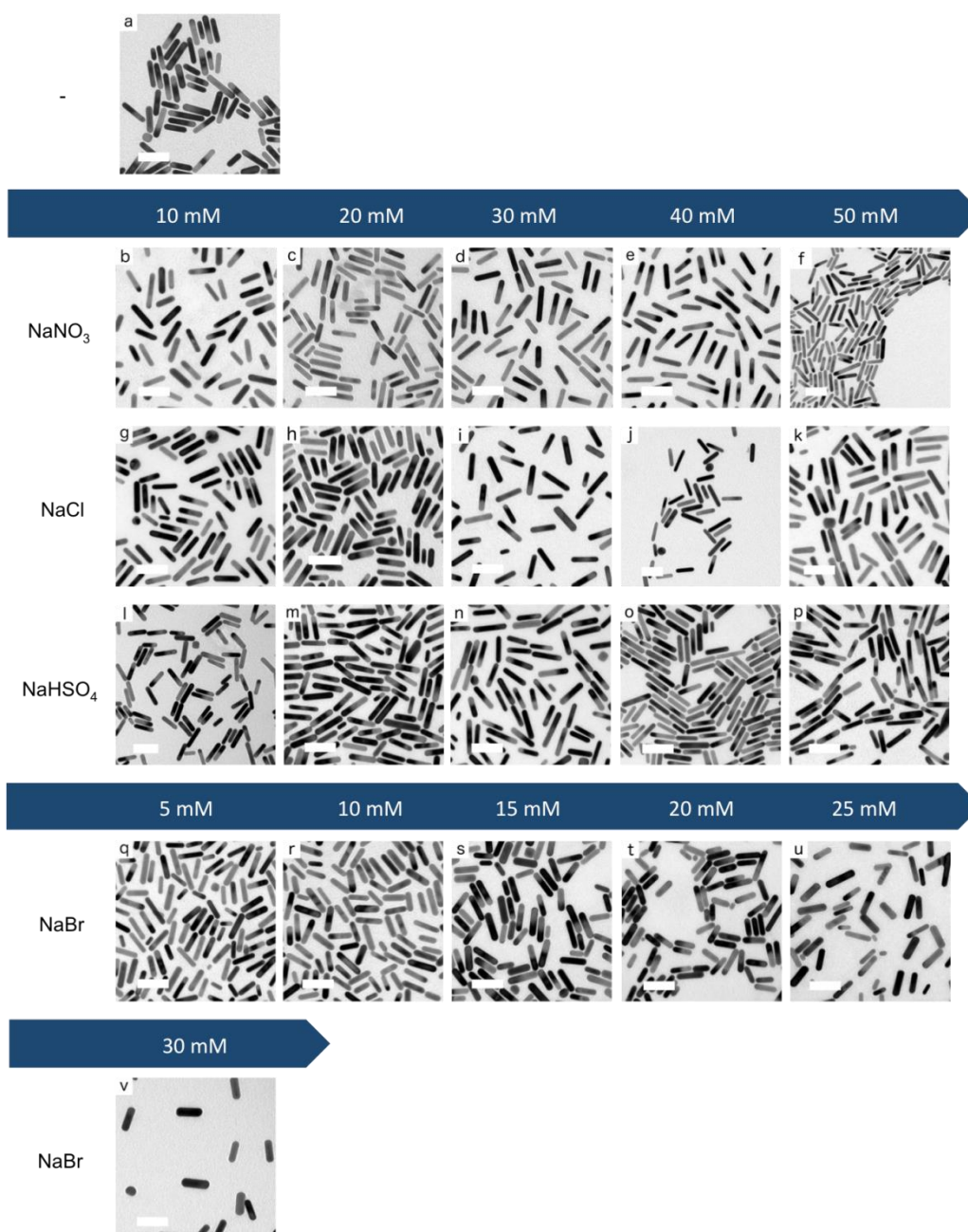


Fig. 3.2. TEM images of AuNRs synthesized using our seed-mediated method with different amounts of Hofmeister salts: (a) without Hofmeister salts. (b - f) with NaNO_3 , (g - k) with NaCl and (l - p) with NaHSO_4 in order of increasing added concentration (10 - 50 mM). (q - v) with NaBr in order of increasing added concentration (5 - 30 mM). All scale bars are 50 nm.

Interestingly, the increases of the aspect ratio linked to NaNO_3 are mainly caused by the reductions of the rod widths (from 10.6 nm to 8.8 nm), but little by rod elongations (no clear tendency of elongation), as shown in the Table 3.1. The increases in aspect ratios caused by NaCl and NaHSO_4 are due to both elongation (up to 45.6 and 45.0 nm final length, respectively, at the highest salt concentration) and width reduction (down to 9.8 nm for both salts) of the rods at the same time. On the other hand, the addition

of NaBr into the growth solutions yields shorter and wider rods from 43.0×10.6 nm to 36.8×11.2 nm, resulting in lower aspect ratio crystals. The statistical significance of the different aspect ratios was studied by Welch's t-tests (Table S3.1) and effect size calculations (Table S3.2). These show that our method can fine-tune the aspect ratio of the rods with a precision of 0.1 for most of the range between 3.3 and 4.8 with small and medium effect sizes ($0.10 < d < 0.45$) but statistically significant ($p < 0.05$).

Table 3.1. Summary of the optical and morphological properties of AuNRs synthesized after the addition of Hofmeister salts into the growth solution.

Salt	C (mM)	L-LSPR band maximum (nm)	Aspect ratio	Length (nm)	Width (nm)	Shape impurities* (%)
-	0	884	4.1 ± 0.70	43.0 ± 9.4	10.6 ± 1.2	3
NaNO₃	10	881	4.0 ± 0.64	42.2 ± 7.6	10.6 ± 1.2	5
	20	884	4.1 ± 0.76	42.2 ± 9.8	10.2 ± 1.4	2
	30	915	4.3 ± 0.74	42.4 ± 9.0	9.8 ± 1.2	5
	40	945	4.7 ± 0.69	43.4 ± 7.6	9.2 ± 1.2	3
	50	960	4.8 ± 0.79	42.6 ± 7.8	8.8 ± 1.0	6
NaBr	5	860	3.9 ± 0.76	38.8 ± 9.8	10.0 ± 1.4	4
	10	832	3.6 ± 0.69	37.2 ± 9.2	10.4 ± 1.4	3
	15	816	3.6 ± 0.64	39.8 ± 9.0	11.2 ± 1.6	6
	20	796	3.4 ± 0.60	36.6 ± 7.6	10.8 ± 1.2	5
	25	795	3.4 ± 0.63	36.8 ± 9.4	10.8 ± 2.0	6
NaCl	30	777	3.3 ± 0.66	36.8 ± 10.4	11.2 ± 2.6	9
	10	894	4.2 ± 0.75	42.8 ± 9.2	10.2 ± 1.4	7
	20	900	4.0 ± 0.74	42.4 ± 8.6	10.6 ± 1.2	9
	30	909	4.5 ± 0.77	43.2 ± 9.2	9.6 ± 1.2	4
	40	917	4.5 ± 0.75	43.4 ± 10.0	9.6 ± 1.4	11
NaHSO₄	50	928	4.7 ± 0.77	45.6 ± 9.6	9.8 ± 1.2	5
	10	893	4.2 ± 0.71	43.0 ± 8.2	10.2 ± 1.2	3
	20	896	4.3 ± 0.73	43.4 ± 8.8	10.2 ± 1.2	5
	30	918	4.4 ± 0.79	43.4 ± 9.2	9.8 ± 1.2	7
	40	926	4.5 ± 0.85	43.6 ± 10.0	9.6 ± 1.4	13
50	933	4.6 ± 0.89	45.0 ± 10.0	9.8 ± 1.2	10	

*Shape impurities (%) are defined as the percentage of non-rod shaped nanoparticles in the sample.

In addition, we studied the crystalline structure of AuNRs through HR-TEM and XRD. The fast Fourier transform patterns of all the samples show face centered cubic (fcc) close packing, examined along $[110]$ zone axis (Fig. 3.3).²²² HR-TEM data prove that the AuNRs are single-crystal. Furthermore, it is clear that the rods grow along the $[001]$ direction. Fig. 3.4 shows the XRD diffraction patterns of the samples obtained with the maximum amount of Hofmeister salts. In all the cases the XRD peaks are coherent with the metallic gold where the strongest peaks are (111) and (200) .²²³

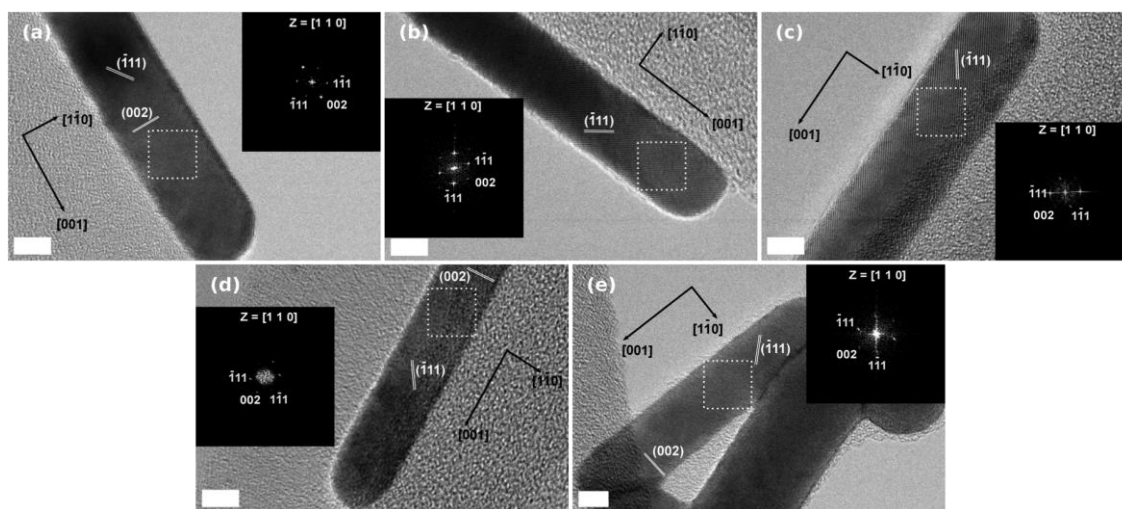


Fig. 3.3. HR-TEM images of AuNRs synthesized (a) without Hofmeister salts, (b) with NaNO_3 (50 mM), (c) with NaCl (50 mM), (d) with NaHSO_4 (50 mM) and (e) with NaBr (30 mM). The insets in the images are the fast Fourier transform patterns of the selected regions. All scale bars are 5 nm.

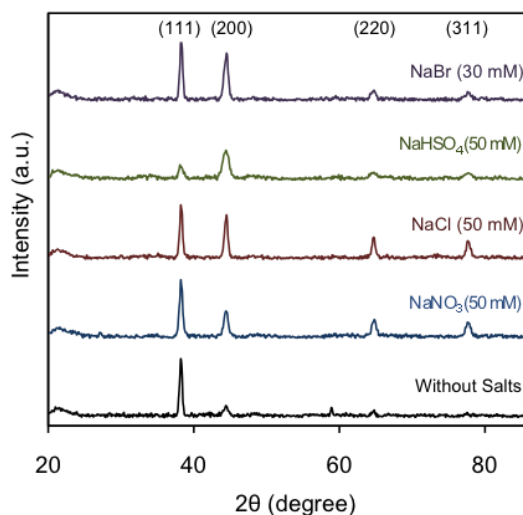


Fig. 3.4. XRD diffraction pattern of AuNRs obtained with and without added Hofmeister salts.

3.3.3 Evolution of CTAB micelles

To clarify the role of the CTAB in the synthesis of AuNRs, it is necessary to characterize the evolution of the CTAB micelles under the different growth conditions. The immiscibility between the aliphatic chain of CTAB and water induces their aggregation in cationic sphere-shaped micelles. It is well established that the electrostatic interactions between surfactant polar heads and charged species modifies the micelle zeta potential,²²⁴ which has been suggested to play an important role on the growth of AuNRs.²⁰⁹ Fig. 3.5a depicts the electrokinetic potential of CTAB micelles in the growth solution after the addition of different Hofmeister salt concentrations. The initial value without added Hofmeister salts is 43.5 mV and it linearly decreases with NaNO_3 , NaCl and NaBr down to 31.1, 33.7 and 37.0 mV, respectively. Interestingly, NaHSO_4 is the salt that reduces the most the micellar zeta potential, down to 27.9 mV.

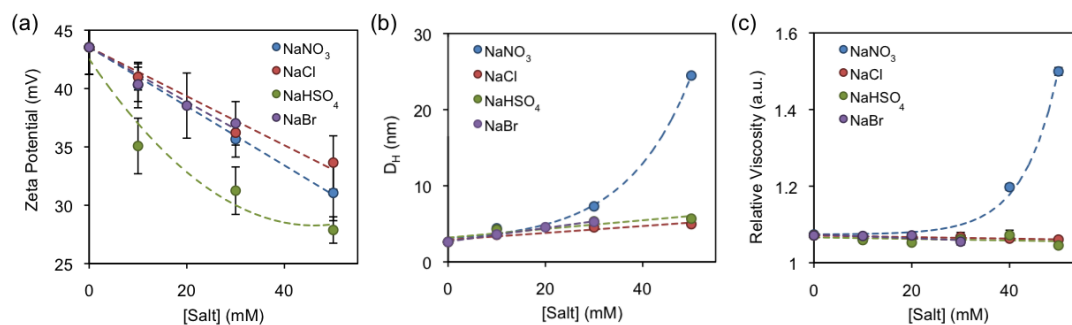


Fig. 3.5. (a) Zeta potential, (b) hydrodynamic diameter and (c) relative viscosity of growth solutions in the presence of added Hofmeister salts.

The interaction between the salts and the CTAB micelles also results on the screening of the electrostatic repulsion between the surfactant polar heads, which alters the surfactant packing and can trigger morphological transitions,²¹⁰ such as spherical-to-wormlike micelle transitions. The micelle morphologies have been mainly characterized by three different kinds of techniques: linear rheology, cryo-TEM and scattering based methods, as they have been deeply discussed in a recent review article.²¹⁰ Fig. 3.5b presents the CTAB micelle hydrodynamic diameter (D_H) in the growth solution as a function of increasing salt content measured by dynamic light scattering (DLS). The D_H increased in all the samples and was proportional to both the salt concentration and position of the anion in the Hofmeister series, suggesting that the salt triggers the micellar growth. Moreover, a larger increase of the D_H was observed for the samples with $[\text{NaNO}_3] > 30$ mM. Such kind of growth is related to the existence of interactions between the micelles, also called semi-diluted regime.

In addition to the DLS measurements, the solution viscosity was also characterised. As soon as the micelle morphology changes from sphere to rod-like or wormlike, the micelles start entangling one to each other (semi-dilute regime), subsequently the solution viscosity increases.²¹⁰ Fig. 3.5c plots the relative viscosity of growth solutions as a function of increasing salt content at 23 °C. Under the growth conditions, the viscosity is only affected by nitrate. Bromide, chloride and bisulphate do not show any significant effect. Interestingly, the viscosity starts increasing at NaNO₃ concentrations above 30 mM. Those are the same concentrations that also show semi-dilute regime by DLS.

Finally, cryo-transmission electron microscopy (cryo-TEM) studies were performed to characterise the micelle morphology in the presence of NaNO₃, NaCl and NaHSO₄ (NaBr was excluded from cryo-TEM study, because bromide anion tunes the rod aspect ratio through different mechanism, which will be described in the next section). The micelle shape has been hypothesized to play an important role on directing the AuNR growth.^{57,225} Fig. 3.6a reveals mostly spherical CTAB micelles (97.9 %) in absence of additional Hofmeister salts, with small percentage of ellipsoidal micelles (2.1 %). Interestingly, although the spherical shape is the most common in all the samples (Fig. 3.6b-g), the addition of salts increases the proportion of ellipsoidal ($1.5 < AR < 3$) and rod-like ($AR > 3$) micelles rather than the size of all micelles (Fig. 3.7), and these shape transitions increases the overall micellar size observed by DLS. Nevertheless, the micelle dimensions seem to slightly increase by the addition of the salts (Table 3.2), however the tendency is not as clear as the increase on the number of non-spherical micelles. These results are in agreement with previously published works, which show co-existence of spherical and wormlike micelles in the same solution.²²⁶ It is worth to mention that the only visualised solution with rod-like micelles is the one with NaNO₃ concentration of 50 mM. This is coherent with the semi-diluted regime observed by DLS and rheological measurements. It is important to note that the cryo-TEM images were taken from the growth solutions after the addition of the Hofmeister salts. As the growth of the AuNRs occurs, some ionic species are consumed such as Ag⁺, AuCl₄⁻ and ascorbate, which is added in the form of ascorbic acid in a second step. Therefore, the variation in their concentration might affect the CTAB micelles. Nevertheless, this seems quite unlikely since their concentrations are very low (*i.e.* the initial concentrations of silver nitrate, chloroauric acid and ascorbic acid are 0.1, 0.5 and 0.5 mM, respectively) and strong Hofmeister anions, such as nitrate, require a concentration of 10 mM to show a significant effect.

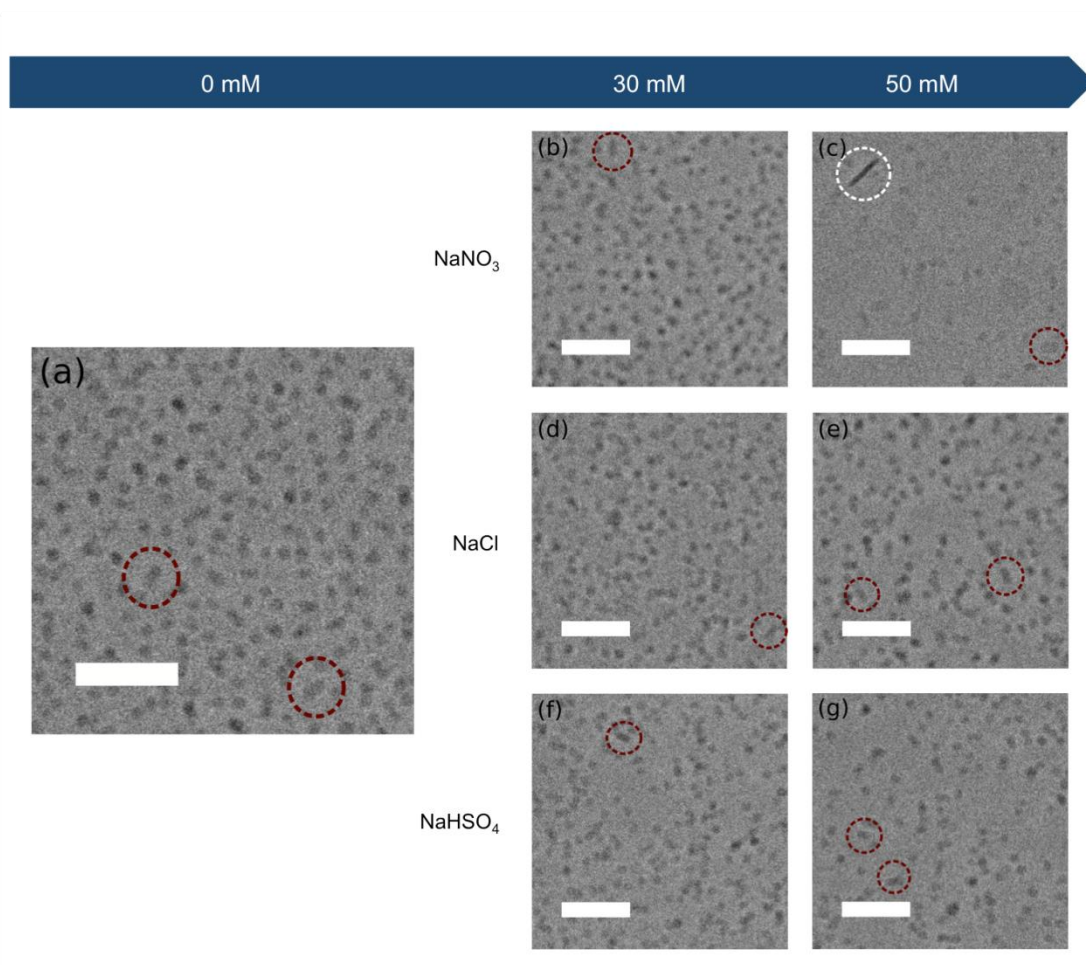


Fig. 3.6. Cryo-TEM images of CTAB micelles in the growth solutions with different amounts of Hofmeister salts: (a) without Hofmeister salts. (b and c) with NaNO_3 , (d and e) with NaCl and (f and g) with NaHSO_4 in order of increasing added concentration (30 and 50 mM). Some ellipsoidal and rod-like micelles have been highlighted in red and white dashed circles, respectively. All scale bars are 50 nm.

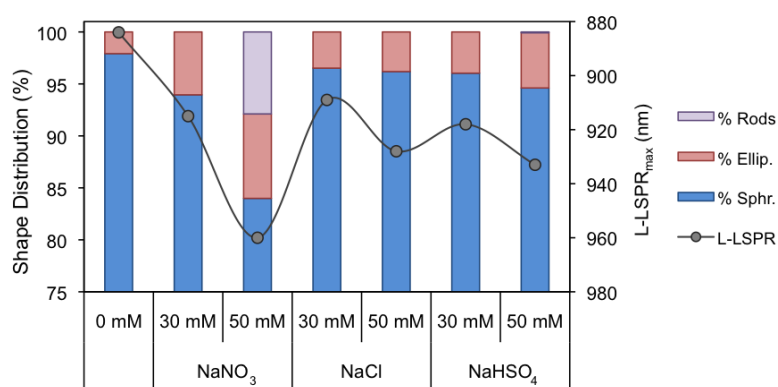


Fig. 3.7. Micelle shape distribution (spherical, ellipsoidal and rod-like micelle) in growth solutions at different Hofmeister salt concentrations and the L-LSPR_{max} of the rods grown in those solutions.

Table 3.2. Summary of the morphological properties of CTAB micelles after the addition of Hofmeister salts into the growth solution. The three micelle morphologies observed by cryo-TEM are spherical (Sph.), ellipsoidal (Ellip.) and rod-shaped (rod).

	[Salt]	<i>NaNO₃</i>			<i>NaCl</i>		<i>NaHSO₄</i>	
		0 mM	30 mM	50 mM	30 mM	50 mM	30 mM	50 mM
Sph.	%	97.9	94	84	96.5	96.2	96	94.6
	Diameter (nm)	2.6	2.8	3.2	2.8	2.8	2.8	2.8
	st dev	1.2	1.4	2	1.4	1.4	1.4	1.4
Ellip.	%	2.1	6	8.1	3.5	3.8	4	5.4
	AR	1.7	1.7	2	1.9	2	1.9	1.8
	st dev	0.1	0.3	0.4	0.3	0.3	0.3	0.3
	Length (nm)	8.2	8.6	10.6	9.4	10.2	9.6	9.6
	st dev	1.4	1.4	2.6	1.8	1.6	1.6	1.4
	Width (nm)	4.8	5	5.4	5	5.2	5	5.2
	st dev	0.8	0.6	1.2	0.6	0.6	0.6	0.6
Rod	%	0	0	7.9	0	0	0	0
	AR	-	-	4.6	-	-	-	-
	st dev			1.5				
	Length (nm)			22.8				
	st dev			9				
	Width (nm)			5				
	st dev			0.8				

3.3.4 Growth mechanism

Despite the silver-assisted AuNR synthesis was developed over a decade ago,⁵⁷ its mechanism still very controversial and poorly understood. Currently, three main mechanisms have been proposed for the nanoparticle anisotropy: 1) the silver is under-potentially deposited at specific gold crystal faces, preventing the crystal growth at those faces;^{18,227} 2) the bromide-silver complex plays a role as face-specific capping agent;^{18,227} 3) CTAB micelles act as soft templates.^{57,225} All three mechanisms are supported by experimental data, making it difficult to choose between the opposed theories. In a recent review,²²⁸ Murphy *et al.* surveyed the current state-of-the-art in AuNR growth mechanism and suggests that the three mechanisms may be correct to some extent, being the final mechanism a combination of all three.

Our work provides a deeper understanding of the AuNR anisotropic growth and addresses some of the unanswered questions described before. In this section we list the most important observations obtained from our experimental data.

First of all, it is worth mentioning that few groups have previously reported the effect of salts in the growth of AuNRs with different results than ours. Mulvaney *et al.* reported the decrease of aspect ratio after adding NaCl into the growth solution.²⁰⁹ However, they were synthesizing penta-twinned AuNRs, which diverge from the single crystal AuNR in different ways, such as structure and synthetic protocol (e.g. low CTAB concentration, 8 mM, and absence of AgNO₃). On the other hand, Yong *et al.* observed increases of the aspect ratio at nitrate and chloride concentrations above 0.1 M.²²⁵ Nevertheless, the rods obtained were highly polydisperse and presented significant shape impurities. That was probably due to the high concentration of salts in the growth solution, which may have induced wormlike micelles.^{229,230}

Second, there seems to be a correlation between the decrease of CTAB zeta potential and the amount of shape impurities. The addition of Hofmeister salts decreased the zeta potential of CTAB micelles to different extents and increased the shape impurities in a certain degree (Fig. 3.8). NaHSO₄ induced the highest electrokinetic decrease, *i.e.* from 43.5 mV down to 27.9 mV, and yielded the highest amount of shape impurities, *i.e.* up to 13 %. NaBr induced a significant amount of spherical nanoparticles too, *i.e.* up to 9 %, however this can be accounted for a different mechanism that will be described later. NaCl presents a highly variable amount of shape impurities and it is difficult to get a solid conclusion. However, the general impurity tendency is smaller than in the first salt. Finally, NaNO₃ is the salt that produces rods with higher shape purity. Even though the syntheses of penta-twinned and single crystal AuNRs follow different synthetic protocols, Mulvaney *et al.* reported a similar observation for the silverless synthesis, where the rod formation depends on *the extremely strong binding* between gold anions and cationic micelles.²⁰⁹ Therefore, the decrease of the micelle zeta potential weakens the electrostatic interaction between the two species and may drop the rod yield. In the aromatic based synthesis,⁵⁸ where organic additives are introduced to the silver-assisted synthesis, the authors hypothesized that a weaker CTAB micelle and gold precursor interaction yields shorter AuNRs. However, we did not observe such a phenomenon except for the bromide, whose case will be discussed later.

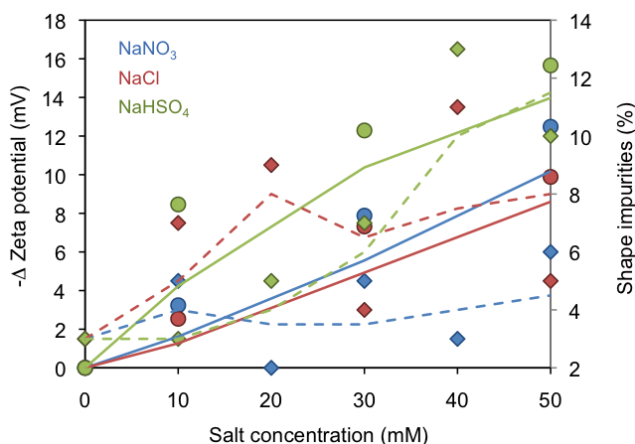


Fig. 3.8. Micelle zeta potential (circle) after the addition of Hofmeister salts in the growth solution and percentage of shape impurities (diamond) after the growth of the rods in those solutions. The moving averages of both zeta potentials and impurities are represented in solid and dashed lines, respectively.

Third, some works have suggested that under AuNR growth conditions,^{57,225} CTAB micelles present rod-shape morphology. Thus, the AuNR anisotropy would be driven by the micelle that acts as a soft template. To the best of our knowledge, this is the first work that has visualized the CTAB micelles under AuNR synthesis conditions by cryo-electron microscopy. The surfactant micelles were mostly spherical in all the cases, with an increasing amount of ellipsoidal micelles ($1.5 < AR < 3$) with the addition of salts. Only the sample with 50 mM NaNO₃ presented rod-like micelles ($AR > 3$), which were significantly smaller than the resulting AuNRs, 22.8×5.0 and 42.6×8.6 nm, respectively. Therefore, the soft template seems unlikely to occur as it was proposed on those works. Nevertheless, Murray *et al.* has recently suggested that the increase of AuNR aspect ratio after the addition of organic additives is coherent with an increase of the surfactant packing parameter (p).⁵⁸ This phenomena is also observed here, where the transition of spherical micelles ($p < 1/3$)²¹⁰ to ellipsoidal and rod-like micelles ($1/3 < p < 1/2$)²¹⁰ after the addition of the salts is consistent with the shift of the AuNR L-LSPR_{max} (Fig. 3.7). Thus, the change on the micellar behaviour, whether the surfactant molecule is directly bond to the gold, to another surface (e.g. under-potentially deposited silver) or in the form of a different surface-active species (e.g. silver-CTAB complex), seems to affect the growth of the rod.

Fourth, the samples with NaBr presented a decrease in their aspect ratio and blue-shift of the LSPR band proportional to the amount of salt, although the salt triggered the overall micellar growth. This anomalous behaviour can be explained by understanding the interaction between the bromide ions and gold. Halides are known to affect the growth of gold nanoparticles through two cooperative pathways.²³¹ (1) Halides anions can complex gold ion derivatives, modifying their potential and solubility and thereby

altering their reduction rate.^{232,233} The reduction potentials of AuCl_2^- , AuBr_2^- and AuI_2^- are 1.154, 0.960 and 0.578 V, respectively.²³⁴ As the lower the standard reduction potential of a complex is, the more difficult it is to be reduced by ascorbic acid. Additionally, the solubility of those complex drops in an order $\text{AuCl}_2^- > \text{AuBr}_2^- > \text{AuI}_2^-$ and the formation of less soluble compounds slows down the reaction.²³⁵ (2) Halides can also bind to the gold surface, blocking the growth of the nanoparticle. The binding strength of the halides increase in the following order $\text{Cl}^- < \text{Br}^- < \text{I}^-$.²³⁶ In addition, Mirkin *et al.* reported that the passivation of the gold surface by halides further disturbs the silver under-potential deposition onto gold surface.²³¹ This halide strong interference on the AuNR growth has been observed for iodide, where low concentrations have been reported reducing AuNRs aspect ratio and high concentrations quenching further and yielding spherical nanoparticles.^{61,237} Thereby, the fact that bromide reduced the aspect ratio of the AuNRs can be explained from the gold–halide interaction point of view. Additionally, we observed a concentration threshold for bromide, *i.e.* 30 mM, like the one reported for iodide, where above that concentration the AuNRs synthesis is completely quenched and spherical particles are mainly obtained. On the contrary, chloride has less capacity to block gold deposition and it did not hinder the growth of AuNRs at the experimental concentrations. Finally, nitrate and bisulphate have been reported displaying very low affinity for gold in comparison to halides,^{236,238} which explains why they did not interfere in nanoparticle growth.

3.4 Conclusions

We demonstrate that a high level of control over the rod dimensions and widely tuneable L-LSPR band can be achieved by adding small amounts of Hofmeister salts into the seed-mediated synthesis of AuNRs. The nature of the tuning depends on the double interaction between the salts with gold and the salts with surfactant micelles. Salting in ions, like thiocyanate and perchlorate, induce the surfactant precipitation and the quenching of the AuNRs formation. Neutral and salting out anions screen the electrostatic repulsion between the surfactant molecule heads, inducing changes on the micellar behaviour. When those anions have low affinity for gold, like nitrate, bisulphate and chloride, their addition yields longer aspect ratio rods. However, anions with high affinity for gold, like bromide, reduce the gold deposition, producing shorter aspect ratio rods. Interestingly, CTAB micelles are mainly sphere-shaped in all solutions. The addition of salt increases the overall micelle size by increasing the non-spherical micelle population, although spherical shape is still the predominant one. Hence, these results provide not just a new strategy for the precise tuning of the optical properties and morphology of Au NRs, but also a deeper understanding of the anisotropic growth mechanism of the nanoparticles.

3.5 Annex

Table S3.1. *p*-values obtained by Welch t-test (unequal variances t-test), to study if the differences between aspect ratios are statistical significant. The Hofmeister salts have been abbreviated as B (NaBr), N (NaNO₃), C (NaCl) and S (NaHSO₄). The number next to the salt is the concentration (mM) added to the growth solution.

AR/AR	3.3	3.4	3.6	3.9	4.0	4.1	4.2	4.3	4.4	4.5	4.6	4.7	4.8											
[salt]/[salt]	B 30	B 25	B 20	B 15	B 10	B 5	N 10	C 20	0	N 20	C 10	S 10	N 30	S 20	S 30	C 30	C 40	S 40	S 50	N 40	C 50	N 50		
3.3	B 30	0.0250	0.0202																					
	B 25		0.0000	0.0000																				
3.4	B 20			0.0000	0.0000																			
	B 15				0.0000																			
3.6	B 10					0.0000																		
	B 5						0.0011	0.0007																
3.9	N 10								0.0051	0.0009														
	C 20								0.0041	0.0006														
4.0	0										0.0102	0.0052												
	N 20										0.0036	0.0013												
4.1	C 10												0.0073	0.0026										
	S 10												0.0034	0.0006										
4.2	N 30														0.0021									
	S 20															0.0002								
4.3	S 30																0.0158	0.0256	0.0007					
	C 30																	0.0158						
4.4	C 40																		0.0256					
	S 40																			0.0007				
4.5	S 50																				0.0023	0.0019		
	N 40																					0.0021		
4.6	C 50																						0.0017	
	N 50																							0.0017

Table S3.2. Cohen's α -values calculated to study the standardised differences between aspect ratios. The Hofmeister salts have been abbreviated as B (NaBr), N (NaNO₃), C (NaCl) and S (NaHSO₄). The number next to the salt is the concentration (mM) added to the growth solution.

AR/AR	3.3	3.4	3.6	3.9	4.0	4.1	4.2	4.3	4.4	4.5	4.6	4.7	4.8										
[salt]/[salt]	B 30	B 25	B 20	B 15	B 10	B 5	N 10	C 20	0	N 20	C 10	S 10	N 30	S 20	S 30	C 30	C 40	S 40	S 50	N 40	C 50	N 50	
3.3	B 30	0.16	0.16																				
	B 25		0.31	0.30																			
3.4	B 20		0.32	0.31																			
	B 15			0.42																			
3.6	B 10				0.41																		
	B 5					0.14	0.13																
4.0	N 10						0.15	0.14															
	C 20						0.14	0.13															
	0								0.14	0.14													
4.1	N 20								0.13	0.13													
	C 10										0.13	0.14											
4.2	S 10											0.14	0.14										
	N 30												0.13	0.14									
4.3	S 20													0.13	0.13								
	S 30														0.13	0.13	0.13	0.12					
	C 30																	0.12					
4.5	C 40																		0.12				
	S 40																			0.12			
4.6	S 50																				0.13	0.13	
	N 40																					0.13	0.13
4.7	C 50																						0.13
4.8	N 50																						0.13

Chapter 4

Growth of Anisotropic Gold Nanoparticles in Photoresponsive Fluid for UV Exposure Sensing and Erythema Prediction

Photoresponsive fluids have been widely employed in nanoscale and microscale technologies, due to their light-tunable properties. Here, we propose using the distinct physicochemical properties of an ultraviolet-responsive fluid to tailor the growth of anisotropic gold nanoparticles. The direct dependency between the ultraviolet (UV) irradiation and the resulting nanoparticle optical properties, renders the system to be useful as an *in situ growth sensor* for UV exposure. The UV exposure levels used in the synthesis are accurately correlated to the UV minimal doses to produce erythema to different skin types, expanding the application of this system as an easy-to-use and inexpensive sunlight-indexing tool for monitoring the dangerous level of skin exposure.

4.1 Introduction

Over the last decade, metallic nanoparticles have captured great scientific attention due to their wide biomedical applications, such as photothermal therapy,^{192,193,195} drug delivery,¹⁹⁶ imaging^{18,197–199} and sensing.^{200,202,239} Their unique optical and electrical properties rely on the collective oscillation of the electrons in the conduction band called surface plasmon resonance (SPR),¹¹² which can be customized by changing the nanoparticle size²⁶ and shape.²⁴⁰ Due to a great advancement of synthetic methods, a broad range of non-spherical metallic nanoparticles have been obtained, e.g. rod,^{21,194} star,^{64,65,241} shell,^{242,243} prism,^{244,245} worm²⁴⁶ and others.²⁴⁷ Even though each morphology requires a different synthetic route, few of them use hexadecyltrimethylammonium bromide (CTAB) as a main symmetry-breaking component.²⁴⁷ CTAB is a cationic surfactant that self-assemble in spherical micelles in water.⁵⁹ Interestingly, CTAB micelle behaviour can be modified by introducing additives such as salts, co-surfactants or organic compounds.²⁴⁸ Controlling anisotropic gold nanoparticle morphology, particularly AuNRs, was initially achieved by regulating the presence of silver cations in solution.⁵⁷ In recent years, it has been accomplished by modifying the rheological behaviour of the surfactant with the addition of organic⁵⁸ or inorganic salts⁵⁹ into the CTAB-containing growth solution. When a photoresponsive organic compound is added to the CTAB solution, a photorheological fluid can be obtained.^{249–251} These smart fluids present light-tunable properties, which we hypothesize can control the growth of anisotropic nanoparticles by irradiating the reaction mixture before the gold reduction takes place. Previously, the photochemical synthesis of AuNRs had been accomplished by a different principle, *i.e.* introducing acetone into the growth solution and irradiating it with UV light for 30 h.²⁵² Although the mechanism is still not clear, it has been suggested that acetone acts as catalyst in the gold reduction.²⁵³ Later, the long reaction time was improved by combining a chemical reduction step with the photoirradiation.²⁵⁴ However, this double-reduction procedure did not yield the larger rods with the longer the irradiation time. The rod aspect ratio initially increased with the irradiation time until reaching a maximum, after which the rod length started to decrease.

Gold nanoparticles have been abundantly used in colorimetric sensing, due to their strong extinction coefficients in the visible and near-infrared wavelength range.²⁰⁰ Traditional approaches measure the shift of the SPR band as a consequence of the analyte-induced nanoparticle aggregation. Those sensors can be generally classified under cross-linking^{119,255–257} or non-cross-linking (*i.e.* electrostatic) principles,^{201,258,259}

depending on the aggregation driving force. Nevertheless, these sensors using as-prepared nanoparticles present several drawbacks such as complex post-synthesis surface modifications in the case of cross-linking based sensors and weak binding interactions, which may be impaired by the buffer or the medium-containing species, and low specificity in the case of non-cross-linking based sensors. Therefore, recent efforts have been made in order to develop a totally new analytical approach, where the nanoparticles are not synthesized beforehand and later exposed to the analyte, but synthesized in the presence of the analyte, and their growth is driven by the analyte concentration that is termed as *in situ* growth sensing. So far the most successful design of such system is the gold nanoparticle-based enzyme-linked immunosorbent assay (ELISA) for cancer markers developed by de la Rica et al.²⁶⁰ In this design, non-aggregated spherical or aggregated non-spherical gold nanoparticles are produced under enzymatic interaction, depending on the prostate-specific antigen or p24 levels. Since its publication, this sensing principle has been further applied to other biomarkers.^{261,262} Coronado-Puchau et al. were able to correlate the growth of AuNRs to the levels of a nerve gas analogue by enzymatically-quenching the nanorod growth.²⁶³ Even though these designs that combine the synthesis and sensing in a single step are superior to the traditional approaches, they all rely on enzyme-based signal generation, which increases the design complexity and experimental times.

Nanotechnology and nanosensing have the potential to benefit several biomedical fields such as sunlight-related disease prevention.²⁶⁴ The impact of UV radiation (UVR) on human health has become a major concern according to World Health Organization (WHO), due to the strong increase on skin cancer incidence and ozone depletion over the last decades.²⁶⁵ The exposure of skin to solar UVR produces erythema,²⁶⁶ a skin inflammation commonly known as “sunburn”. The UVR damages the epidermal DNA, mostly producing pyrimidine dimers.²⁶⁷ Those lesions are premutagenic and have been linked to many UV-related diseases, such as immunosuppression.²⁶⁷ Even though the DNA integrity is generally restored by repair processes and the damaged cells are eliminated by apoptosis,²⁶⁸ the malfunction of those mechanisms may lead to melanoma.²⁶⁹ Nevertheless, an opposite health issue related to the lack of UV exposure has recently emerged as widespread threat, *i.e.* vitamin D insufficiency, which is directly linked to several bone disease, such as rickets and osteomalacia.²⁷⁰ Therefore, novel and inexpensive systems capable of measuring human exposure to UV are required.

In this work, we study the effect of growing anisotropic gold nanoparticles, *i.e.* nanorods and nanoworms, in a photoresponsive medium. We demonstrate that the UV irradiation induces physical and chemical changes on the growth solution, which

ultimately controls the nanoparticle dimensions. Furthermore, we apply those UV-dependent syntheses as enzyme-free in situ growth sensors for solar UVR exposure and erythema prediction.

4.2 Experimental section

4.2.1 Materials

The following products were used as received. Hydrogen tetrachloroaurate (HAuCl_4 , 99.99% trace metals basis, 30 wt. % in dilute HCl), silver nitrate (AgNO_3 , 99%), hydrogen chloride (HCl, 37% wt in water), L-ascorbic acid (crystalline), sodium borohydride (NaBH_4 , 98%) *ortho*-methoxycinnamic acid (OMCA, predominantly *trans*, 98%) were purchased from Sigma-Aldrich. Hexadecyltrimethylammonium bromide (CTAB, >98%) and *cis-ortho*-methoxycinnamic acid (99%) were purchased from Tokyo Chemical Industry.

All the water employed in the experiments was obtained with a Milli-Q Integral 5 system.

4.2.2 Sample irradiation

UV irradiations. 7.5 ml solutions made of CTAB (133.3 mM) and *trans*-OMCA (6.7 mM) and contained in sealed glass vials were irradiated in a 400 W UV chamber (DYMAX light curing system, Model 2000 Flood) with maximum irradiation from 300 to 450 nm. The irradiations were carried in air atmosphere.

Solar-simulated irradiations. Solutions with the same composition as in the UV irradiation were irradiated in a 400 W solar simulator (Honle UV Technology, model SOL 2). The irradiations were carried in air atmosphere.

4.2.3 Synthesis of AuNRs

Synthesis of seeds. The reaction was performed at 23 °C. The CTAB solution (5 ml, 0.2 M) was added to a 5.0 mL solution of HAuCl_4 0.5 mM. While the mixture was being vigorously stirred, 0.6 mL of ice-cold NaBH_4 10 mM were added at once. The seed solution was stirred for 30 s and was left undisturbed for 1 h. Then, the seeds were immediately used to synthesize the gold nanorods.

Synthesis of rods. 250 μL of AgNO_3 (4 mM) were added to the previously irradiated solution (7.5 ml, 133.3 mM CTAB and 6.7 mM *trans*-OMCA). The solution was kept undisturbed for 15 min, after which 2.5 mL of HAuCl_4 (2 mM) were added. After slow

stirring, ascorbic acid (60 μL , 79 mM) was introduced into the growth solution, which lost its orange colour and yielded a colourless solution, because of the reduction of Au^{3+} to Au^{1+} . The mixture was vigorously stirred for 30 s and 60 μL of the seed solution were added. Finally, the growth solution was vigorously stirred for 30 s and left undisturbed for 12 h. The gold nanorods were isolated by centrifugation at 8000 rpm for 15 min followed by removal of the supernatant twice. The precipitate was re-dispersed in 10 ml of Milli-Q water, yielding a pale red solution.

4.2.4 Synthesis of AuNWs

The reaction was performed at 23 °C. 70 μL of freshly prepared NaOH (1 M) were added to the irradiated solution (7.5 ml, 133.3 mM CTAB and 6.7 mM *trans*-OMCA) under vigorous stirring. 2.5 mL of HAuCl_4 (1 mM) were immediately introduced into the growth solution, changing the colour solution to pale yellow. While keeping the vigorous stirring, ascorbic acid (34 μL , 79 mM) was added, yielding a colourless solution. The loss of the colour was followed by the addition of 250 μL of AgNO_3 (4 mM). The final solution was stirred for 30 s and left undisturbed for 12 h. A fast change in the colour from colourless to dark red-brown occurs few minutes after the addition of the last reagent, indicating the formation of AuNWs, which were isolated by centrifugation at 7000 rpm for 10 min followed by removal of the supernatant twice. The precipitate was re-dispersed in 10 ml of Milli-Q water, yielding a red-brown solution.

4.2.5 Simulated sunlight calculations

The solar-simulated irradiance was measured with a solar meter (DAYSTAR DS-05 model; Daystar, inc.) and optical filters. The UV solar-simulated irradiance of the lamp is 73 W/m^2 , which is in good agreement with the ASTM-G173 standard, *i.e.* UV Sun irradiance of 63 or 91 W/m^2 depending if considering diffusion radiation.²⁷¹ The non-erythemally weighted UV radiant exposure (J/m^2) was calculated by integrating irradiance over exposure times. For erythemally weighted, the solar-simulated irradiance was decomposed in single irradiances for every wavelength by assuming that the solar lamp and sun irradiances have the same wavelength profile. The global sun irradiance from ASTM-G173 standard was used as a reference. The erythemally weighted irradiance was calculated by applying the CIE-standard erythral weight

function to the lamp irradiance. Finally, the irradiance was integrated over time to obtain the erythemally weighted exposure.

4.2.6 Characterization

Transmission electron microscopy (TEM) images and high-resolution TEM (HR-TEM) images were obtained with a JEM-2100 microscope operating at 200 kV. The optical extinction spectra were recorded using a Spectramax M2/M2e UV/Vis/NIR spectrophotometer. The growth of the nanoparticles was studied with a Cary 60 UV-Vis from Agilent Technologies. The dynamic light scattering (DLS) measurements were performed with a Zetasizer Nano Z from Malvern Instruments. The X-ray diffraction (XRD) measurements were performed with D8 Discover Gadds. pH measurements were recorded with an Orion Star A111 Benchtop meter from Thermo Scientific. The IR spectra were acquired from solid samples with a FTIR spectrometer (Perkin Elmer Spectrum 2000 with Autoimage). The samples were irradiated in ethanol, dried and grinded with potassium bromide, followed by film pelletization before the measurements. The $^1\text{H-NMR}$ spectra were collected with a Bruker DRX 400 MHz.

4.3 Results and discussion

4.3.1 Growth of AuNRs

AuNRs are commonly synthesized by seed-mediated methods, where gold salts are reduced in the presence of a cationic surfactant (*i.e.* CTAB) and small gold nanoparticles that act as seeds.^{57,203} When a photosensitive organic acid or salt, which photoisomerizes, is added into a CTAB solution, the organic molecules interact differently depending on the isomer geometry, providing distinctive rheological properties.^{249–251} OMCA is one of the rare cases, where its photoisomerization (from *trans* to *cis* form, Fig. 4.1) is irreversible and the rheological changes are only one-way and triggered by the absorption of UV light.²⁵¹

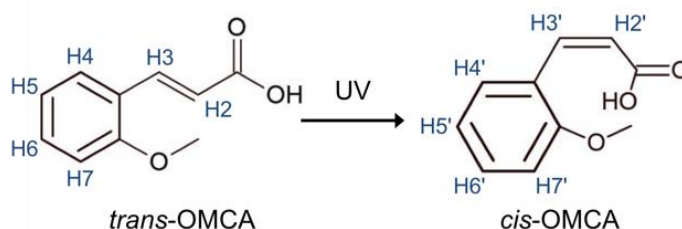


Fig. 4.1. Photoisomerization of OMCA from *trans* to *cis* form.

The effect of UVR on the growth of AuNRs in a photoresponsive fluid, made of CTAB and *trans*-OMCA (final concentrations of 100 and 5 mM, respectively), has been studied. The growth of AuNRs following the traditional seed-mediated protocol requires acidic conditions,⁵⁷ which hinders the solubility of OMCA in water. A concentration of 5 mM was found to be optimal, since bigger amounts of OMCA precipitated over time. Identical solutions were irradiated with UV light for different exposure times, before being used in the synthesis of the nanoparticles. The TEM images of the rods grown in those solutions are presented in Fig. 4.2A. Even though the aspect ratio of AuNRs increases from 3.5 to 3.9 with increasing UVR, the length and the width don't follow a clear tendency with the exposure time (Fig. 4.2B). Interestingly, AuNRs obtained after 15 min of irradiation present two different populations. One made of bigger rods ($38.0 \pm 6.0 \times 9.8 \pm 1.0$ nm) and the other composed of rice-shaped rods ($31.8 \pm 7.2 \times 8.0 \pm 1.2$ nm) with aspect ratios of 3.9 ± 0.6 and 4.0 ± 0.7 , respectively. This may suggest a complex combination of phenomena that results on the tuning of the AuNR aspect ratio. The underlying mechanism is thoroughly discussed in 4.3.3 *Insights into the growth mechanism and the role of OMCA* section of this chapter. The statistical significance of the different aspect ratios

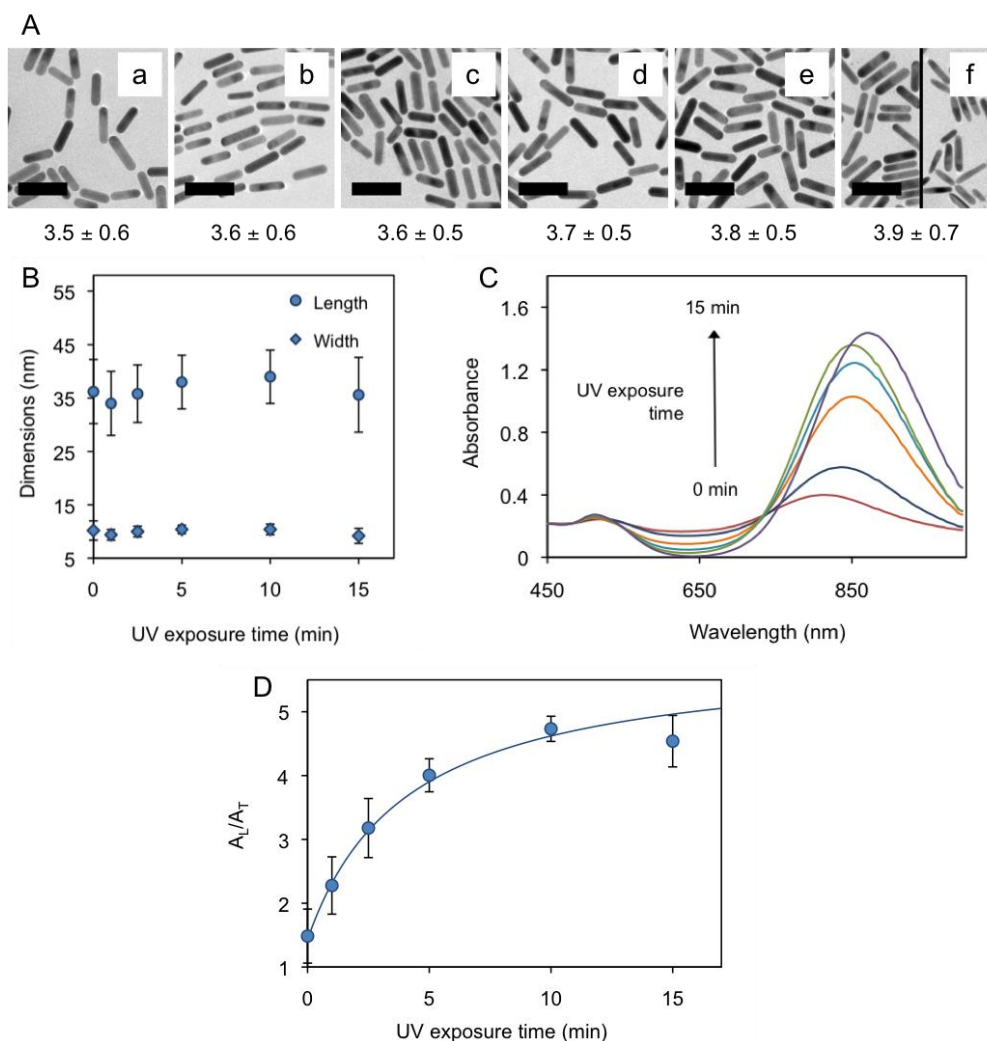


Fig. 4.2. (A) TEM images of AuNRs grown in the photoresponsive fluid after UV irradiation for (a) 0, (b) 1, (c) 2.5, (d) 5, (e) 10 and (f) 15 min. AuNR aspect ratios are displayed below the TEM images. Scale bars represent 50 nm. (B) Plot of the length and width of the grown AuNRs. (C) Corresponding absorbance spectra of the AuNRs. (D) Variation of the ratio between the AuNR longitudinal (AL) and transversal (AT) LSPR bands as a function of UV exposure time.

has been evaluated by Welch's t-tests (Table S4.1) and the effect size (*i.e.* standardized measure of the strength of the effect) by Cohen's *d* calculations (Table S4.2). These analyses show the aspect ratio of the rods increase with a precision of 0.1 for the range between 3.5 and 3.9 with small Cohen's *d* values ($0.16 \leq d \leq 0.20$) but statistical significance ($p < 0.05$). In other words, even though the effect of the UVR on the aspect ratio is small, it is statistically significant. The change of the rod morphology contributes to increase and shift of the longitudinal localized surface plasmon resonance (L-LSPR) band from 813 up to 862 nm (Fig. 4.2C). Fig. 4.2D presents the intensity ratio between the two LSPR bands (A_L/A_T) of the AuNRs grown after different irradiation times. The ratio values shift from 1.4 to 4.7 with increasing UVR times, and saturation is reached after 10 min of irradiation. It is important to note that the strong shift of A_L/A_T by UVR suggests that the variation of the AuNR's optical properties can

be used as transducer signal for robust UV-sensing. Nevertheless, the L-LSPR bands in all the nanoparticle solutions are in the near-IR region, outside of the visual spectrum. Thus, those changes are not detectable by naked eye and require UV-Vis spectrometer as quantitative detection system.

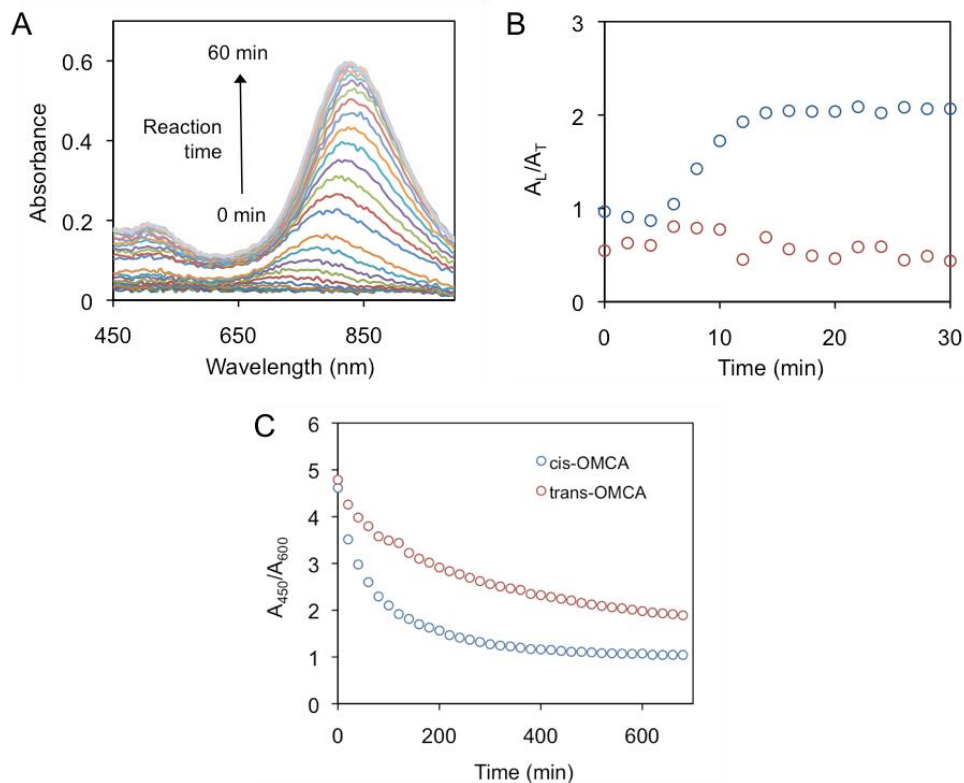


Fig. 4.3. (A) Absorbance spectra of the AuNRs grown in the photoresponsive fluid over the time. (B) Correlation between the intensity ratio of the AuNR longitudinal (AL) and transversal (AT) LSPR bands with reaction time in the presence (blue) and absence (red) of 5 mM *trans*-OMCA. The UV irradiation time is 0 min. (C) Variation of Au^{3+} absorbance ratio at 450 (characteristic absorbance band of Au^{3+}) and 600 nm (reference point), as a function of time in the presence of (blue) *cis*-OMCA or (red) *trans*-OMCA under AuNR growth conditions.

The growth kinetics of the rods was studied by UV-Vis spectroscopy. Fig. 4.3A presents the evolution of AuNR growth in the presence of 5 mM *trans*-OMCA. A wide plasmon band appears around 720 nm after 16 min of reaction. It red-shifts and its intensity increases as the reaction progresses. The growth of the AuNRs is completed after 54 min and no further changes are observed in the spectrum. Interestingly, standard protocols for the synthesis of AuNRs (*i.e.* in absence of *trans*-OMCA) require higher amounts of ascorbic acid, which is the essential reagent for the gold reduction. OMCA presents mild reducing behaviour, which may play a role in the reduction of gold salts. Therefore, we compared the AuNR growth kinetics in the presence and absence of *trans*-OMCA. Fig. 4.3B shows the intensity ratio between the two AuNR LSPR bands (A_L/A_T) against the experimental time. In the presence of *trans*-OMCA, AuNR growth takes 54 min to complete, as previously described. On the other hand, AuNRs don't

grow in the absence of *trans*-OMCA. We hypothesize that *trans*-OMCA contributes to the gold reduction, and ascorbic acid at 79 mM (60 μ l) by itself is not enough to reduce the gold salts to metallic gold. It is worth to mention that several aromatic compounds have been reported reducing gold salts in the formation of gold nanoparticles.^{272–275} To confirm this hypothesis, a growth solution (containing 0.5 mM HAuCl₄) was left undisturbed without adding ascorbic acid and seeds. Fig. 4.3C shows the slow reduction of Au³⁺ to Au⁺ in the presence of *trans* and *cis*-OMCA (the difference between the reduction behaviour of both isomers and its consequences are discussed in 4.3.3 *Insights into the growth mechanism and the role of OMCA* section). Au⁺ is not further reduced to metallic gold, as observed by the absence of plasmon band. Interestingly, OMCA by itself requires significantly larger times to reduce Au³⁺ to Au⁺ than ascorbic acid, *i.e.* 10 h (Fig. 4.3C) and few seconds (Fig. 4.3B), respectively. AuNR growth and gold reduction kinetics suggest that even though OMCA's contribution to reduce the gold salts is very small, it is essential for the final growth of the rods.

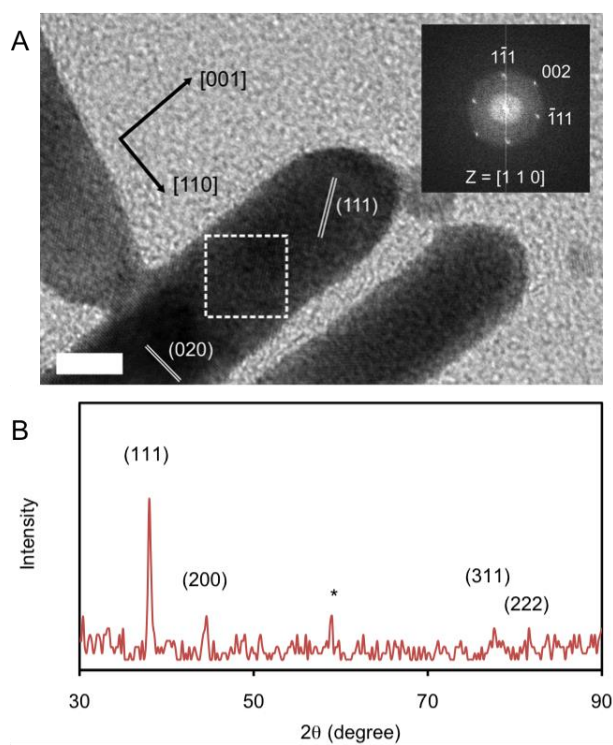


Fig. 4.4. (A) HR-TEM image of AuNRs synthesized in the photoresponsive fluid. The inset in the image is the fast Fourier transform pattern of the selected region. Scale bar represents 5 nm. (B) XRD pattern of AuNRs obtained in the photoresponsive fluid. Asterisk denotes a substrate peak (Si (444)).²⁷⁶ The UV irradiation time is 0 min.

Finally, the crystalline structure of the nanoparticles was characterized. HR-TEM images indicate that the rods are single-crystal, growing along the [001] direction (Fig. 4.4A). The analysis of the fast Fourier transform (FFT) obtained from the HR-TEM images shows face-centered cubic (fcc) spot pattern, acquired along the [110] zone

axis. Furthermore, the XRD patterns present strong peaks at (111) and (200), which are coherent with metallic gold (Fig. 4.4B).

4.3.2 Growth of AuNWs

The reducing behaviour of ascorbic acid is pH-dependent.²⁷⁷ When the pH of the growth solution is increased (pH \approx 11), ascorbic acid can completely reduce Au^{3+} to Au^0 without the presence of seeds. Due to the fast reduction kinetics, CTAB cannot efficiently break the nanoparticle symmetry and effectively induce the growth of AuNRs.²⁷⁸ Nevertheless, twisted gold nanowires (*i.e.* AuNWs) can be formed at that basic pH under highly controlled conditions.²⁴⁶ It has been proposed that CTAB's higher affinity for {100} and {110} facets induces an anisotropic coverage of the newly formed nanoparticles, originating electrostatic interactions among them and promoting their oriented attachment.²⁴⁶ The deposition of reduced gold on top of those assembled nanoparticles yields the final AuNWs.

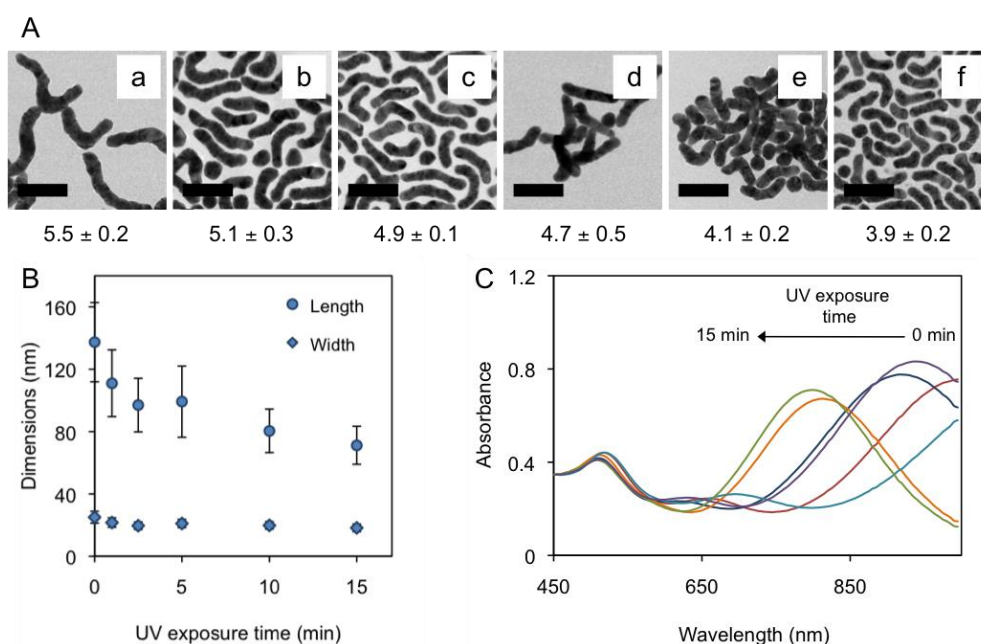


Fig. 4.5. (A) TEM images of AuNWs grown in the photoresponsive fluid after (a) 0, (b) 1, (c) 2.5, (d) 5, (e) 10 and (f) 15 min of UV irradiation. AuNW aspect ratios are displayed below the TEM images. Scale bars represent 100 nm. (B) Plot of the length and width of grown AuNWs. AuNW length is defined as the distance between the two longitudinal ends, if the AuNW was completely extended. (C) Absorbance spectra of AuNWs grown in the photoresponsive fluid after 0, 1, 2.5, 5, 10 and 15 min of UV irradiation.

To study the growth of AuNWs in a photoresponsive fluid, several solutions with same composition (*i.e.* final concentration of 100 mM CTAB and 5 mM *trans*-OMCA) were exposed to UVR for different times. Those solutions were lately used to synthesize the AuNWs shown in Fig. 4.5A. The aspect ratio of the worms decreases from 5.5 to 3.9

upon 15 min of irradiation. Interestingly, this is the opposite phenomenon that the one observed for AuNRs, where their aspect ratio increases with UVR. Those variations of the aspect ratio are statistically significant ($p < 0.05$, Table S4.3) with big Cohen's d values ($d \geq 1.00$, Table S4.4). Both length and width decrease upon UVR exposure, from 137.4 to 71.2 nm and from 25.0 to 18.2 nm, respectively (Fig. 4.5B). Due to the decrease in the aspect ratio, the L-LSPR band shifts from above 995 to 800 nm (Fig. 4.5C).

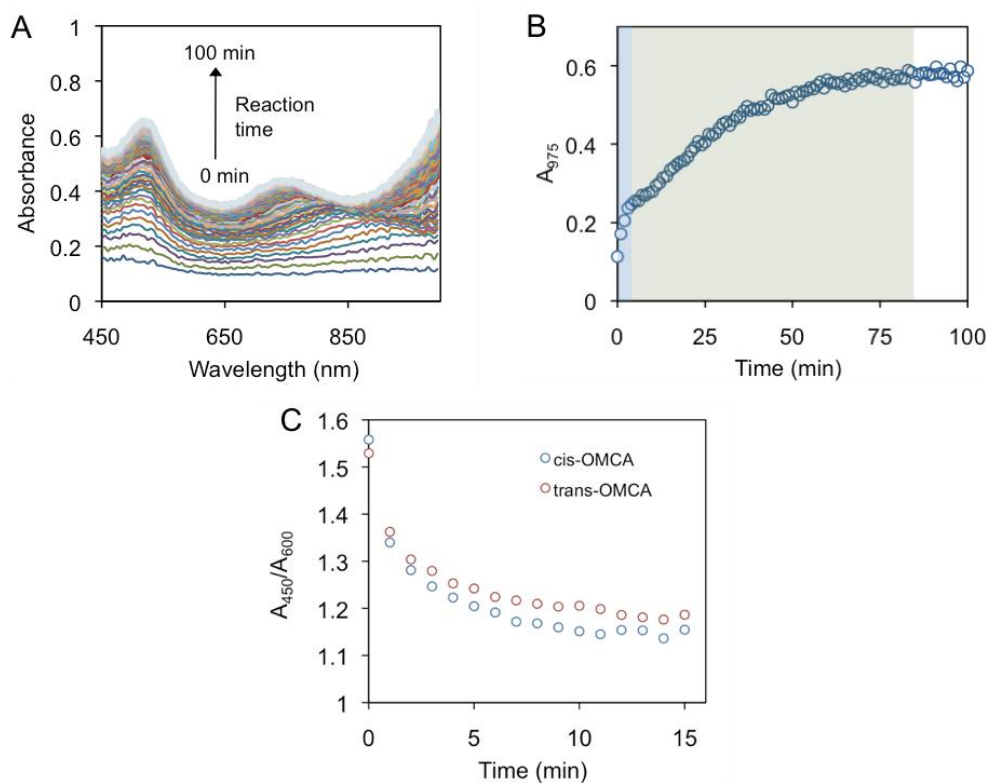


Fig. 4.6. (A) Absorbance spectra of the AuNWs grown in the photoresponsive fluid over the time (from 0 to 100 min). (B) Correlation between the absorbance intensity at 975 nm against reaction time. The two phases of AuNW growth, *i.e.* fast formation of the plasmon bands and their slow increase, are highlighted in blue and green, respectively. The UV irradiation time is 0 min. (C) Variation of Au³⁺ absorbance ratio at 450 and 600 nm, as a function of time in the presence of (blue) *cis*-OMCA or (red) *trans*-OMCA under AuNW growth conditions.

The growth of AuNWs studied by UV-Vis spectroscopy presents two clear phases. The first one is the fast formation of a broad plasmon band around 500 nm, which indicates the growth of gold nanocrystals above 2 nm in size,²⁷⁹ and small L-LSPR band within the first 2 min of reaction (Fig. 4.6A). In a second phase the AuNWs start growing, as indicated by the increase of both plasmon bands, in a slower process that lasts around 83 min (Fig. 4.6B). It is worth mentioning, that the appearance of the first plasmon band is significantly faster in the case of AuNWs than in the AuNRs, being 30 s and 16 min, respectively. Nevertheless, the total growth time for AuNRs is shorter than the one for AuNWs, being 54 and 85 min, respectively. This observation suggests that,

although the initial formation of nanoparticles in the AuNW synthesis is fast, the nanoparticle oriented attachment and further gold deposition on top of them is a remarkably slower process.

In the previous section we proved that OMCA presents a pivotal role in the reduction of gold salts in AuNR synthesis, together with ascorbic acid. Here, we performed the same study under AuNW growth conditions (Fig. 4.6C). We found that total reduction of Au^{3+} to Au^0 occurs after 15 min of reaction in absence of ascorbic acid. This is significantly faster than the reduction occurred under AuNR growth conditions (*i.e.* 10 h). We hypothesize that the faster reduction kinetics is the result of two factors: 1) Stronger reducing power of OMCA at higher pH (*i.e.* cinnamic acid family presents stronger reducing capabilities at higher pH).^{280–282} 2) the lower concentration of Au^{3+} in solution. Nevertheless, the same as observed for AuNR synthesis, OMCA is insufficient to completely reduce gold salts to metallic gold and nanoparticles don't grow in solution. This is confirmed by the absence of plasmon band around 500 nm.

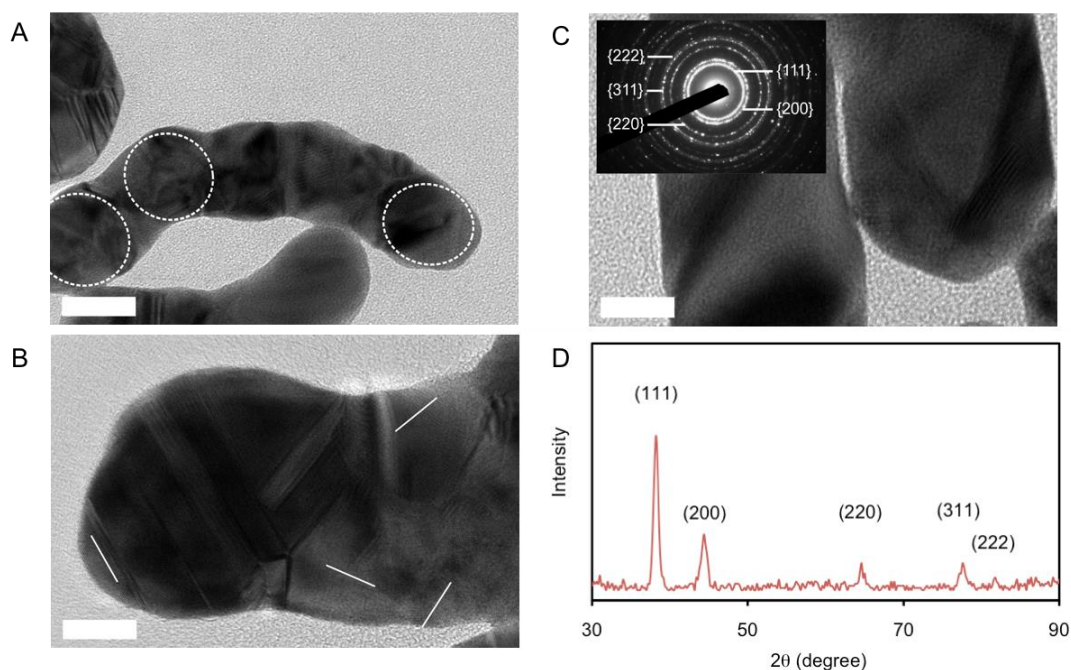


Fig. 4.7. (A) TEM image of the AuNWs. The circles highlight the areas of different domains. Scale bar represents 10 nm. (B) HR-TEM image of AuNW with different atomic lattice directions highlighted in white. Scale bar represents 10 nm. (C) HR-TEM image of AuNWs synthesized in the photoresponsive fluid. The inset in the image is the fast Fourier transform pattern of the AuNW. Scale bar represents 5 nm. (D) XRD pattern of AuNWs obtained in the photoresponsive fluid. The UV irradiation time is 0 min.

Another important information concerning the AuNW growth is observed in the TEM images (Fig. 4.7A). As Ahmed *et al.* had previously reported,²⁴⁶ AuNWs present distinguishable domains, which are most likely formed from the attachment of different nanoparticles. HR-TEM images show that the different domains present indeed

different crystal orientation (Fig. 4.7B). The nanoworm polycrystallinity is further confirmed by the ring structure in the FFT obtained from the HR-TEM images (Fig. 4.7C). Finally, the XRD pattern is coherent with the electron diffraction pattern, showing two strong peaks at (111) and (200) and three smaller at (220), (311) and (222), which are characteristic of metallic gold (Fig. 4.7D).

4.3.3 Insights into the growth mechanism and the role of OMCA

The experimental results of the previous sections prove that UV light can affect the morphology of anisotropic gold nanoparticles grown in a photoresponsive fluid. In this section we list the main observations that will lead to the understanding of the mechanism behind this phenomenon.

First, OMCA photoisomerization was characterized by UV-Vis spectroscopy. Fig. 4.8A presents the spectra of solutions containing 100 mM CTAB and 5 mM *trans*-OMCA after irradiation with UV light. The two absorbance peaks blue-shift and their absorbance intensities decrease upon irradiation, indicating that the photoisomerization from *trans* to *cis* occurs. Interestingly, not all *trans*-OMCA is converted to its *cis* isomer, and the photostationary equilibrium is reached when around 83% of all OMCA molecules are in *cis* form. This is in agreement with previous literature values.²⁵¹ The spectra of both isomers were also recorded in absence of CTAB and similar results are observed (Fig. 4.8B). FTIR and NMR spectroscopies were used to further characterise the photoisomerization. The FTIR spectra of *trans* (after being irradiated with UV light for 0, 5, 10 or 15 min) and *cis*-OMCA were acquired. *Trans* and *cis* isomers can be distinguished by the position of their acrylic out-of-plane =C-H bending bands (γ =C-H)²⁸³, which are located at 879²⁸⁴ and 837 cm⁻¹,²⁸⁵ respectively. In addition, *cis*-OMCA presents a characteristic ring breathing band (RB) around 793 cm⁻¹.²⁸⁵ Fig. 9A shows

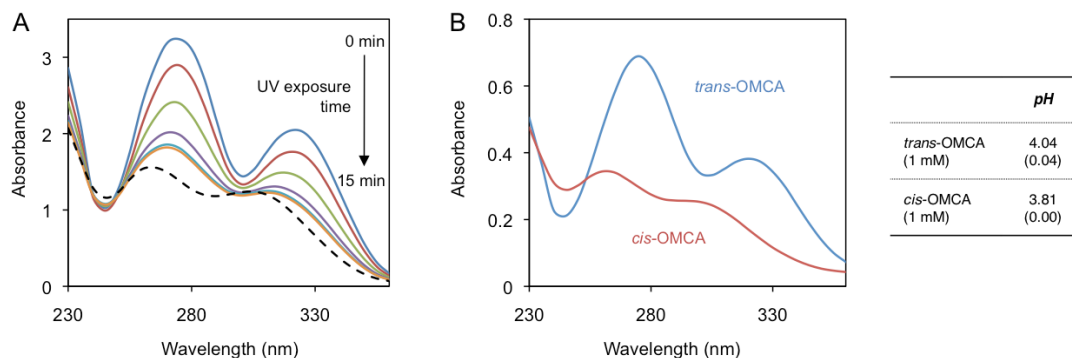


Fig. 4.8. (A) Absorbance spectra of *trans*-OMCA (in a solution made of 100 mM CTAB and 5 mM *trans*-OMCA) after being irradiated with UV light for 0, 1, 2.5, 5, 10 and 15 min. The spectrum of *cis*-OMCA (dashed line) is plotted for reference. (B) Absorbance spectra of 1 mM *trans*-OMCA (purple) and *cis*-OMCA (red), and their pH.

the decrease of the band at 879 cm^{-1} and the increase of both 837 and 793 cm^{-1} bands with increasing UVR time. Furthermore, *trans*-OMCA presents a characteristic aromatic C-H in-plane bending vibration ($\beta\text{C-H}$) located at 996 cm^{-1} ,²⁸⁴ which decreases with the UVR.

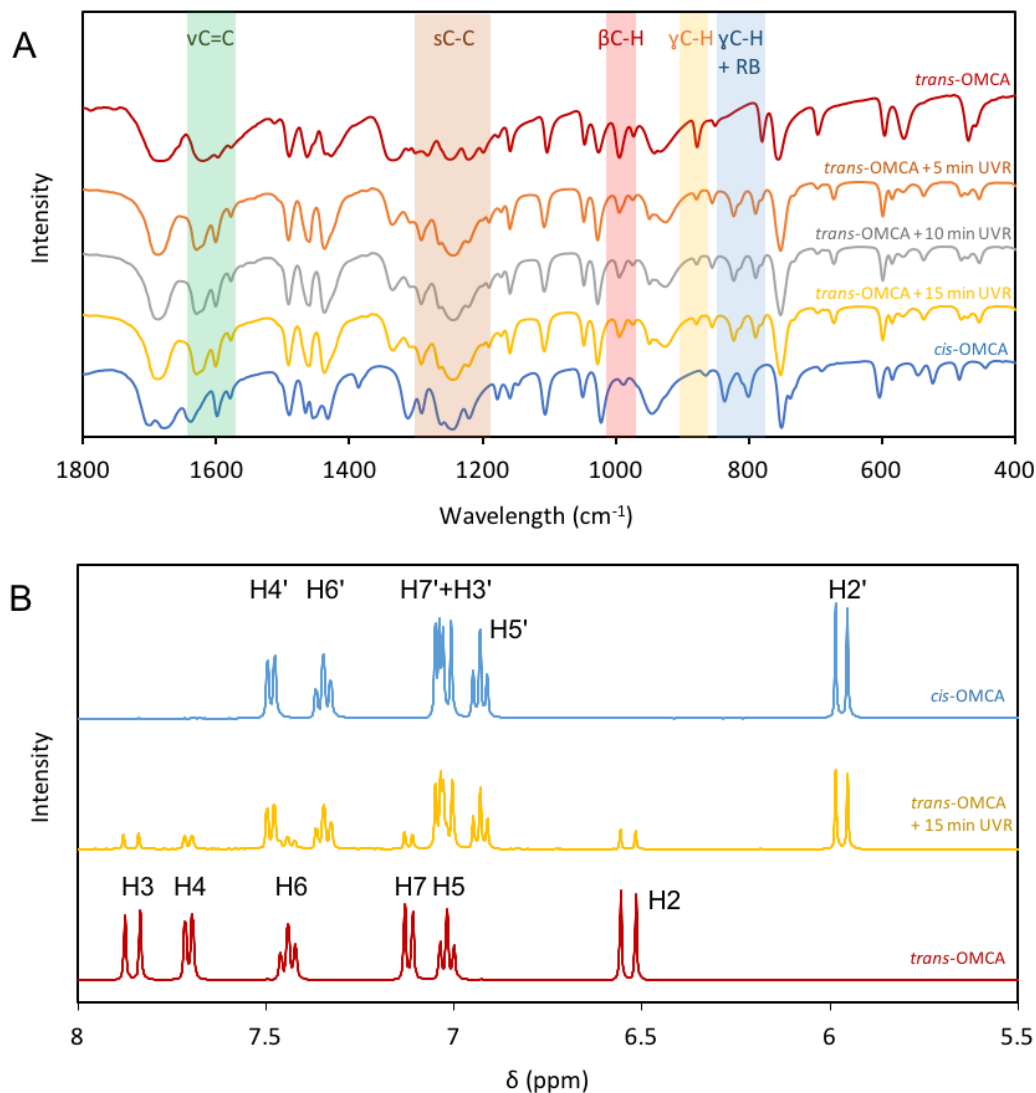


Fig. 4.9. (A) FTIR spectra of *cis*-OMCA and *trans*-OMCA after being irradiated with UV light for 0, 5, 10 or 15 min. (B) $^1\text{H-NMR}$ spectra of *cis*-OMCA and *trans*-OMCA before and after being irradiated for 15 min in DMSO-d_6 .

All those results are coherent with photoisomerization *trans* to *cis*. There are changes in other characteristic bands that are also consistent with photoisomerization. The samples' irradiation increases the two strong C-C stretching vibrations (sC-C) at 1291 and 1246 cm^{-1} associated to *cis*-OMCA,²⁸⁵ while the two less-intense bands at 1302 and 1202 cm^{-1} linked to *trans*-OMCA²⁸⁴ decrease in intensity. It is worth mentioning that all spectra present the characteristic bands of the acrylic C=C vibration ($\nu\text{C=C}$) at 1622 cm^{-1} for *trans*²⁸⁴ or at 1639 cm^{-1} for *cis*-OMCA.²⁸⁵ The existence of those $\nu\text{C=C}$ vibrations confirms that UVR does not induce photodimerization.²⁸⁶ The $^1\text{H-NMR}$

spectra of *trans* (before and after being irradiated for 15 min) and *cis*-OMCA in DMSO- d_6 were also collected (Fig. 4.9B) to complement the FTIR studies. The ^1H chemical shifts are summarized in Table 4.1 and assigned on the basis of theoretical estimations (performed with the commercial Chemdraw Ultra software) and literature values of related cinnamic compounds.²⁸⁷ The main difference between the two isomers is the peak positions of the acrylic hydrogens, which are located at 6.54 (H2) and 7.86 pm (H3) for *trans* and 5.97 (H2') and 7.02 pm (H3') for *cis*-OMCA. After 15 min of UVR, *trans*-OMCA spectrum presents peaks from both isomers, with the stronger ones associated to the *cis* form. This suggests that the photoisomerization has occurred but it was incomplete. An isomerization yield of 80% is calculated by integrating the signal intensities. This value is in agreement with the yield previously calculated from the UV-Vis data (*i.e.* 83 %).

Table 4.1. ^1H Chemical shifts (δ , ppm) of *trans* and *cis*-OMCA in DMSO- d_6

	<i>trans</i> -OMCA (δ , ppm)		<i>cis</i> -OMCA (δ , ppm)	
	<i>Exp.</i>	<i>Calculated</i>	<i>Exp.</i>	<i>Calculated</i>
H2	6.54	6.16	5.97	6.14
H3	7.86	8.04	7.02	7.62
H4	7.70	7.66	7.49	7.66
H5	7.02	7.02	6.93	7.02
H6	7.44	7.49	7.35	7.49
H7	7.11	7.07	7.04	7.10

Second, *trans* and *cis* isomers of cinnamic acid derivatives are known to present distinctive physical and chemical properties, such as pK_a ^{288,289} or freezing point.²⁹⁰ Those differences are due to the conjugation between the double bond and the aromatic ring, which is sterically hindered in the *cis* forms.²⁹¹ Furthermore, *trans*-OMCA presents stronger association with CTAB micelles than the *cis* isomer, most likely due to its geometry and higher hydrophobicity.²⁵¹ Therefore, the effect of UV light on the nanoparticle tuning has to be analyzed from two different points of views, *i.e.* changes on the interaction between surfactant and OMCA and changes on the growth solution conditions triggered by the isomerization.

Third, ascorbic acid presents two pK_a , one at 4.04²⁹² (*i.e.* transition from protonated form to ascorbate monoanion) and the other at 11.34²⁹³ (*i.e.* transition from ascorbate

monoanion to dianionic form). It is generally accepted that the reducing behaviour of ascorbic acid increases from protonated to dianionic form.^{294–296} Thus, its antioxidant strength increases with the pH, as stronger reducing species are produced in the medium. The pH of the growth solution was studied for different UV irradiation times before the addition of ascorbic acid and seeds. For AuNR growth solutions, the pH decreases from 3.06 to 3.01 after 15 min of irradiation (Table 4.2). The *trans* isomers of cinnamic acid family have higher pKa than that of the *cis* forms.^{288,289} Therefore, the photoisomerization produces more acidic species, which decrease the solution's pH. The higher acidity of *cis*-OMCA isomer was confirmed by comparing the pH of the solutions of the two isomers at 1 mM (Fig. 4.8B). The decrease of pH reduces ascorbic acid's reducing strength, slowing the growth of the rods. Smaller reducing capacity has been proved to be a key parameter to obtain larger aspect ratio AuNRs, since it allows the CTAB to direct the nanoparticle growth.²⁷⁸ In the case of AuNW growth solutions, the UV irradiation increases the pH from 10.90 to 11.03 (Table 4.2), which contributes to faster gold reduction and shorter aspect ratio worms. Even though it is not clear why the UV irradiation increases the pH in AuNW growth solutions, we hypothesize that may be the result of a complex combination of changes induced by the photoisomerization (e.g. isomer's solubility²⁵¹ and redox potential^{288,289}) and the solution's high pH (e.g. decrease on the stability of cinnamic acid derivatives²⁹⁷).

Table 4.2. Growth solution pH after UV irradiation.

<i>UV - Exposure (min)</i>	<i>pH in AuNW growth solution</i>	<i>Standard Dev.</i>	<i>pH in AuNR growth solution</i>	<i>Standard Dev.</i>
0	10.90	0.01	3.06	0.03
2.5	10.98	0.03	3.06	0.02
5	10.99	0.01	3.05	0.02
10	11.01	0.02	3.05	0.03
15	11.03	0.03	3.01	0.02

Fourth, another property that changes between isomers is their reduction and oxidation behaviour.²⁹⁸ Previously, we proved that OMCA contributes to reduce gold salts in the photoresponsive synthesis. Thus, a change on the OMCA reduction potential can affect the growth of the nanoparticles. The reduction behaviour of both OMCA isomers was studied under AuNR and AuNW growth conditions. Fig. 4.3C presents the Au³⁺ reduction kinetics in the AuNR growth solution (pH ≈ 3) by the action of both isomers. *cis*-OMCA presents faster reduction kinetics than *trans*. Therefore, photoisomerization from *trans* to *cis*-OMCA promotes faster gold reduction and contributes to obtain shorter rods. On the other side, the Au³⁺ reduction kinetics in the AuNW growth

solution (pH \approx 11) are very similar for both isomers (Fig. 4.6C) and no major differences are expected in the AuNW growth.

Table 4.3. Hydrodynamic diameter (D_H) of CTAB micelles after UV irradiation.

UV - Exposure (min)	D_H (nm) in AuNW growth solution	Standard Dev.	D_H (nm) in AuNR growth solution	Standard Dev.
0	1.47	0.02	0.94	0.03
1	1.50	0.05	0.94	0.04
2.5	1.47	0.04	0.97	0.09
5	1.48	0.02	0.94	0.05
10	1.47	0.02	0.93	0.04
15	1.49	0.03	0.89	0.09

Fifth, OMCA geometry affects the molecular packing of the CTAB/OMCA system and the final micelle morphology. Micelle shape transitions, such as wormlike to shorter rod micelles, have been obtained by irradiating a solution containing CTAB and *trans*-OMCA (*i.e.* 60 and 50 mM, respectively) with UV light.²⁵¹ Recently, it has been proved that CTAB micelle morphology affects the growth of AuNRs and their final aspect ratio.⁵⁹ Based on those observations, we studied if the UV light induces changes on CTAB micelle morphology, which could explain the nanoparticle tuning. Table 4.3 presents the hydrodynamic diameter of CTAB micelles in the growth solutions measured by dynamic light scattering (DLS). The micelle sizes are constant and independent of the irradiation time, with no morphological changes (*i.e.* size or shape) detectable by DLS. Nevertheless, AuNR and AuNW growth solutions present different micelle size, 0.9 and 1.5 nm, respectively. This size difference is likely due to the different pH. Aromatic counterions interact with CTAB micelles by inserting the aromatic ring in the surfactant aliphatic chain, while keeping the anionic part between the polar heads.²⁴⁸ This decreases the electrostatic repulsion between the CTAB polar heads, bringing the surfactant molecules closer and inducing the growth of the micelle. The OMCA pKa is 4.70.²⁹⁹ Thus, higher concentration of anionic OMCA is produced at pH \approx 11 than 3 (*i.e.* growth condition for AuNW and AuNR synthesis, respectively). Since, anionic OMCA can strongly screen the electrostatic repulsion between CTAB polar heads, AuNW growth solutions present larger micelles.

In conclusion, OMCA presents four key characteristics: it is photoresponsive; OMCA isomers have different redox behaviour; it affects the pH of the solution; and it has a structural role in forming the CTAB micelles. Table 4.4 summarizes the mechanistic observations described in the previous paragraphs. The increase of pH under AuNW growth conditions, promotes shorter aspect ratio worms. Both isomers present similar

reduction behaviour at those conditions, thus the nanoworm aspect ratio decreases upon UVR. On the other hand, UV light decreases the pH under AuNR growth conditions, promoting larger aspect ratio rods. However, the photoisomerization of *trans*-OMCA yields *cis* isomer, which presents stronger reduction behaviour at that pH and contributes to shorter rods. The two factors confront and promote opposing results. This may explain why AuNRs are tuned in a significantly narrower range than that for AuNWs, with L-LSPR band shifts of 49 and above 195 nm, respectively. Nevertheless, the changes on the pH seem to be more significant than the OMCA-reduction behaviour. This can be rationalized since the pH affects the redox potential of ascorbic acid, which is the main reducing reagent in the reaction. Finally, the micelle packing doesn't change by the photoisomerization and it doesn't play a role on the nanoparticle tuning.

Table 4.4. Parameters affecting the nanoparticle aspect ratio.

	<i>AuNRs</i>	<i>AuNWs</i>
pH	++	---
OMCA redox behaviour	-	=
Micelle shape	=	=
Overall effect	+	---

+ , - , = : Increasing, decreasing and no effect on nanoparticle aspect ratio.

4.3.4 In situ growth sensing of UV radiant exposure for erythema prevention

For sensing applications, UV exposure can be measured as received (*i.e.* without any mathematical treatment) or weighted using an erythemal response function.³⁰⁰ Since skin sensitivity to UV is wavelength-dependent, the erythemal response function has been developed in order to weight the wavelength effect and provide a single radiant exposure value, which can be directly correlated to the biological impact.^{301,302} Radiant exposure can be expressed in different units, such as energy per surface unit (J/m^2), standard erythemal dose (SED, erythemally weighted radiant exposure unit, equivalent to $100 \text{ J}/\text{m}^2$) or minimal erythemal dose (MED, minimal UVR dose to produce detectable erythema in a specific skin type).

Interestingly, just a small fraction of UV light irradiated by the sun reaches earth surface, *i.e.* UVC (100 – 280 nm) is completely adsorbed by atmospheric oxygen and ozone, while UVB (290 – 315 nm) is partially blocked and UVA (315 – 400 nm) weakly

attenuated.³⁰¹ Therefore, when the spectra of erythemal response function and sun irradiance at earth's surface are superimposed, the overlapped area is defined as the biologically active UV radiation (Fig. 4.10), which is a range of atmosphere-penetrating wavelengths that can induce erythema.^{301,302}

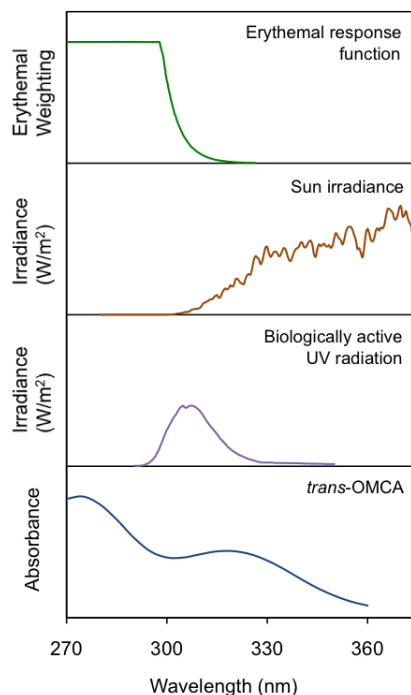


Fig. 4.10. Spectra of erythemal response function (green),³⁰¹ sun irradiance at earth's surface (orange),²⁷¹ biologically active UV radiation (purple)³⁰¹ and *trans*-OMCA absorbance (blue).

We propose using the UV-dependent growth of anisotropic nanoparticles in photoresponsive fluids as plasmonic nanosensor for UV exposure measurement. The CTAB / *trans*-OMCA system presents two main advantages: a) it absorbs in the range of both erythemal response function and biological active UV radiation (Fig. 4.10); and b) it can tune the morphology of AuNR and AuNW under UV irradiation. AuNRs were chosen for the sensing application over AuNWs, since their L-LSPR band is found in an easier wavelength range to measure (*i.e.* AuNW L-LSPR band can shift beyond 1000 nm). The growth solutions were irradiated with solar-simulated radiation for different periods of time before the synthesis of the rods. Fig. 4.11A plots the absorbance spectra of the rods grown in those solutions. The L-LSPR band shifts from 813 to 859 nm after 80 min of irradiation, which is in agreement with the previous results presented in this paper. Fig. 4.11B presents a calibration curve built by plotting the ratio between the two LSPR bands (A_L/A_T) with two horizontal axes, the non-erythemally weighted UV radiant exposure (J/m^2) and the erythemally weighted standard erythema dose (SED units). Finally, the sensor dynamic range can be divided

in MED ranges depending on skin type sensitivity. This allows predicting the potential skin damage of a specific radiant exposure. Thus, the system can be used not only as a sensor for UV exposure but also as prevention tool against erythema.

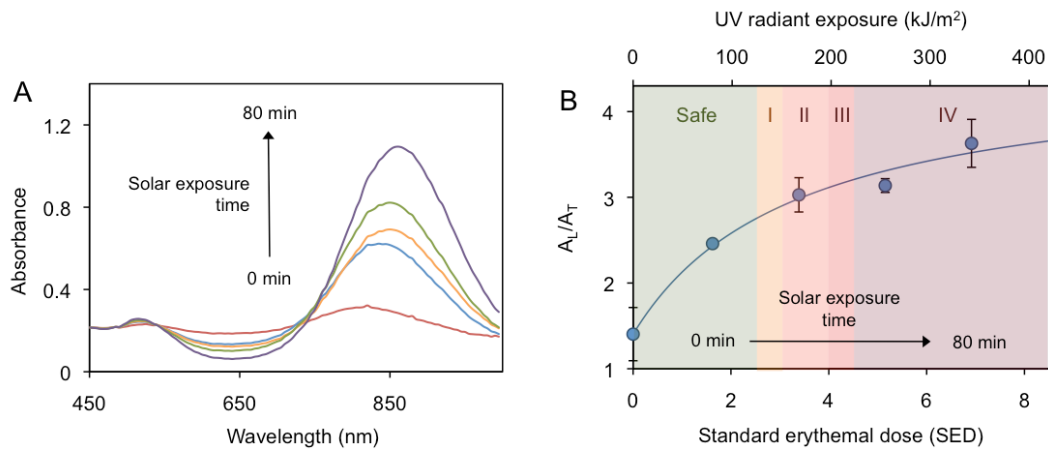


Fig. 4.11. (A) Absorbance spectra of AuNRs grown in the photoresponsive fluid after 0, 20, 40, 60 and 80 min of solar simulated irradiation. (B) Variation of the ratio between the AuNR longitudinal (A_L) and transversal (A_T) LSPR bands as a function of non-weighted UV radiant exposure and standard erythemal dose. The graph is divided in areas based on the exposure biological effect: harmless exposures (green) and erythema-causing exposures to skin type I (orange), type II (pink), type III (red) and type IV (dark red).

4.4 Conclusions

We have demonstrated that the physicochemical changes induced by UVR on a photoresponsive fluid affect the growth of anisotropic gold nanoparticles, *i.e.* nanorods and nanoworms. The as-prepared nanoparticles' dimensions, plasmon band position, and intensity are highly dependent on the UV irradiation. Interestingly, opposite phenomena are observed in the tuning of AuNR and AuNW. While the aspect ratio of the rods increases upon irradiating the photoresponsive fluid with UVR and the L-LSPR band red-shifts and increases in intensity, the same irradiation decreases the nanoworm dimensions and blue shifts its L-LSPR band. This distinctive behaviour depends on two factors: the pH change induced by the photoisomerization and the distinct reduction behaviour of OMCA isomers. The pH plays a major role on the redox behaviour of ascorbic acid, which controls the growth speed and final particle dimensions. Based on those findings, we have developed a plasmonic nanosensor for UV exposure. It is an *in situ growth sensor* that quantifies UV exposure when nanoparticles are synthesized. In this sensor, the UV exposure values can be correlated to the minimal UV-dose necessary to develop erythema. Thus, the growth of anisotropic nanoparticles in the photoresponsive fluid can be used not just as a plasmonic sensor but sunlight-disease prevention tool. Finally, this assay further reinforces the breakthrough strategy of combining both synthesis and sensing steps, while avoiding post-synthesis functionalization and enzyme-based nanoparticle growth, often used in other *in situ growth sensors*.

4.5 Annex

Table S4.1. p -values obtained by Welch t-test (unequal variances t-test), to study if the differences between AuNR aspect ratios are statistical significant.

<i>Time/Time</i>	<i>0 min</i>	<i>1 min</i>	<i>2.5 min</i>	<i>5 min</i>	<i>10 min</i>	<i>15 min</i>
0 min		0.0007				
1 min			0.5000 [*]			
2.5 min				0.0000		
5 min					0.0000	
10 min						0.0000
15 min						

^{*}AuNRs grown after 1 and 2.5 min of UV irradiation present the same aspect ratio.

Table S4.2. Cohen's d -values calculated to study the standardised differences between AuNR aspect ratios.

<i>Time/Time</i>	<i>0 min</i>	<i>1 min</i>	<i>2.5 min</i>	<i>5 min</i>	<i>10 min</i>	<i>15 min</i>
0 min		0.17				
1 min			0.00 [*]			
2.5 min				0.20		
5 min					0.20	
10 min						0.16
15 min						

^{*}AuNRs grown after 1 and 2.5 min of UV irradiation present the same aspect ratio.

Table S4.3. *p*-values obtained by Welch t-test (unequal variances t-test), to study if the differences between AuNW aspect ratios are statistical significant.

Time/Time	0 min	1 min	2.5 min	5 min	10 min	15 min
0 min		0.0000				
1 min			0.0000			
2.5 min				0.0004		
5 min					0.0000	
10 min						0.0000
15 min						

Table S4.4. Cohen's *d*-values calculated to study the standardised differences between AuNW aspect ratios.

Time/Time	0 min	1 min	2.5 min	5 min	10 min	15 min
0 min		1.44				
1 min			1.08			
2.5 min				1.18		
5 min					1.83	
10 min						1.00
15 min						

Chapter 5

An Enzyme-free Plasmonic Nanosensor with Inverse Sensitivity for Circulating Cell-free DNA Quantification

A plasmonic nanosensor (using gold nanorods) with inverse sensitivity is presented for circulating cell-free DNA quantification. The inverse sensitivity (*i.e.* the lower the analyte concentration, the higher the response intensity) is achieved by the unusual DNA concentration-dependent gold nanorod aggregation. This assay method can adjust the dynamic range by controlling the concentration of nanoparticles in solution.

5.1 Introduction

Currently, biopsy is the only method that can diagnose cancer with absolute certainty.³⁰³ This medical test involves the removal of tissue from the patient to determine the presence and extent of the abnormal cell growth. Several non-invasive alternatives have been developed, such as body fluid analysis.^{304–306} However, the lack of sensitivity and specificity of the most serum cancer biomarkers has prevented the use of body fluid analysis as definitive non-invasive sensing technique for cancer diagnostics.^{307,308} Nevertheless, the analysis of circulating cell-free DNA (cfDNA), *i.e.* extracellular and mostly double-stranded DNA found in nucleosomes^{309,310} and other complex species^{310–312} in blood, serum and plasma, has recently emerged as a promising new non-invasive liquid biopsy, which allows monitoring the patient's therapeutic response and disease progression.^{313–315} Even though a few commercial kits are available, providing fast and easy-to-use DNA quantification, most of them are not able to cover all the physiological cfDNA concentration range. Furthermore, the ranges of concentrations of the analysed samples are frequently close to the limit of detection (LOD) of those kits, providing small intensity responses, that leads to a low reliability. Therefore, new assay concepts are required for a robust quantification of cfDNA at low concentration range, especially around the LOD. In analytical chemistry, the low reliability for low analyte concentrations near the LOD is a common problem. Thus signal amplification strategies, *i.e.* enzymatic amplification,³¹⁶ labelling the analyte with antibody conjugates³¹⁷ or employing more sophisticate equipment,³¹⁸ have been largely developed. However, those options also increase the complexity of the design and resource investment.

In this chapter we propose an alternative analytical concept that overcomes the limitations of the commercial kits without involving complex designs. Particularly, we demonstrate a plasmonic nanosensor for cfDNA (or dsDNA) with inverse sensitivity, *i.e.* the lower the concentration of the analyte is, the higher the response intensity³¹⁹ (Fig. 5.1). This concept employs hexadecyltrimethylammonium bromide (CTAB) coated gold nanorods (AuNRs) and their electrostatic interactions with dsDNA. The inverse sensitivity is achieved by the unusual DNA concentration-dependent AuNR aggregation, which can be measured by UV-Vis spectroscopy. This sensor is fast (10 min), straightforward and easy-to-use (one-step, mixture of 3 solutions). To the best of our knowledge, this is the second paper reporting the concept of *inverse sensitivity*. This enables a higher reliability for low concentration analyte detection by creating inverse relationship between analyte concentration and signal output, which introduces

high signal-to-noise ratio (SNR) for low concentration detection. The first report of such concept was performed by L. Rodriguez-Lorenzo et al.,³¹⁹ where enzymatic catalysed gold nanoparticle formation provides the inverse sensitivity for protein biomarker detection. In our current work, we further reinforce the inverse sensitivity concept for cfDNA detection. Despite of using plasmonic nanoparticles' optical property as a signal output similarly, our method does not involve enzymes and is conceptually simpler without involving long experimental times and multi-step procedures. Furthermore, our concept allows for a tuneable dynamic range not existing in the first inverse sensitivity sensor.

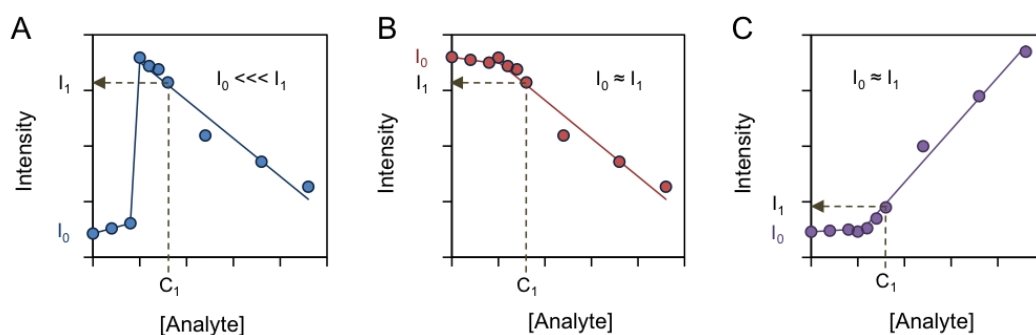


Fig. 5.1. Scheme of the response curves of sensors with (A) inverse sensitivity, (B) inversely proportional response and (C) directly proportional response. This scheme has been drawn for clarification purposes and it has not been made from real data.

5.2 Experimental section

5.2.1 Materials

In the series of experiments that are presented in this article, the following products were used as received. Hydrogen tetrachloroaurate trihydrate ($\text{HAuCl}_4 \cdot 3\text{H}_2\text{O}$), silver nitrate (AgNO_3 , 0.1 N), hydrogen chloride (HCl, 37% wt in water), L-ascorbic acid, sodium borohydride (NaBH_4 , 98%) were purchased from Sigma-Aldrich. Hexadecyltrimethylammonium bromide (CTAB, >98%) was purchased from Tokyo Chemical Industry. The oligos used in this study were purchased from Integrated DNA Technologies. Table 5.1 shows their sequences. For the ssDNAs hybridization, the sense and antisense strands were annealed at 95 °C for 5 min and cooled down for 4 h in 10 mM Tris-HCl buffer (pH 7.4), yielding their corresponding dsDNA. All the water employed in the experiments was obtained with a Mili-Q Integral 5 system.

Table 5.1. Oligonucleotides sequences

<i>Name</i>	<i>Sequence 5' to 3'</i>
180-bp ssDNA	CTGGCACTGCCCCGCCCCACCCCTGACTTGCCAGTGAGTCCCAGACAGGCTGGC GGGATGACACAGGTCAGTGTGACCACCTGAGTCACACGCCGTCAGTGTGAGGCC GTGAGTGCCCCAGGCACCGGGACCTGGGGACTGTGCTCTGCGGCCTGTGTACCC CACAGAACCGGTTCCCTTG
180-bp ssDNA- rev	CAAGGAACCGGTTCTGTGGGGTACACAGGCCGCAGAGCACAGTCCCCAGGTCCC GGTGCCTGGGGCACTCACGGCCTCACAGTGACGGCGTGTGACTCAGGTGGTCA AGTGACCTGTGTCATCCCAGCCTGTCTGGGACTCACTGGCAAGTCAGGGGT GGGGCGGGCAGTGCCAG

5.2.2 Characterization

Transmission electron microscopy (TEM) images were acquired with a Philips CM300 FEG TEM operating at 300 kV. The optical extinction spectra were recorded using a Synergy 2 Multi-Mode Reader spectrophotometer from BioTek Instruments, Inc. The fluorescence spectra were obtained by an InfiniteM200 from Tecan. The dynamic light scattering (DLS) measurements were performed with a DynaPro PlateReader-II from Wyatt Technology Corporation. The nanoparticle zeta potentials were recorded with a Zetasizer Nano Z from Malvern Instruments.

5.2.3 Synthesis of AuNRs

The AuNRs were synthesized via seed-mediated method. Briefly, Au seeds were obtained by adding at once 0.6 mL ice-cold NaBH_4 (10mM) into a 10 mL solution of CTAB (0.1M) and HAuCl_4 (0.25 mM) while vigorously stirred. The solution was stirred for 30 s and left undisturbed for 30 min.

Au NRs were synthesized by adding 250 μL of AgNO_3 (4 mM) into 5.0 mL solution of CTAB (0.1 M). The solution was kept undisturbed for 15 min, after which 5 mL of HAuCl_4 (1 mM) and 12 μL of HCl (37%) were added. After slow stirring, ascorbic acid (75 μL , 79 mM) was introduced. The mixture was vigorously stirred for 30 sec and 60 μL of the seed solution were added. Finally, the growth solution was vigorously stirred for 30 sec and left undisturbed for 12 h. The Au NRs were isolated by centrifugation twice at 7000 rpm for 15 min followed by removal of the supernatant. The final precipitate was diluted in 20 mL of water before used.

5.2.4 Colorimetric detection of dsDNA

The assay was performed after preparing dsDNA solutions with different concentrations in 8 mM Tris-HCl buffer (pH 7.4). 25 μL of those solutions were added into 75 μL of as-prepared Au NRs. The final concentrations of dsDNA ranged from 0 to 100 nM. The mixtures were incubated at room temperature for 10 min and the UV-Vis spectra were recorded afterwards.

5.2.5 Fluorescence assays

dsDNA was incubated with thiazole orange (TO) in a proportion of 1:40 in Tris 10 mM buffer at room temperature for 30 min. Saturation of dsDNA with TO is achieved at ratio of 1 dye to 2 base pairs.³²⁰ Because we wanted to make sure that all TO was bound to dsDNA, a ratio of 1 dsDNA to 40 TO was selected (1 dye to 4.5 base pairs). The fluorescence of several dilutions, ranging from 0 to 50 nM, was measured in the absence and presence of AuNRs ($\text{OD}_{890} = 0.48$).

5.3 Results and discussion

5.3.1 Inverse response

The AuNRs used in this work were synthesized by seed-mediated method with CTAB as a surfactant,⁵⁷ which results in a positively charged gold surface. When negatively charged molecules are mixed with AuNRs, the rods aggregate.³²¹ Several reports have published apparently contradictory results, *i.e.* a few groups reporting the AuNR aggregation by dsDNA^{322,323} while others found that dsDNA can protect them against aggregation.^{324,325} We discovered that the result of the interaction between dsDNA and AuNR is concentration dependent, and therefore both induction of AuNR aggregation and protection against aggregation occur depending on the dsDNA and AuNR concentrations. Both phenomena can be followed by the shift of the longitudinal localised surface plasmon resonance band (L-LSPR) as a consequence of the plasmon coupling between contiguous rods.

Fig. 5.2A shows the UV-Vis spectra of AuNRs (optical density at 890 nm, OD₈₉₀ of 0.48) with aspect ratio (AR) of 4.9 mixed with dsDNA (in 8 mM Tris buffer) at different concentrations. The dsDNA molecules were 180 base-pair long, which is the typical length of the cfDNA fragments originated from apoptotic cells.³²⁶ The Tris buffer is the most common buffer used by the commercial DNA extraction kits.³²⁷ Since cfDNA is commonly adsorbed on other species in biological samples (*e.g.* proteins^{309,310} and lipid membranes³¹⁰⁻³¹²), its extraction is an essential step prior to the analysis using any commercial quantification kit,³²⁸ and our plasmonic sensing method. Initially, the dsDNA induces the assembly of the rods, red-shifting the L-LSPR band from 890 to 995 nm at 2.5 nM. However, further addition of dsDNA promotes the opposite phenomenon, *i.e.* disaggregation of the rods. The L-LSPR band blue-shifts back, up to 895 nm at 50 nM dsDNA. The aggregation and disaggregation is quantified using the absorbance ratio at 510 and 890 nm wavelengths (A_{510}/A_{890}) for different dsDNA concentrations in Fig. 5.2B. The limit of detection (LOD) is 2.5 nM, which is calculated as the lowest analyte concentration that is detected in the inverse-sensitivity regime, and the dynamic range is from 2.5 to 50 nM. The response curve of the sensor has been divided in two concentration regimes, *i.e.* below (green) and above (blue) the LOD, respectively. It is noteworthy that the below LOD regime presents normal sensitivity with increasing signal with the analyte concentration. This lower concentration regime is so narrow (5 % of the concentration of the full response curve) that can be neglected, yielding an inverse sensitivity sensor closer to the idealistic

performance, *i.e.* zero response below the LOD. Additionally, the sample concentration within the higher concentration regime (*i.e.* the one with inverse sensitivity response) can be confirmed by diluting the sample for a second test. An increase of A_{510}/A_{890} is expected if the sample is within this higher concentration regime. Otherwise a decrease of A_{510}/A_{890} would be observed if it is in the lower concentration regime. Interestingly, the SNR at the LOD is highly enhanced by the inverse sensitivity, *e.g.* SNR at 2.5 nM is 63, in comparison to the conventional sensors, whose SNR at the LOD is 3 by definition.³²⁹

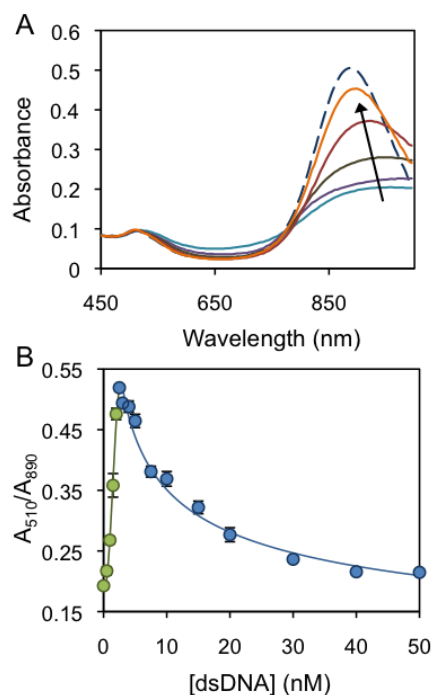


Fig. 5.2. Characterization of AuNRs ($OD_{890} = 0.48$), mixed with different amounts of dsDNA (180bp) in 8 mM Tris buffer. (A) UV-Vis spectra at 0 nM (dashed line), 2, 5, 10, 20 and 40 nM DNA (solid lines). (B) Absorbance ratio intensities at 510 and 890 nm as the function of DNA concentration. The lower and higher concentration regimes are highlighted in green and blue, respectively.

Transmission electron microscopy (TEM) studies were performed to characterise the AuNRs assembly and disassembly at the nanoscale. Fig. 5.3A reveals well monodispersed AuNRs in the absence of dsDNA. After the addition of dsDNA of as low as 2 nM, the rods are assembled, yielding several micrometer sized aggregates (Fig. 5.3B). Upon further addition of dsDNA, *e.g.* 10 nM, initiates the disaggregation (Fig. 5.3C). At dsDNA concentration of 20 nM, the original AuNR dispersity is almost recovered and only small aggregates are present in the sample (Fig. 5.3D). These results are confirmed by dynamic light scattering (DLS), which shows a dramatic increase of the AuNR hydrodynamic radius from 8 to 110 nm, after the initial addition of dsDNA, and its subsequent decrease back to 14 nm at higher dsDNA concentration (Fig. 5.3E).

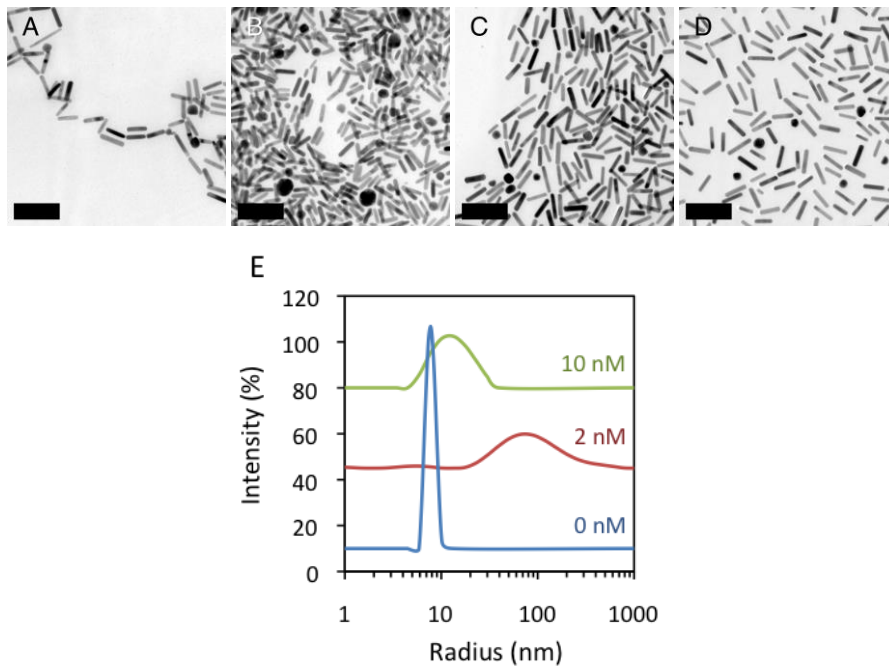


Fig. 5.3. Characterization of AuNR aggregation and disaggregation induced by dsDNA. TEM images at dsDNA concentrations of (A) 0, (B) 2, (C) 10 and (D) 20 nM. All scale bars are 50 nm. (E) Measures of AuNR hydrodynamic radius at 0, 2 and 10 nM dsDNA by DLS. The radius distributions have been offset vertically for clarity.

5.3.2 Mechanism behind the inverse sensitivity

To gain a more complete understanding of the mechanism involved in the concentration-dependent interaction of the dsDNA with the AuNRs, the nanoparticle zeta potential was measured after the addition of different amounts of dsDNA. Fig. 5.4 shows an initial decrease in the AuNR zeta potential with the increase in the dsDNA concentration. The rapid decrease can be attributed to the screening of the CTAB

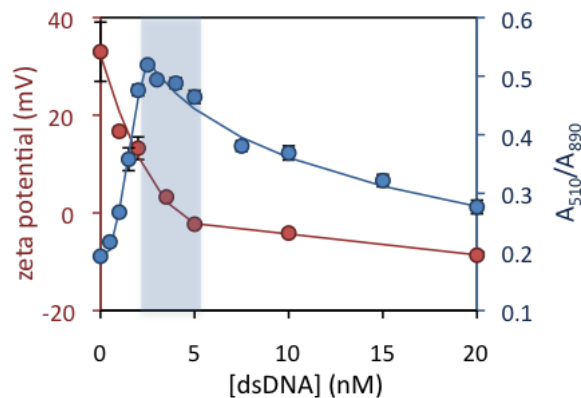


Fig. 5.4. Comparison between the effect of dsDNA concentration on the AuNR zeta potential (red) and the A_{510}/A_{890} (blue). The region of concentrations with higher AuNR aggregation is highlighted in pale blue.

positive charges by the dsDNA phosphate groups. Once the AuNR net charge has been neutralized, further additions of dsDNA induce a charge reversal and a slow negative increase of the nanoparticle electric potential. Zeta potential is one of the key parameters defining the repulsive forces among nanoparticles and colloidal stability.³³⁰ Therefore, its fast neutralization and subsequent negative increase resulted in the AuNR initial aggregation and the later disaggregation. This result is consistent with the zeta potential and the A_{510}/A_{890} profiles, which show the range of dsDNA concentrations with zeta potential closer to zero is the range with higher aggregation. To complement the concentration dependent charge density observations from the zeta potential experiments, we designed an experiment to study the relative positions between AuNRs and dsDNA. In this experiment, the dsDNA molecules were saturated by TO, *i.e.* an intercalation dye that increases its fluorescence quantum yield 18900-fold upon binding to DNA,³³¹ at molar ratio of 1:40 (Fig. 5.5). The fluorescence of the resulting dsDNA-TO₄₀ can be quenched by AuNRs when they are in close proximity through nanoparticle surface energy transfer mechanism.³³² Therefore, measuring the fluorescent emission of the dsDNA-TO₄₀ can provide information about their relative position to the AuNR surface. Fig. 5.6A shows the emission of dsDNA-TO₄₀ solutions (0-50 nM), same concentration range as used in the nanorod aggregation study, in the absence and presence of AuNRs (OD₈₉₀ = 0.48). In the absence of AuNRs, the fluorescence intensity at 535 nm (maximum emission wavelength) is linearly proportional to the concentration of the dsDNA-TO₄₀ complex as expected (Fig. 5.6B). However, if the measured solution contains AuNRs, the fluorescence is almost totally quenched. Fig. 5.6C compares the fluorescence emission of dsDNA-TO₄₀ in the presence of AuNRs and the AuNR aggregation profile measured with DNA without the intercalation dye. In the range of concentrations from 0 to 20 nM, where the rods are

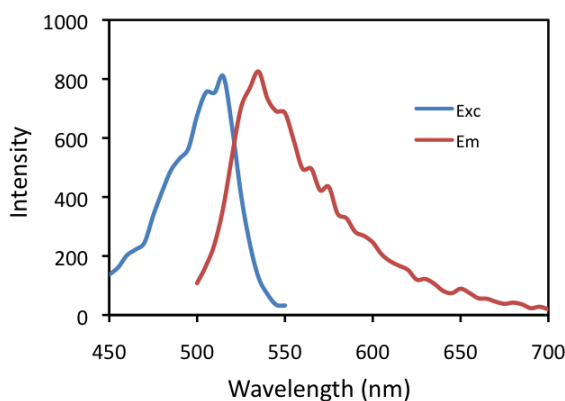


Fig. 5.5. Excitation and emission spectra of dsDNA-TO₄₀ (5 nM). Excitation wavelength: 450 nM. Emission wavelength: 600 nm.

initially aggregated and later start disaggregating, all the fluorescence is quenched. The fluorescence intensity begins increasing after most part of the AuNRs have been disaggregated, e.g. dsDNA-TO₄₀ concentrations higher than 20 nM.

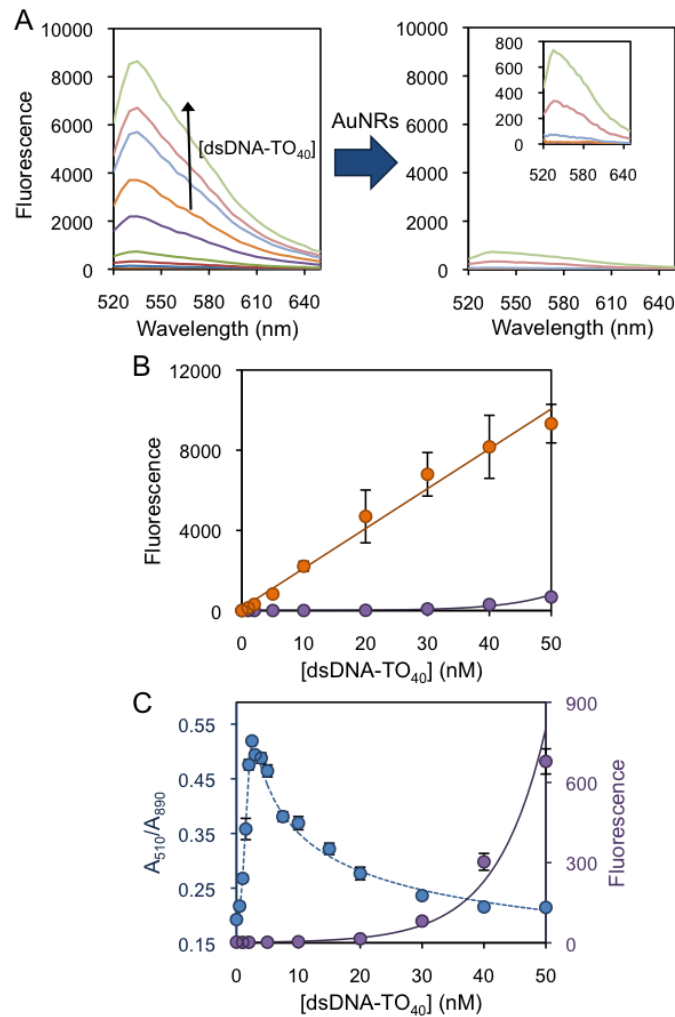


Fig. 5.6. (A) Fluorescence emission of dsDNA-TO₄₀ solutions in the absence and presence of AuNRs ($OD_{890} = 0.48$), respectively. (B) Emission intensities of different dsDNA-TO₄₀ solutions at emission wavelength of 535 nm in the absence (orange) and presence (purple) of AuNRs. (C) Comparison between the fluorescence emission of dsDNA-TO₄₀ in the presence of AuNR and their aggregation profile. All measures were done with an excitation wavelength of 490 nm.

Based on the collective observations, we propose a mechanism for the DNA concentration-dependent AuNR aggregation and re-dispersion. Initially, the dsDNA molecules are adsorbed on the AuNR surface by electrostatic interactions, leading to total dsDNA-TO₄₀ fluorescence quenching. At the lower DNA concentration regime (<2.5 nM), the electrostatic interactions between the dsDNA molecules and the AuNRs drive the initial aggregation, due to the decrease on the nanoparticle positive charge, and this process continues until the AuNRs have zero net charge. When DNA concentration increases further, more nucleic acids continue to adsorb on the AuNR surface, as evidenced by the nearly total quenching of the dsDNA-TO₄₀ emission up to

~20 nM, as well as the pickup of the nanoparticle negative charge. The slow negative charge increase is accountable for the disaggregation process at higher DNA concentration regime (>2.5 nM). At concentrations above 20 nM, we hypothesize that the AuNRs are mostly covered and the excess dsDNA chains have little access to the CTAB gold surface and thus the fluorescence emission starts to pick up. Those free-DNA molecules have little to non-effect on the nanoparticle disaggregation, based on the small A_{510}/A_{890} changes observed at concentrations higher than 20 nM. This unique DNA concentration dependent tuning of AuNR surface charge is the key of the inverse sensitivity.

5.3.3 Tuning the dynamic range

One major issue for detecting cfDNA and other nuclear acids in clinical samples is that the concentrations vary widely in those samples. To take full advantage of the inverse sensitivity method described here, it is important to tune the dynamic ranges of the detection so that the highest inverse sensitive area matches the cfDNA concentration in the samples. Toward this goal, we have changed the AuNR concentration in solution in order to adjust the dynamic range of the sensor and its section with higher SNR to different common ranges previously published in the literature.

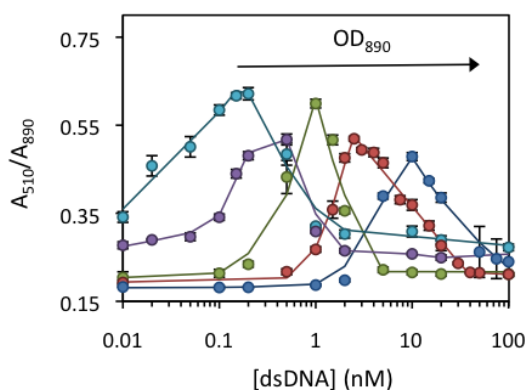


Fig. 5.7. Effect of the dsDNA concentration on the A_{510}/A_{890} of five AuNR solutions. AuNR OD_{890} of 0.05 (turquoise), 0.08 (purple), 0.22 (green), 0.48 (red) and 0.92 (blue).

Fig. 5.7 depicts the aggregation profile of AuNR solutions at five different concentrations, *i.e.* OD_{890} of 0.92, 0.48, 0.22, 0.08 and 0.05. The LOD was found to increase with the AuNR concentration, *e.g.* 10 nM for the most concentrated solution, relative to 0.2 nM for the most diluted one. The AuNR concentration also affects the dynamic range, increasing it and shifting it, *e.g.* from 0.2 to 2 nM and 10 to 100 nM for the AuNR solutions with OD_{890} of 0.05 and 0.92, respectively. The combination of the

five AuNR solutions yields a sensor that is sensitive enough to monitor the cfDNA levels associated with a wide range of cancer types (Table 5.2).

When the AuNR solution is added into the sample, the DNA concentration is diluted. Thus, the concentration values have to be corrected depending on the AuNR solution (75 μ l) and the initial the sample volume. In Table 5.2 we present the results for an original sample volume of 25 μ l.

Table 5.2. Dynamic ranges of different AuNR solutions and their equivalence for an original 25 μ L sample. The dynamic ranges from an original 25 μ L sample are compared with several reference values from cancer patients.

[AuNR] (OD)	Concentrations range in the sensor solution		Concentrations range in 25 μ L Sample		Reference Cancer Patient Values		
	Min [dsDNA] ng/ml (nM)	Max [dsDNA] ng/ml (nM)	Min [dsDNA] ng/ml	Max [dsDNA] ng/ml	Cancer Type	Value ng/ml	Sample
0.93	1111.3 (10)	11112.6 (100)	4445.1	44450.6	-	-	-
0.48	277.8 (2.5)	5556.3 (50)	1111.3	22225.3	Colorectal (stage I – II) ³³³	1630 \pm 430	Serum
					Colorectal (stage III – IV) ³³³	1730 \pm 450	Serum
0.22	111.1 (1)	555.6 (5)	444.5	2222.5	Melanoma (Metastasis) ³³⁴	1056* (411 – 2021)	Serum
					Colorectal ³³⁵	868* (22 – 3922)	Serum
					Lymphoma ³³⁶	899* (171 – 2660)	Plasma
					Brest (stage III) ³³⁷	589 \pm 87	Serum
					Brest (stage IV) ³³⁷	776 \pm 271	Serum
0.08	55.6 (0.5)	222.3 (2)	222.3	889	Stomach ³³⁶	593* (232 – 1111)	Plasma
					Lung ³³⁸	318**	Plasma
					Gastrointestinal ³³⁹	412 \pm 63	Serum
0.05	22.2 (0.2)	222.3 (2)	88.9	889	Gastrointestinal (Benign) ³³⁹	118 \pm 14	Serum
					Melanoma (Metastasis) ³³⁴	259* (83 – 604)	Plasma
					Mix ³⁴⁰	180 \pm 38	Serum

* Median

** Standard deviations or ranges are not provided.

5.4 Conclusions

In summary, we have developed a plasmonic nanosensor with inverse sensitivity, exploiting the unique DNA concentration-dependent AuNR aggregation/re-dispersion profile for cfDNA detection. A mechanism based on the change of the AuNR electric potential by the adsorption of dsDNA molecules at two regimes of lower and higher concentrations has been proposed to account for the inverse response of the sensor. The LOD and the dynamic range of this method can be adjusted by controlling the AuNR concentration in solution, allowing tunable sensor response curve and covering a wide range of cfDNA concentrations linked to cancer diagnosis and prognosis. The lowest LOD reached by this method is 0.2 nM with an overall dynamic range of 0.2 to 100 nM. Notably, this is the second report of inverse sensitivity, relative to a previous one involving enzymatic reaction. The assay is conceptually simple, fast, easy-to-use and compatible with cfDNA extraction medium. This study further reinforces the breakthrough strategy of enhancing the reliability of low concentration detection, by literally introducing high SNR, which is often failed in the normal sensitivity sensing and signal amplification strategies.

Chapter 6

Plasmonic Multi-logic Gate Platform Based on Sequence-specific Binding of Transcription Factors and Gold Nanorods

A hybrid system made of gold nanorods (AuNRs) and double-stranded DNA (dsDNA) is used to build a versatile multi-logic gate platform, capable of performing six different logic operations. The sequence-specific binding of transcription factors to the DNA drives the optical response of the design.

6.1 Introduction

One of the most promising applications of nanotechnology is building molecular-scale logic gates, capable of performing logic operations on external inputs.^{341,342} Those new logic gates are candidates for the new computing revolution and miniaturize information technology at nanoscale.³⁴³ To date, most molecular logic gate designs are based on fluorescence signals^{344–346} and chemically demanding modifications of nanomaterials³⁴⁷ and/or biomolecules,^{346,348–350} which increase design complexity and resource investment. Recently, gold nanoparticles (AuNPs) have been used as building blocks for colorimetric logic gates^{180,351–354} due to their high extinction coefficients and interparticle-distance dependent optical properties,¹¹² which can be easily monitored by UV-visible spectroscopy.

Even though the existing AuNP-based logic gate designs present promising results, they have several drawbacks, such as complex surface modifications,^{351,352} multiple separation and purification steps,³⁵² lack of versatility to build several logic gates^{180,353} and/or use of strong toxic ligands.^{180,353,354} Nowadays, great efforts are made in bioinspired materials research to mimic nature's high dynamic control over the nanomaterial assembly, with excellent spatial and temporal resolution upon a biological input.³⁵⁵ Following this strategy, several logic gate designs have recently been published, exploiting biochemical events, such as antibody recognition,³⁵⁰ DNA hybridization,^{349,356} DNA assembly,³⁵⁷ catalytic reactions by DNAzymes³⁵⁸ or peptides interactions.³⁵⁹

The logic system that we present in this chapter is able to go a step further. To the best of our knowledge, this is the first design to mimic the gene regulation performed by transcription factors as a biochemical event for the logic response. Furthermore, this design overcomes the lack of versatility of most designs and can perform six different logic gates, while no complex surface modification is required. Multi-logic gate platforms capable of performing six logic operations are very rare and just few have been published.^{357,359} The mechanism of this multi-logic gate platform relies on the binding of estrogen receptors (ERs) to dsDNA adsorbed on gold nanorods (Fig. 6.1). ERs are a group of transcription factors activated by estrogen³⁶⁰ (*i.e.* steroid hormone that regulates several functions including the development of reproductive system and maintenance of bone structure). ER's action involves binding to specific DNA sequences, called estrogen receptor elements (EREs), that triggers the estrogen biological response.³⁶¹ The dsDNA used in this work is 35 base-pair long and contains

the ERE consensus sequence (GGTCAnnnTGACC, where n are spacer nucleotides), which provides binding specificity for ERs (*i.e.* ER α and ER β).

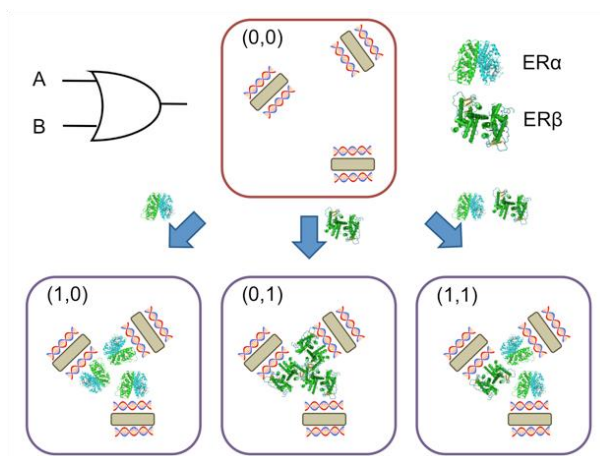


Fig. 6.1. Schematic illustration of one of the logic gates, *i.e.* OR, performed by the multi-logic gate design. OR logic gate is built by combining dsDNA-AuNRs and ERs, exploiting sequence-specific interactions between ERs and dsDNA.

6.2 Experimental section

6.2.1 Materials

In the following products were used as received. Hydrogen tetrachloroaurate trihydrate ($\text{HAuCl}_4 \cdot 3\text{H}_2\text{O}$), silver nitrate (AgNO_3 , 0.1 N), hydrogen chloride (HCl, 37% wt in water), L-ascorbic acid, sodium borohydride (NaBH_4 , 98%), lysozyme from chicken egg white (90 %) and the oligos containing the wild-type ERE consensus sequence (wtERE, 5'-AGTAAGCTCCAGGTCATTATGACCTGGAGCTTACT-3') were purchased from Sigma-Aldrich. Hexadecyltrimethylammonium bromide (CTAB, >98%) was purchased from Tokyo Chemical Industry. Human recombinant estrogen receptor α and β (ER α and ER β) were purchased from Life Technologies, ThermoFisher Scientific. To form dsDNA, the sense and antisense strands were annealed at 95 °C for 5 min and cooled down for 3 h in 10 mM Tris-HCl buffer (pH 7.0). All the water employed in the experiments was obtained with a Mili-Q Integral 5 system.

6.2.2 Characterization

Transmission electron microscopy (TEM) images were acquired with a FEI Titan TEM operating at 200 kV. The optical extinction spectra were recorded using a Spectramax M2/M2^e UV/Vis/NIR spectrophotometer. The dynamic light scattering (DLS) and zeta potential measurements were recorded with a Zetasizer Nano Z from Malvern Instruments. pH was measured with an 827 pH lab from Metrohm.

6.2.3 Synthesis of AuNRs

The AuNRs were synthesized via seed-mediated method. Briefly, *Au seeds* were obtained by adding at once 0.6 mL ice-cold NaBH_4 (10mM) into a 10 mL solution of CTAB (0.1 M) and HAuCl_4 (0.25 mM) while vigorously stirred. The solution was stirred for 30 s and left undisturbed for 60 min.

AuNRs were synthesized by adding 250 μL of AgNO_3 (4 mM) into 5.0 mL solution of CTAB (0.1 M). The solution was kept undisturbed for 15 min, after which 5 mL of HAuCl_4 (1 mM) and 12 μL of HCl (37%) were added. After slow stirring, ascorbic acid (75 μL , 79 mM) was introduced. The mixture was vigorously stirred for 30 s and 60 μL of the seed solution were added. Finally, the growth solution was vigorously stirred for

30 s and left undisturbed for 12 h. The AuNRs were isolated by centrifugation twice at 8500 rpm for 15 min followed by removal of the supernatant.

6.2.4 Determination of metallic Au concentration

The concentration of metallic Au (Au^0) in solution was determined by the Edgar *et al.* method.³⁶² Briefly, a calibration curve at 400 nm was built by well-aging different CTAB stabilized AuNP solutions of known Au^0 concentration for a month. This ensured that the reduction of gold salts was fully reached and no size effect would interfere with the measures. Metallic gold presents inter-band transitions in the range from 350 to 450 nm.^{363,364} Therefore, the absorbance within this range is relatively independent from the shape and it has been widely used in the past to quantify metallic gold.^{217,232,362} A comparison between the results of this method and ICP-MS was performed by Edgar *et al.*,³⁶² presenting discrepancies below 20%.

6.2.5 AuNRs aggregation by dsDNA

dsDNA solutions with different concentrations were prepared in 10 mM Tris-HCL buffer (pH 7.0). 1 μL of those solutions was added into a solution made of 25 μL of AuNR (final Au^0 concentration of 257 μM) and 74 μL of DI water. The final dsDNA concentration in solution ranged from 0 to 100 nM. The mixtures were incubated at room temperature for 10 min and the UV-Visible spectra were registered.

6.2.6 Protein-dsDNA binding assays

Binding assay at low concentration regime. The binding assay was performed by incubating 25 μL of AuNRs (final Au^0 concentration of 257 μM) with 1 μL of dsDNA (final concentration 10 nM) in 70 μL of DI water at room temperature for 10 min. The resulting solutions were mixed with 4 μL of different diluted solutions of ER α , ER β or lysozyme in 12.5 mM Tris-HCl buffer (pH 8.0, 9.0 and 8.0 respectively). The final protein concentrations ranged from 0 to 35 nM for ER α and lysozyme and from 0 to 70 nM for ER β . The mixtures were incubated for another 40 min at room temperature before their characterization.

Binding assay at high concentration regime. The binding assay was performed by incubating 25 μL of AuNRs (final Au^0 concentration of 257 μM) with 1 μL of dsDNA (final concentration 75 nM) in 67.5 μL of DI water at room temperature for 10 min. The

resulting solutions were mixed with 6.5 μL of different concentrated solutions of ER α or lysozyme in 50 mM Tris-HCl buffer (pH 8.0). The final concentrations of proteins ranged from 0 to 262.5 nM. The mixtures were incubated for another 40 min at room temperature before their characterization.

6.3 Results and discussion

6.3.1 Combination of AuNRs and dsDNA

AuNRs with an aspect ratio of 4.1 were synthesized by seed-mediated method (Fig. 6.2).⁵⁹ Hexadecyltrimethylammonium bromide was used as surfactant, which provides positive charges to the surface of nanorods. We recently proved that when positively charged AuNRs are mixed with negatively charge dsDNA, the nucleic acid molecules are adsorbed on the nanoparticle surface (dsDNA-AuNR), changing the electric potential of the particles.²⁰¹ The variation of the surface charge of the rods triggers the nanoparticle aggregation at lower dsDNA concentrations and disaggregation at higher concentrations.

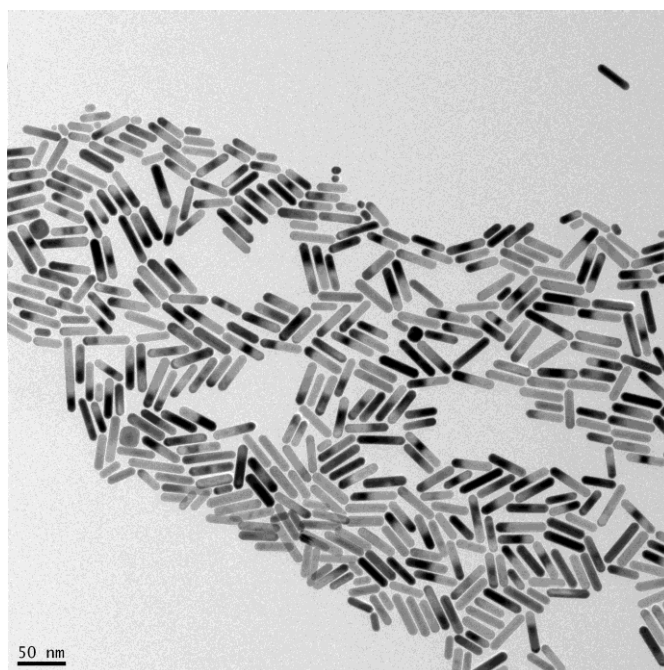


Fig. 6.2. TEM image of AuNRs used in the protein-DNA binding assays. AuNR dimensions are $42.6 (\pm 10.0) \times 10.4 (\pm 1.2)$ nm with aspect ratio of $4.1 (\pm 0.8)$.

Fig. 6.3A presents the red shift of the AuNR longitudinal localised surface plasmon resonance (L-LSPR) band by the addition of dsDNA from 0 to 20 nM (Au^0 concentration of $257 \mu\text{M}$). Interestingly, further increase of dsDNA, *i.e.* from 20 to 100 nM, blue shifts back the L-LSPR band (Fig. 6.3B). In a plot of the absorbance ratio at the two plasmon band maxima wavelengths (A_{510}/A_{885}) versus dsDNA concentration (Fig. 6.3C), the lower (blue) and the higher (red) concentration regimes are clearly observed. Dynamic light scattering characterization (DLS, Fig. 6.4) confirmed the initial rod aggregation and later disaggregation, which are account for the increase and

decrease of A_{510}/A_{885} values in Fig. 6.3C, respectively. DLS shows the increase of the rod hydrodynamic diameter from 55 nm up to 3803 nm after the addition of 20 nM dsDNA. The initial dispersity, measured by the initial particle size, is almost fully recovered at 100 nM dsDNA, where the hydrodynamic diameter decreases to 64 nm. The change of the AuNR's surface charge as driving force behind the two-concentration regime behaviour²⁰¹ is further verified by a zeta potential analysis (Fig. 6.4). AuNRs are initially positively charged (30.4 mV). The addition of dsDNA starts neutralizing the surface charge by electrostatic screening, decreasing the electrostatic repulsion among the particles. This induces the nanorod aggregation, which reaches its maximum when the surface charge is neutralized at around 20 nM dsDNA. Further additions of dsDNA induce a charge reversal and increase of the negative charge, which restores part of the electrostatic repulsion among the particles and disassembles them, reaching a zeta potential of -22.6 mV at 100 nM dsDNA.

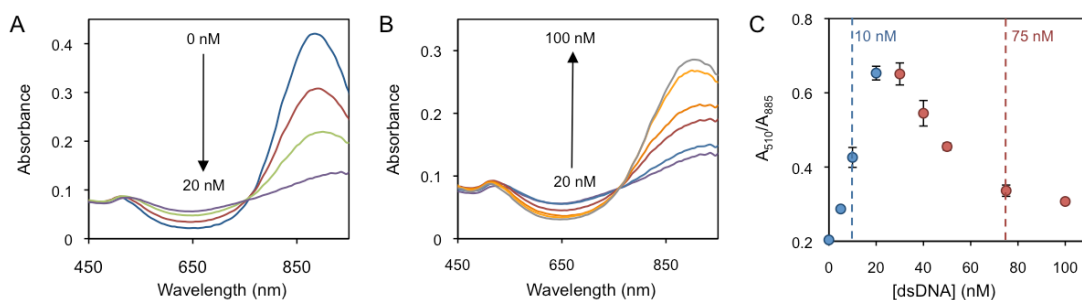


Fig. 6.3. Characterization of AuNRs mixed with different amounts of dsDNA. (A) UV-Vis spectra of the AuNRs in the presence of 0, 5, 10 and 20 nM DNA. (B) UV-Vis spectra in the presence of 30, 40, 50, 75 and 100 nM DNA. (C) Absorbance intensity ratio at 510 and 885 nm as function of DNA concentration. The lower and higher concentration regimes are highlighted in blue and red, respectively. 10 nM at the lower concentration regime and 75 nM at the higher concentration regime are indicated because these two concentrations are used in the protein-DNA binding characterization experiments.

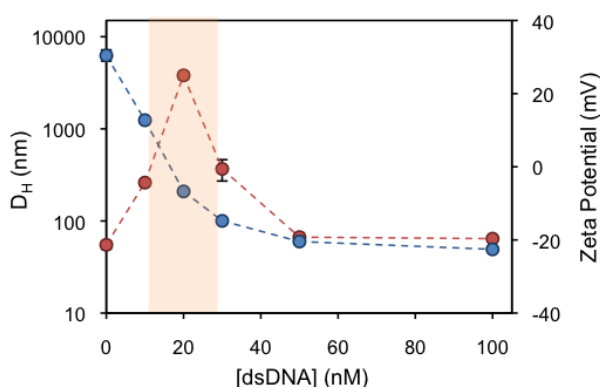


Fig. 6.4. (Red) hydrodynamic diameter (D_H) measured by DLS and (blue) zeta potential of AuNRs as a function of dsDNA concentration. The area with higher AuNR aggregation is highlighted in pale-orange.

6.3.2 Characterization of protein-dsDNA binding

Due to the different electrokinetic behaviour of dsDNA-AuNR at lower and higher dsDNA concentration regimes, the binding of ERs to dsDNA-AuNR was studied at two DNA concentrations of 10 nM (lower concentration regime) and 75 nM (higher concentration regime). Two human ER subtypes (*i.e.* ER α and ER β) were used to prove the effect of protein-DNA interactions on the aggregation of AuNRs. ER α and ER β have an isoelectric point (pI) of 8.3 and 8.8, respectively,³⁶⁵ and they are sold and stored in Tris 50 mM buffer (pH 8 and 9, respectively). When Tris 50 mM (pH 8) without ERs is added to the dsDNA-AuNR solutions, the nanoparticles slightly aggregate over time (Fig. 6.5). After an incubation of 40 min, the absorbance ratios are mostly stable, indicating that no further aggregation significantly occurs due to the buffer. Thus, incubation times of 40 min are chosen for all protein-binding experiments to equalize the buffer effects. Fig. 6.6A and 6B present increasing A_{510}/A_{885} (increased aggregation) upon ER α binding at 10 and 75 nM dsDNA, respectively. Both figures show that the transcription factor binds to the ERE-containing dsDNA with a stoichiometry of 2 to 1, *i.e.* A_{510}/A_{885} reaches saturation at 2:1 of ER:dsDNA concentration ratio. This is in agreement with previously published literature that reports ER α binding to ERE as a dimer.¹⁵⁶ We hypothesize that the aggregation is driven by the interprotein interactions. At pH close to the protein's pI (solutions pH ~ 8.0), the van der Waals and dipole-dipole attractive forces dominate over the charge-charge electrostatic repulsion forces (*i.e.* the protein's charge is almost neutralised at pH near their pI).³⁶⁶ Therefore, proteins tend to aggregate at those pH, driving the aggregation of the nanoparticles bound to them.

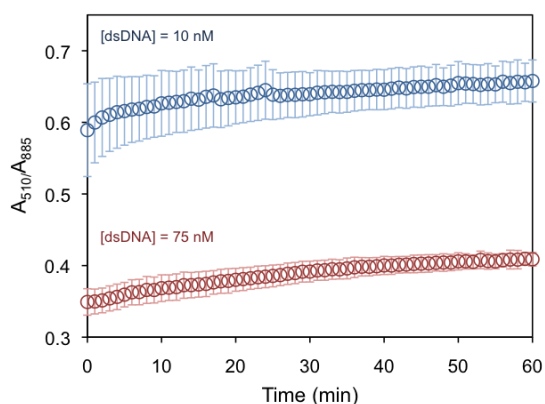


Fig. 6.5. Variation of dsDNA-AuNR absorbance ratio intensities at 510 and 885 nm after addition of Tris buffer over time. The volumes of Tris added into the system are the same as the ones added in the protein-dsDNA binding assays, *i.e.* 4 μ L of 12.5 mM Tris and 6.5 μ L of 50 mM Tris at 10 and 75 nM dsDNA, respectively.

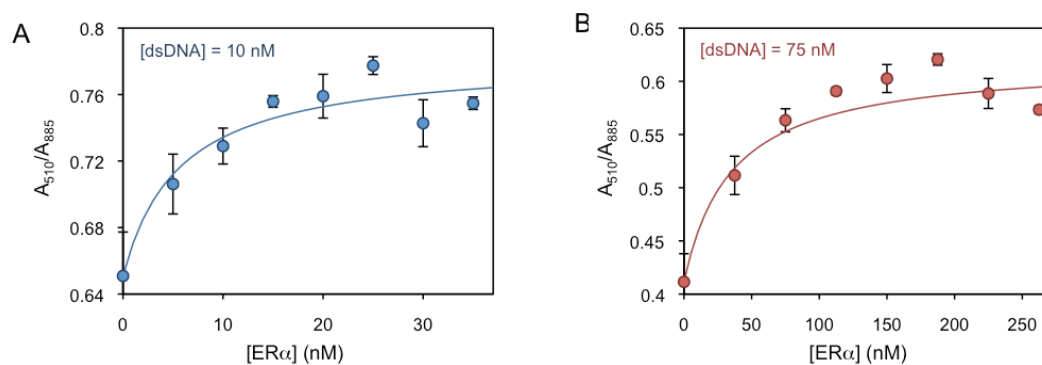


Fig. 6.6. AuNR absorbance intensity ratio at 510 and 885 nm as function of $ER\alpha$ concentration at (A) 10 and (B) 75 nM dsDNA.

Even though the DNA-binding domains of $ER\alpha$ and $ER\beta$ are highly conserved (96 % identity),³⁶⁷ their binding behaviour to ERE presents a significant difference. Fig. 6.7 plots the binding curve of $ER\beta$ to ERE-containing dsDNA on AuNRs at pH 8.5, using the A_{510}/A_{885} ratio as the binding signal. The transcription factor induces the aggregation of dsDNA-AuNR as previously observed for $ER\alpha$, *i.e.* increasing the A_{510}/A_{885} ratio. Nevertheless the stoichiometry between $ER\beta$ and ERE is approximately 4 to 1. This observation is in agreement with previous reports, which studied the $ER\beta$ -ERE binding by surface plasmon resonance spectroscopy.³⁶⁸

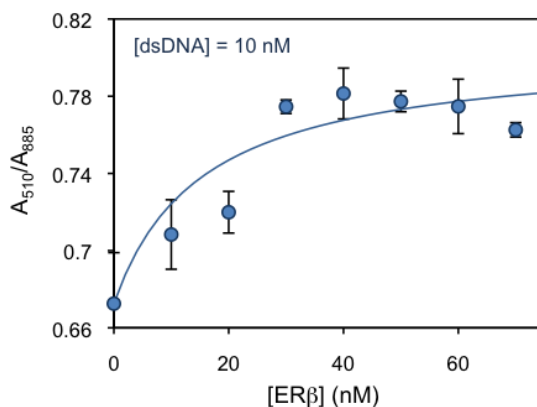


Fig. 6.7. AuNR absorbance ratio intensities at 510 and 885 nm as function of $ER\beta$ concentration at 10 nM dsDNA.

In a control experiment, the interaction between ERE-containing dsDNA and a control protein without a binding site for the ERE was studied. Lysozyme is a basic monomeric protein with pI of 11.2³⁶⁹ and it is positively charged at the pH ~ 8.0 of this study. Fig. 6.8 plots the lysozyme-induced dsDNA-AuNR aggregation profile at 10 nM and 75 nM dsDNA, as done for $ER\alpha$ experiments. The dsDNA-AuNRs are positively charged at 10 nM dsDNA and the addition of lysozyme barely aggregate the nanoparticles within a protein concentration range of 0 to 50 nM. We hypothesize that dsDNA-AuNR and lysozyme electrostatically repel each other because of their positive charges. On the

other hand, dsDNA-AuNRs are negatively charged at 75 nM dsDNA and the positively charged lysozyme can aggregate them. This is because the negatively charged dsDNA-AuNRs and the positive lysozyme are electrostatically attracted to each other. The difference between sequence-specific and non-sequence-specific binding can be observed by comparing the aggregation profiles induced by ER α and lysozyme: under the experiment conditions, the sequence-specific interaction with ER α triggers the aggregation of the nanoparticles in both dsDNA concentration regimes and it is independent of the nanoparticle's surface charge; on the other hand, the non-sequence specific interaction with lysozyme requires strong electrostatic forces between AuNRs and proteins to induce the nanoparticle's aggregation and it only occurs when AuNRs and proteins present opposite charges.

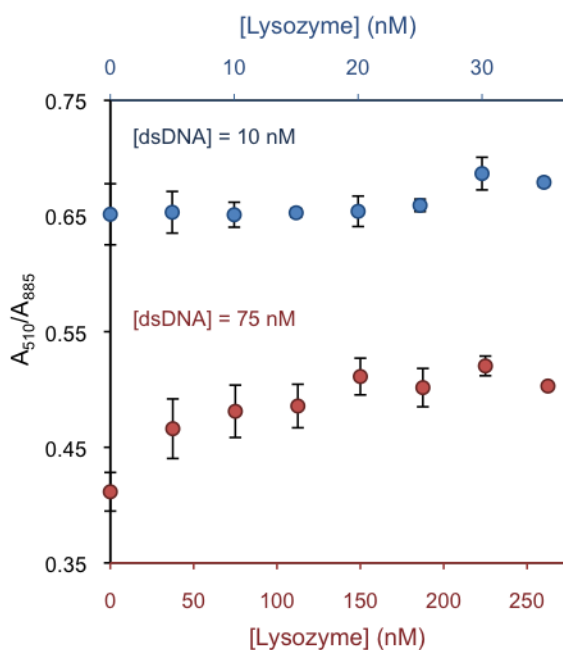


Fig. 6.8. AuNR absorbance ratio intensities at 510 and 885 nm as function of Lysozyme concentration in the presence of dsDNA of (blue) 10 nM and (red) 75 nM.

6.3.3 Building a multi-logic gate platform

At this point, we have proved that AuNR's aggregation profiles can be used to sense protein-dsDNA interactions. We then further explored the combination of proteins, ERE-containing dsDNA and AuNRs to build a platform capable of performing logic operations at nanoscale.

We built logic gates by adding proteins or dsDNA (logic inputs) into a base solution consisting of AuNR (Au⁰ concentration of 257 μ M) and dsDNA of 10 nM (leading to dispersed AuNRs) or 25 nM (leading to aggregated AuNRs). The logic values of the

inputs are 0 and 1, which are defined as the absence and the presence of the input in solution, respectively. The outputs are read by measuring the variation of A_{510}/A_{880} ratio, where the logic 0 and 1 values are experimentally established as 0.65 and 0.75, respectively. The amount of input added into the solutions was experimentally optimized, so that the output signals are coherent in all the logic gates. First, the logic gate OR was built (Fig. 6.9A). The base solution contains AuNRs and dsDNA (10 nM), and the two inputs are ER α (20 nM) and ER β (30 nM). Both inputs induce similar level of aggregation when separately added (0/1 and 1/0). Interestingly, when both ERs are added at the same time (1/1), a similar level of aggregation is obtained, rather than a higher one. This is most likely because of the amount of ERE-containing dsDNA is the limiting factor. Thus, the excess of ERs does not bind to the dsDNA and it is left in solution without interacting with the nanoparticles. Next, the NOT gate was designed (Fig. 6.9B). It is a 1-input 1-output gate that performs logic negation. The base solution contains AuNRs and 25 nM dsDNA, which aggregates the nanoparticles (0/0). When more dsDNA (additional 15 nM) is added as an input in a second step, the nanoparticles disaggregate (1/1). OR and NOT are basic operations and all the rest can be obtained through them. It is worth mentioning that derivative operation gates can be built with this design without the need of combining different basic operations. First, A IMPLY B gate was developed by using a base solution with AuNRs and 25 nM dsDNA (Fig. 6.9C). The two inputs are dsDNA (additional 15 nM) and ER β (30 nM). In the initial state (0/0), the nanoparticles are aggregated. When more dsDNA is added (1/0), the new dsDNA triggers the AuNR disassembly. The single addition of ER β (0/1) does not change the aggregation state of the nanoparticles because they are already aggregated. The addition of both inputs (1/1) results in AuNR aggregation, since dsDNA's disassemble capacity is neutralized by ER β aggregating behaviour. Next, the BUFFER logic gate was demonstrated. A base solution made of AuNRs and 10 nM dsDNA, and one input (20 nM ER α) are required (Fig. 6.9D). The mechanism of this gate is based on the further aggregation of dsDNA-AuNR induced by ER α (1). TRUE logic gate could also be obtained. This was constructed by using a base solution of AuNRs and 25 nM dsDNA (Fig. 6.9E). The two inputs are ER α (20 nM) and ER β (30 nM). Since the nanoparticles are already aggregated in the initial state (0/0), the addition of ERs does not significantly change the aggregation state of the system. Lastly, the FALSE gate was built (Fig. 6.9F). The base solution contains AuNRs and 10 nM dsDNA, and the inputs are lysozyme (20 nM) and dsDNA (additional 27 nM). In the initial state, the AuNRs are dispersed (0/0). Lysozyme does not interact with ERE-containing dsDNA, and its addition (1/0) does not affect the aggregation state. The

addition of extra 27 nM dsDNA keeps the nanoparticles disaggregated (0/1 and 1/1). Based on the previous zeta potential results, we hypothesize that the amount of dsDNA in solution is enough to induce a nanoparticle charge reversal and provide enough electrostatic repulsion to disaggregate the AuNRs. It is worth mentioning that even though this is a multi-component system, the sequence-specific binding is essential for building four of the six logic gates (*i.e.* OR, A IMPLY B, BUFFER and TRUE). Limited number of logic operations (*i.e.* NOT and FALSE) can be performed by using only dsDNA and/or non-specific binding protein as inputs.

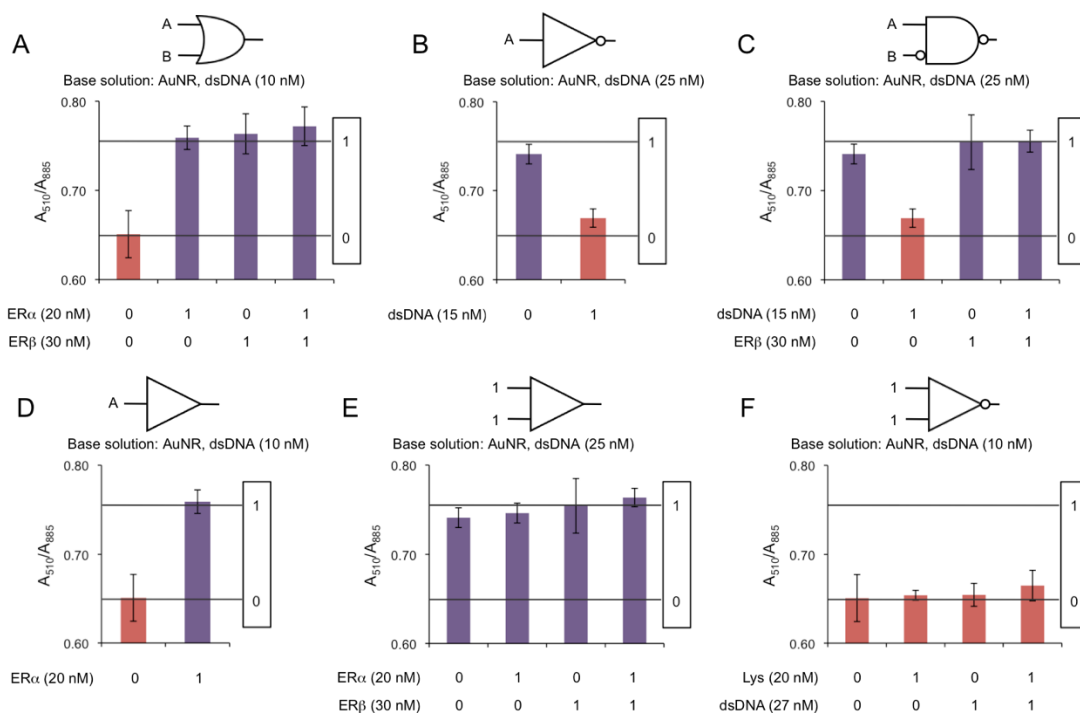


Fig. 6.9. AuNR absorbance ratio intensities at 510 and 885 nm as function of different inputs in (A) OR, (B) NOT, (C) A IMPLY B, (D) BUFFER, (E) TRUE, and (F) FALSE logic gates.

Finally, the results from the logic gate experiments were statistically assessed, rendering two conclusions: 1) All the A_{510}/A_{885} outputs were successfully labelled as logic 0 or 1 values, since they were not statistically different from one of the two reference values, *i.e.* 0.65 and 0.75, respectively ($p > 0.05$, Table S6.1); 2) the values for logic 0 are statistically different and clearly distinguishable from the values for logic 1 ($p < 0.05$, Table S6.2; Cohen's $d > 3.5$, Table S6.3).

6.4 Conclusions

In summary, we have developed a plasmonic hybrid system made of AuNR and ERE-containing dsDNA capable of tracking the binding of ERs (*i.e.* ER α and ER β) to their response element. The system is sensitive enough to distinguish between protein isomorphs. The mechanism is based on the interprotein interactions among ERs, which are bound to dsDNA on the surface of AuNRs under sequence recognition, and trigger the nanoparticle's aggregation. The combination of proteins, ERE-containing dsDNA, AuNRs and the interactions among them allow expanding the system to a plasmonic logic gate platform, becoming the first system that performs logic operations by mimicking transcription factor's gene regulation. This versatile system is able to perform 6 different logic operations (*i.e.* OR, NOT, A IMPLY B, BUFFER, TRUE and FALSE) by changing the design set-up. This overcomes one of the main limitations of traditional nanoscale logic gates, which are just able to perform few logic operations with the same platform. Furthermore, this system is conceptually simple, easy-to-use and does not require complex surface modifications, toxic ligands or separation/purification steps. Lastly, those new insights on the spatial and temporal control over nanomaterial assembly by transcription factors can be the first steps for other nanoscale technologies, such as transcription factor-mediated smart drug release.

6.5 Annex

Table S6.1. p -values obtained by one-sample Student's t -test, to study if the differences between the A_{510}/A_{885} ratios from the logic gate experiments and the reference values are statistical significant.

Logic Gate	Input	A_{510}/A_{885}	St Dev	Reference value	p
OR	(0/0)	0.651	0.026	0.650	0.896
	(1/0)	0.759	0.013	0.750	0.260
	(0/1)	0.763	0.022	0.750	0.414
	(1/1)	0.772	0.022	0.750	0.225
NOT	(0)	0.741	0.011	0.750	0.292
	(1)	0.669	0.010	0.650	0.081
A IMPLY B	(0,0)	0.741	0.011	0.750	0.292
	(1,0)	0.669	0.010	0.650	0.081
	(0,1)	0.754	0.031	0.750	0.844
	(1,1)	0.755	0.012	0.750	0.546
BUFFER	(0)	0.651	0.026	0.650	0.896
	(1)	0.759	0.013	0.750	0.260
TRUE	(0,0)	0.741	0.011	0.750	0.292
	(1,0)	0.746	0.011	0.750	0.593
	(0,1)	0.754	0.031	0.750	0.844
	(1,1)	0.764	0.010	0.750	0.136
FALSE	(0,0)	0.651	0.026	0.650	0.896
	(1,0)	0.654	0.006	0.650	0.368
	(0,1)	0.655	0.013	0.650	0.574
	(1,1)	0.665	0.017	0.650	0.083

Table S6.2. p -values obtained by Welch t-test (unequal variances t-test), to study if the differences between the A_{510}/A_{885} ratios from the logic 0 and 1 values are statistical significant.

Logic Gate	Input 1	A_{510}/A_{885}	St Dev	Input 2	A_{510}/A_{885}	St Dev	p
OR	(0,0)	0.651	0.026	(1,0)	0.759	0.013	< 0.001
	(0,0)	0.651	0.026	(0,1)	0.763	0.022	0.005
	(0,0)	0.651	0.026	(1,1)	0.772	0.022	0.004
NOT	(0)	0.741	0.011	(1)	0.669	0.010	0.004
A IMPLY B	(0,0)	0.741	0.011	(1,0)	0.669	0.010	0.004
	(0,1)	0.754	0.031	(1,0)	0.669	0.010	0.046
	(1,1)	0.755	0.012	(1,0)	0.669	0.010	0.002
BUFFER	(0)	0.651	0.026	(1)	0.759	0.013	< 0.001

Table S6.3. Cohen's d -values calculated to study the standardised differences between the A_{510}/A_{885} ratios from the logic 0 and 1 values.

Logic Gate	Input 1	A_{510}/A_{885}	St Dev	Input 2	A_{510}/A_{885}	St Dev	d
OR	(0,0)	0.651	0.026	(1,0)	0.759	0.013	4.53
	(0,0)	0.651	0.026	(0,1)	0.763	0.022	4.41
	(0,0)	0.651	0.026	(1,1)	0.772	0.022	4.76
NOT	(0)	0.741	0.011	(1)	0.669	0.010	6.85
A IMPLY B	(0,0)	0.741	0.011	(1,0)	0.669	0.010	6.85
	(0,1)	0.754	0.031	(1,0)	0.669	0.010	3.69
	(1,1)	0.755	0.012	(1,0)	0.669	0.010	7.79
BUFFER	(0)	0.651	0.026	(1)	0.759	0.013	4.53

Chapter 7

Hybrid Bioassay Based on Graphene Oxide and Conjugated Polyelectrolytes for Studying Protein-DNA Interactions

A new analytical bioassay to study protein-DNA binding is built by combining the optical properties of water soluble conjugated polyelectrolytes and the graphene oxide superquenching capabilities. The binding of protein to double stranded DNA induces electrostatic changes in the hybrid system that increases the conjugated polyelectrolyte fluorescence quenching.

7.1 Introduction

Conjugated polyelectrolytes (CPEs) are polymers made of two different parts.³⁷⁰ First, a π -conjugated backbone that defines a set of optical properties, such as strong fluorescence, light-harvesting and high quantum yield. Second, ionic side-chains that provide strong electrostatic interactions and high solubility in water. Due to those properties, CPEs have been used as key components in many biosensing assays.³⁷⁰ Early designs exploited the Förster resonance energy transfer (FRET) between a dye-labelled PNA and CPEs to detect ssDNA.^{371,372} When the two oligos hybridized, the negative charge of the ssDNA brought the hybrid complex and the positive CPEs in close proximity, enhancing the FRET. Later works replaced the PNA for dye-labelled ssDNA molecules.³⁷³

Since those early designs, similar CPE-based assays have been developed for the detection of other relevant medical targets, such as DNA with single-nucleotide polymorphisms,³⁷⁴ proteins,³⁷⁵ ATP³⁷⁶ and ions.^{377,378}

Graphene oxide (GO) is a one atom thick sheet of graphite with different oxygen-containing functional groups (*i.e.* carboxyl, hydroxyl and epoxy groups) decorating both the basal plane and the edges.³⁷⁹ This results in a two-dimensional nanomaterial made of a mixture of sp²- and sp³- carbon atoms. GO can improve the performance of CPE-based biosensors³⁸⁰ due to its long-range fluorescence superquenching,³⁸¹ water solubility³⁸² and special interaction with CPEs,^{383,384} such as the strong π - π stacking between CPE aromatic parts and graphene oxide hexagonal cells. Therefore, new assays based on both GO and CPEs have been developed for the detection of different clinically relevant analytes, such as DNA,^{380,385} miRNA,³⁸⁵ proteins³⁸⁶ and other biomolecules.^{387,388}

Transcription factors are proteins that up or down regulate gene transcription by binding to short sequences of DNA called response elements.³⁸⁹ Because they are key factors in many cellular processes, such as growth and cell development,^{390,391} intra and extracellular signalling,^{392,393} and cell cycle,³⁹⁴ several diseases have been linked to transcription factors malfunction (*e.g.* cancer,³⁹⁵⁻³⁹⁷ congenital heart disease,³⁹⁸ renal malfunction³⁹⁹ and chronic inflammation condition^{400,401}). Therefore, the study of transcription factors binding to DNA has also become of clinical significance, since it can reveal gene transcription mechanisms that can lead to new therapies.

Recently, a CPE-based hybrid sensor has been developed for characterizing the sequence-specific bindings of transcription factors.^{156,157} The system exploited the fluorescence quenching of CPEs by gold nanoparticles. The use of dual transducers

and the FRET principle improves the sensor performance in comparison to the colorimetric sensing using solely metal nanoparticles.⁴⁰² A recent study has compared the performance of different nanomaterial quenchers (*i.e.* gold nanoparticles, carbon nanotubes and GO) in DNA sensing assays involving the fluorescence quenching of dye-labelled DNA. The report concludes that the GO-based assay presents a higher sensitivity and repeatability than the others due to GO higher quenching efficiency and kinetics.⁴⁰³

In this work, we explore the collaborative role of CPEs and GO for studying the transcription factor-DNA binding. Two CPEs, which present same backbone but different overall charge (*i.e.* one positive and the other negative), are used in collaboration with GO to form a FRET sensor. Three oncogenic transcription factors, which jointly regulate estrogen gene transcription through cooperative binding to DNA, are used as case study, *i.e.* estrogen receptor α (ER α), forkhead boxA1 (FoxA1) and activating enhancer binding protein 2 gamma (AP-2 γ). ER α is a transcription factor activated by estrogen,³⁶⁰ which regulates several biological functions, such as the development and maintenance of the reproductive system and bone structure. FoxA1 and AP-2 γ act as pioneer factors in the estrogen signalling pathway,^{404,405} affecting the protein-binding, chromatin looping and gene transcription performed by ER α . The GO-CPE hybrid system that we have developed exploits the strong fluorescence and light-harvesting capabilities of CPE and the superquenching properties of GO, resulting on a sensitive, easy-to-use and fast biosensing technique for protein-DNA binding characterization. The detection of the protein-DNA binding is based on protein binding-modulated CPE quenching by GO in the presence of dsDNA. This assay strategy overcomes the main limitations of previous protein-DNA binding sensing designs: it does not require complex surface modifications^{156,157} or enzyme-based signal generation,⁴⁰⁶ and it does not suffer from non-specific interaction interferences.⁴⁰²

7.2 Experimental section

7.2.1 Materials

The following products were used as received. Graphene oxide (2 mg/ml, dispersion in H₂O), poly[(2,5-bis(2-(N,N-diethylammonium bromide)ethoxy)-1,4-phenylene)-alt-1,4-phenylene] (Mn of 745 Da and Mw of 1054 Da), poly(2,5-bis(3-sulfonatopropoxy)-1,4-phenylene, disodium salt-alt-1,4-phenylene) and bovine serum albumin (BSA) were purchased from Sigma-Aldrich. Human recombinant estrogen receptor α (ER α) was purchased from Life Technologies, ThermoFisher Scientific. FoxA1 and AP-2 γ were prepared as HisMBP-tagged recombinant proteins as described in a previous publication.¹⁵⁷ The oligos used in this study were purchased from Integrated DNA Technologies. Table 7.1 shows their sequences. The probe 1 is a DNA that contains binding sites for ER α and AP-2 γ . The probe 2 is a FAM labelled DNA, which contains a binding site for ER α . To form dsDNA, the sense and antisense strands were annealed at 95 °C for 5 min and cooled down for 3 h in 10 mM Tris-HCl buffer (pH 7.0). All the water employed in the experiments was obtained with a Mili-Q Integral 5 system.

Table 7.1. Oligonucleotides sequences

Name	Sequence 5' to 3'
Probe 1	GGGATGACACA <u>GGTCA</u> CTGT <u>TGACC</u> ACCAGT <u>GCCCCAGGC</u> ACCGGGACCT
Probe 1-rev	AGGTCCCGGTGCCTGGGGCACTGGTGGTCACAGTGACCTGTGTCATCCC
Probe 2	ACTTTGATCA <u>GGTCA</u> CTGT <u>TGACC</u> TGACTTTGGAC
Probe 2-rev	[6FAM]-GTCCAAAGTCAGGTCACAGTGACCTGATCAAAGT

GGTCAnnnTGACC = ER α binding site

GCCCCAGGC = AP-2 γ binding site

7.2.2 Characterization

The emission and excitation spectra were obtained by an InfiniteM200 from Tecan. The zeta potential measurements were recorded with a Zetasizer Nano Z from Malvern Instruments. pH was measured with an 827 pH lab from Metrohm. Fluorescence polarisation was measured with a Synergy 2 Multi-Mode Microplate Reader from BioTek with 485/20-excitation and 528/20-emission filters.

7.2.3 CPE fluorescence quenching by GO in the presence of dsDNA

dsDNA (probe 1) solutions with different concentrations were prepared in 10 mM Tris-HCL buffer (pH 7.0). 5 μ L of those solutions were added into 35 μ L CPE solutions (100 μ g/L in 10 mM Tris-HCL pH 7.0) and the mixtures were incubated at room temperature for 10 min. 30 μ L of GO (200 μ g/mL in Tris-HCL pH 7.0) were then added into the dsDNA/CPE solutions and the resulting mixtures were left incubating at room temperature for 15 min. The final dsDNA concentration in the solutions ranged from 0 to 1000 nM. Last, the fluorescence spectra of the resulting solutions were measured.

7.2.4 Protein-DNA binding assay

The assay procedure is similar to that of 7.2.3, except that prior to GO addition, protein is added to the dsDNA/CPE solutions. Specifically, the binding assays were performed by incubating 15.5 μ L solutions made of positively charged CPE (final concentration of 50 μ g/L) and probe 1 (dsDNA final concentration of 100 nM) in 10 mM Tris-HCL pH 7.0 at room temperature for 10 min. The resulting solutions were mixed with 24.5 μ L of different diluted protein solutions ($ER\alpha$, FoxA1 and AP-2 γ in 10 mM Tris-HCL buffer, pH 7.0) and the mixtures were incubated for another 30 min at room temperature. Finally, 30 μ L of GO (200 μ g/mL) were added and incubated for 15 min at room temperature. The final protein concentrations ranged from 0 to 350 nM. Finally, the fluorescence spectra of the resulting solutions were measured.

7.2.5 Assay for fluorescence polarisation measurement

The fluorescence polarisation assay was performed by incubating 15.5 μ L solutions made of positively charged CPE (final concentration of 0 or 50 μ g/L) and probe 2 (final dsDNA concentration of 40 nM) in 10 mM Tris-HCL pH 7.0 at room temperature for 10 min. The resulting solutions were mixed with 54.5 μ L of different protein solutions ($ER\alpha$ or BSA in 10 mM Tris-HCL buffer, pH 7.0) and the mixtures were incubated for another 30 min at room temperature. The final protein concentrations were 100 nM for the protein-dsDNA binding assays and 0 nM for the controls. Lastly, the fluorescence polarisations of the resulting solutions were measured.

7.3 Results and discussion

7.3.1 Fluorescence quenching and recovery between GO and CPE in the absence and presence of dsDNA

Two CPEs were involved in this study. Both CPEs had the same backbone but different side chains, which provided different overall electrostatic charge. Poly[(2,5-bis(2-(*N,N*-diethylammonium bromide)ethoxy)-1,4-phenylene)-*alt*-1,4-phenylene] was the positive CPE (**CCPE**, Fig. 7.1A) and poly(2,5-bis(3-sulfonatopropoxy)-1,4-phenylene, disodium salt-*alt*-1,4-phenylene) the negative one (**ACPE**, Fig. 7.1B). Both CPEs present similar emission profiles (Fig. 7.1C and D), which is expected since they have the same backbone chain. When GO was mixed with the two CPE solutions, the CPEs' emission was quenched. Interestingly, the degree of fluorescence quenching (η) was higher for ACPE than for CCPE (*i.e.* η of 77 and 69 %, respectively), although the ACPE and GO have alike charge that is unfavourable for electrostatic attraction. Those results are in agreement with previous studies, which reported that GO and CPEs interact through strong π - π stacking besides electrostatic interactions.^{383,384} The stronger ACPE fluorescence quenching, which indicates a stronger interaction between ACPE and GO, suggests that the π - π stacking interactions dominate over electrostatic interactions.

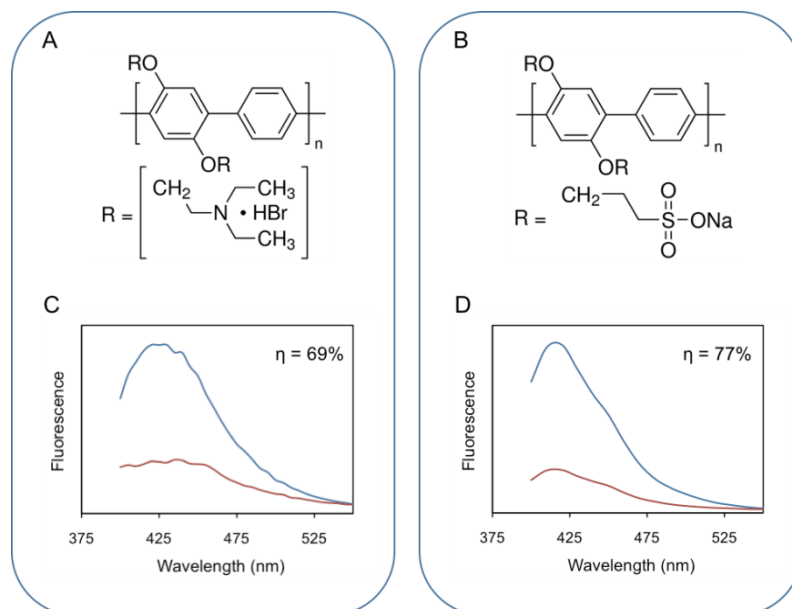


Fig. 7.1. Chemical structures of (A) CCPE and (B) ACPE. Emission spectra of (C) CCPE and (ACPE) in the presence (red line) or absence (blue line) of GO.

DNA, as a negatively charged biopolymer, has been largely studied for its electrostatic interactions with other charged materials.⁴⁰⁷ In a previous study, we have employed the absorption of dsDNA on gold nanorods to change their overall charge and the way DNA coated gold nanorods interact with the other nanoparticles in solution.²⁰¹ In this study, we first examine the effect of dsDNA on the interaction between CPEs and GO prior to the protein binding experiments. In a two-step procedure, CPEs were first incubated with dsDNA to favour their interaction. The probe 1, *i.e.* a dsDNA that contains binding sites for ER α (estrogen receptor element, ERE) and AP-2 γ , was used in these experiments. After 10 min, the hybrid dsDNA-CCPE complex was exposed to GO. Fig. 7.2A shows CCPE fluorescence recovery with increasing dsDNA (probe 1) concentration. The interaction between CCPE and dsDNA molecules is electrostatically favoured because their opposing charges. On the other hand, the ACPE fluorescence does not change upon addition of dsDNA (Fig. 7.2B). The lack of interaction between ACPE and dsDNA can also be understood from an electrostatic point-of-view, where both molecules are negatively charged and repel each other. Fig. 7.2C plots the variation of fluorescence ($F-F_0/F_0$) as a function of dsDNA concentration for the CCPE and ACPE. CCPE spectrum presents a fluorescence recovery curve with hyperbolic shape, while ACPE fluorescence shows no variation within the experimental dsDNA concentration range.

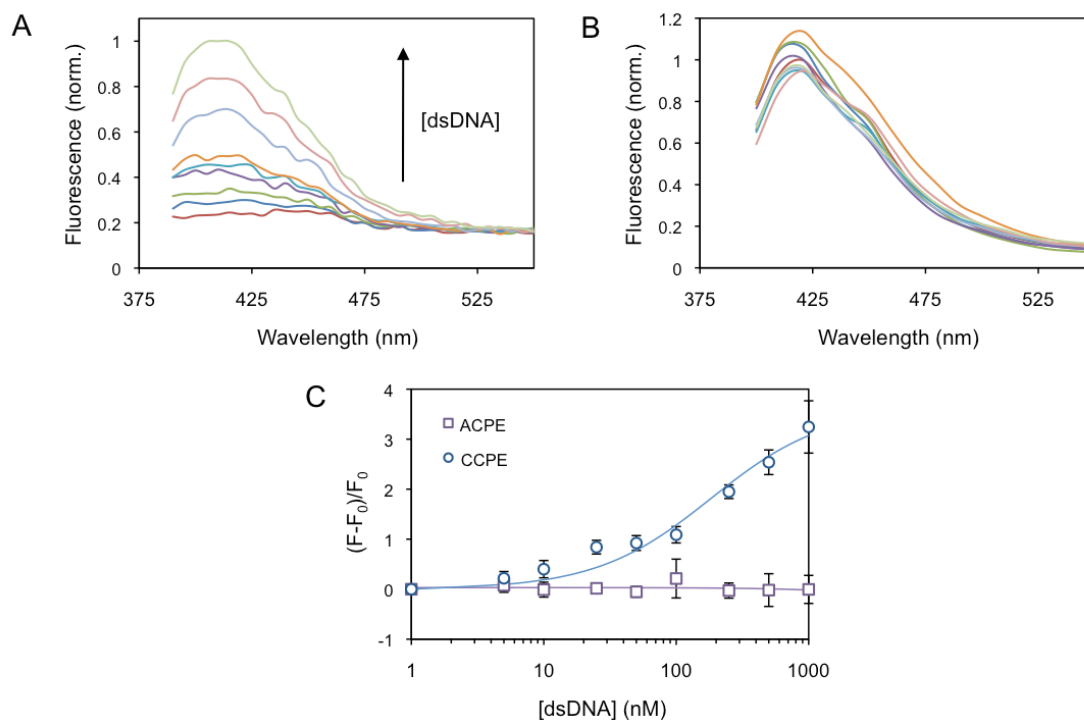


Fig. 7.2. Emission spectra of (A) CCPE and (B) ACPE in the presence of GO and different dsDNA concentrations (*i.e.* 0, 1, 5, 10, 25, 50, 100, 250, 500 and 1000 nM). (C) Fluorescence variation of CCPE (λ_{\max} of 410 nm) and ACPE (λ_{\max} of 420 nm) in the presence of GO and different dsDNA concentrations.

The zeta potentials of GO and CCPE (before and after the addition of different amounts of dsDNA) were measured to further understand the mechanism involved in the fluorescence recovery of CCPE by the dsDNA. It is confirmed that, GO (85.7 $\mu\text{g/mL}$) and CCPE (50 $\mu\text{g/L}$) in absence of dsDNA present opposite charges in solution, with zeta potential of -31.8 and +18.3 mV, respectively (Fig. 7.3). The addition of dsDNA into the CCPE solution turns the overall charge from positive down to -14.4 mV at 100 nM dsDNA, where the molar amount of dsDNA is twice of the CCPE. These results suggest that dsDNA and CCPE form a hybrid complex due to electrostatic interaction, and the overall complex is negatively charged due to the phosphate backbone of the dsDNA. The consequent fluorescence recovery is probably the result of two factors. Firstly, dsDNA covers the polyelectrolyte structure on the dsDNA-CCPE complex and blocks the π - π stacking interactions between GO and CCPE. Secondly, the negatively charged dsDNA-CCPE complex introduces electrostatic repulsion between GO and CCPE. Those two factors, *i.e.* lack of π - π stacking interaction and electrostatic repulsion, promote the separation between GO and CCPE, decreasing the fluorescence quenching observed in Fig. 7.2A. We can exclude the absorption of dsDNA on GO as a cause of the fluorescence recovery, because it is well reported that dsDNA has very limited affinity for GO.⁴⁰⁸

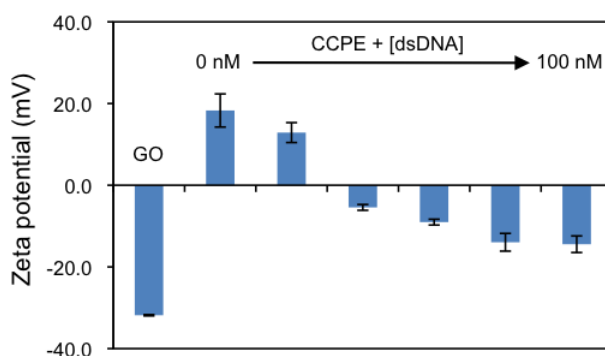


Fig. 7.3. Zeta potential of GO and CCPE in the presence of different dsDNA concentrations (*i.e.* 0, 5, 10, 25, 50 and 100 nM).

7.3.2 Fluorescence quenching promoted by protein-DNA binding

Following the earlier study of how negatively charged dsDNA can push away the CCPE from GO surface, a new analytical assay for protein-DNA binding has been designed. This exploits the ability of transcription factors to bring the CCPE closer to GO, due to the change of the electrostatic behaviour of the DNA.^{156,157} A human estrogen receptor subtype, ER α , was used as proof of concept. Fig. 7.4 depicts the

three steps of the proposed analytical assay: First, CCPE is incubated with probe 1 (*i.e.* dsDNA that contains both ER α and AP-2 γ binding sites). A dsDNA concentration of 100 nM is used in order to obtain a negatively charged dsDNA-CCPE hybrid with 50 $\mu\text{g/L}$ CCPE (molar ratio of dsDNA:CCPE \sim 2:1). Second, the dsDNA-CCPE hybrid is exposed to the ER α , allowing the transcription factor to bind to the dsDNA. Third, GO is added into the mixture and the fluorescence is measured after the incubation time. Since the final pH of the mixture is 7.68, ER α is positively charged in the assay solution (isoelectric point, pI of 8.3)³⁶⁵. Therefore, when ER α binds to its binding site in the dsDNA, it changes the overall negative charge of dsDNA-CCPE and decreases the electrostatic repulsion between dsDNA-CCPE and GO. This reduces their distance separation and enhances the fluorescence quenching. Two negative controls (*i.e.* FoxA1 and AP-2 γ) were employed to confirm the role of the protein-DNA binding and the ER α positive charge in the fluorescence quenching enhancement. On one hand, FoxA1 is a transcription factor that presents similar electrostatic behaviour to ER α (pI of 8.9)⁴⁰⁹ but does not bind to the dsDNA employed in the assay (probe 1). On the other hand, AP-2 γ presents neutral charge in the assay solution (pI of 7.7)⁴¹⁰ but it can bind to probe 1 because the DNA molecule contains a binding site for this protein.

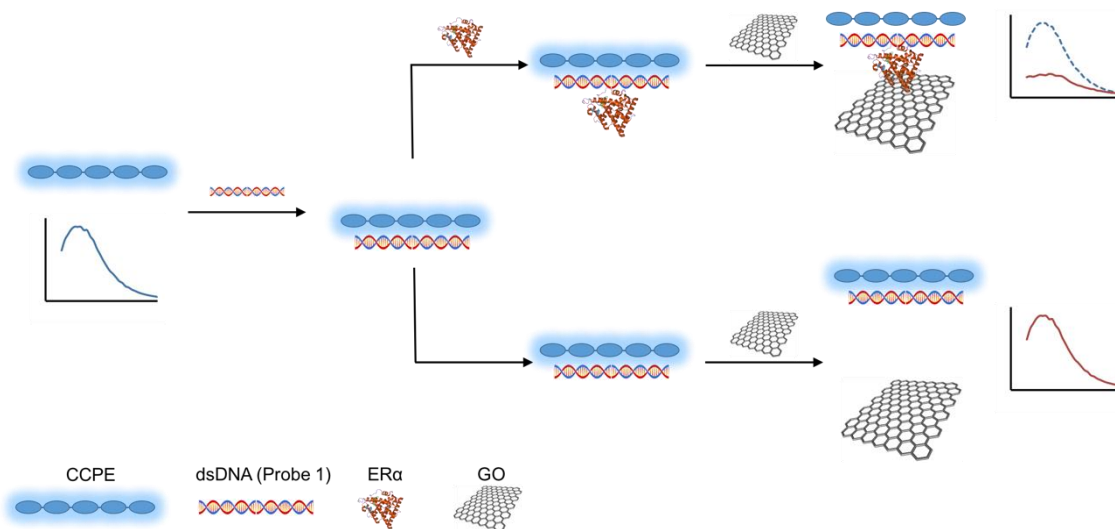


Fig. 7.4. Three step analytical assay based on CCPE and GO for protein-DNA interaction characterization.

Fig. 7.5A depicts the fluorescence emission of the hybrid dsDNA-CCPE in the presence of GO and different amounts of ER α . The fluorescence emission of dsDNA-CCPE decreases with the addition of ER α in a concentration range from 0 to 200 nM. Above those ER α concentrations, the fluorescence does not significantly change. On the other hand, the additions of FoxA1 (Fig. 7.5B) or AP-2 γ (Fig. 7.5C) into the mixture induce no fluorescence decreases, but very moderate increases. Fig. 7.5D presents

the fluorescence intensity variation ($F-F_0/F_0$) as a function of transcription factor concentration. As previously observed in the fluorescence spectrum, the binding of ER α to dsDNA decreases the fluorescence intensity. ER α binds to the ERE-containing dsDNA with a stoichiometry of 2 to 1, *i.e.* ($F-F_0/F_0$) reaches saturation at 2:1 of ER α :dsDNA concentration ratio. This is in agreement with previously published literature, which reported ER α binding to ERE as a dimer.¹⁵⁶ An apparent dissociation constant (K_d) of 58.8 ± 4.5 nM was calculated with the binding isotherm generated from the Fig. 7.5D data. That value is coherent with previous literature results obtained by surface plasmon resonance spectroscopy (K_d of 61.9 nM).⁴¹¹ As mentioned earlier, the two negative controls, *i.e.* FoxA1 and AP-2 γ , do not induce fluorescence quenching but small fluorescence increases, which are linear with their concentration. These fluorescence increases could be the result of different factors, such as FoxA1 non-specific interaction with GO⁴¹² and AP-2 γ shielding the dsDNA-CCPE hybrid when binding to dsDNA, due to its neutral charge.

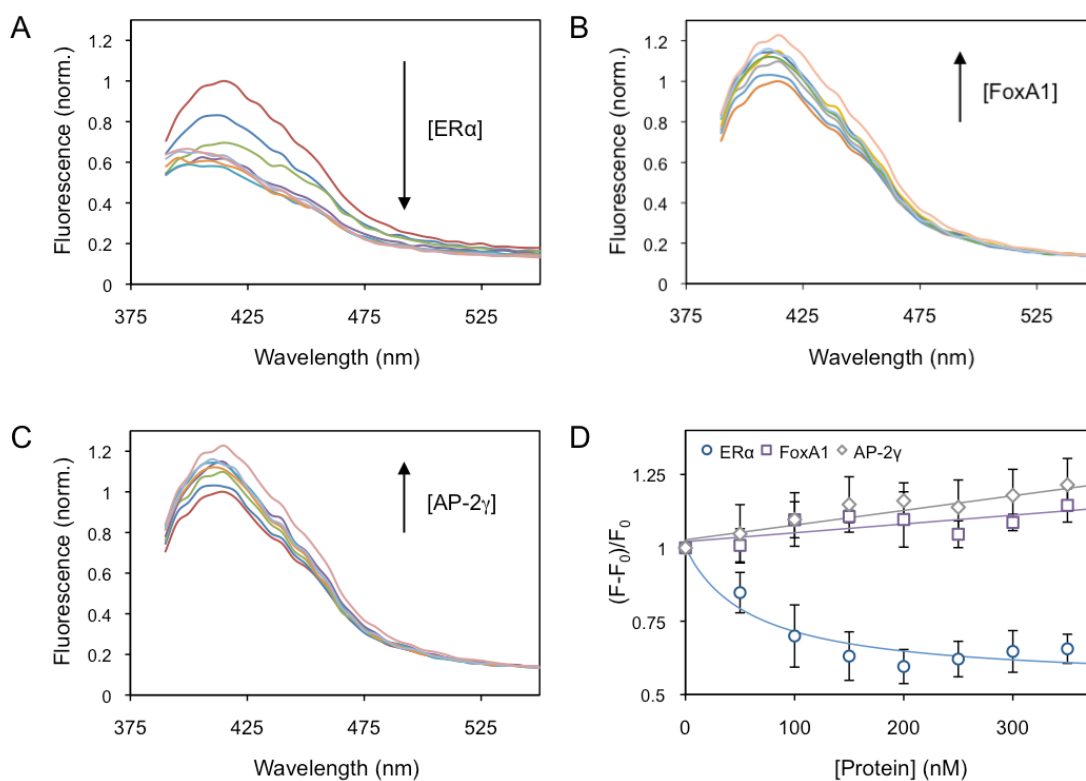


Fig. 7.5. Emission spectra of CCPE in the presence of GO, dsDNA and different protein concentrations (*i.e.* 0, 50, 100, 150, 200, 250, 300 and 350 nM). The three proteins added into the assay solution are (A) ER α , (B) FoxA1 and (C) AP-2 γ . (D) Fluorescence variation of CCPE (λ_{\max} of 410 nm) in the presence of GO, dsDNA and different protein concentrations.

The negative controls confirm that both protein-DNA binding and protein positive charge are necessary for bringing CCPE and GO in close proximity and the

fluorescence being quenched. The presence of only one of the two factors is not enough to trigger the assay response, providing double selectivity.

The above results support that ER α successfully binds to the ERE- containing dsDNA, which has been previously exposed to CCPE. To better understand the impact of CCPE on the protein-DNA binding, we employed fluorescence polarisation (FP). This is an analytical method that provides information about biomolecular interactions by measuring the degree of a fluorophore polarisation,⁴¹³ which is inversely proportional to the fluorophore rotation when is undergoing Brownian motion. When a protein binds to a dye-labelled dsDNA, the larger volume of the complex hinders the fluorophore movement, increasing its fluorescence polarisation.⁴¹⁴ Fig. 7.6 plots the FP of the FAM-labelled probe 2 (a dsDNA that contains the ERE binding site) under different conditions. Firstly, the addition of CCPE does not significantly affect the probe 2 FP. The difference between CCPE and probe 2 molecular masses is so big (*i.e.* 1.05 and 21.4 kDa, respectively) that the formation of dsDNA-CCPE does not hinder the probe 2 movement and rotation. Secondly, the addition of a non-binding protein, such as BSA, does not affect the probe 2 FP either, because no complex is formed. However, the addition of ER α (molecular mass of 65 kDa)⁴¹⁵ increases the FP from 80 to 98.5 mP, due to the formation of ER α -dsDNA complex. Similar results are obtained when the probe 2 is previously exposed to CCPE, where the addition of ER α increases the FP from 81.5 to 99.5 mP. Those results confirm that (1) ER α can bind to its binding site, even when the dsDNA is part of the dsDNA-CCPE hybrid, and (2) the ER α -DNA binding is similar in the absence or presence of CCPE.

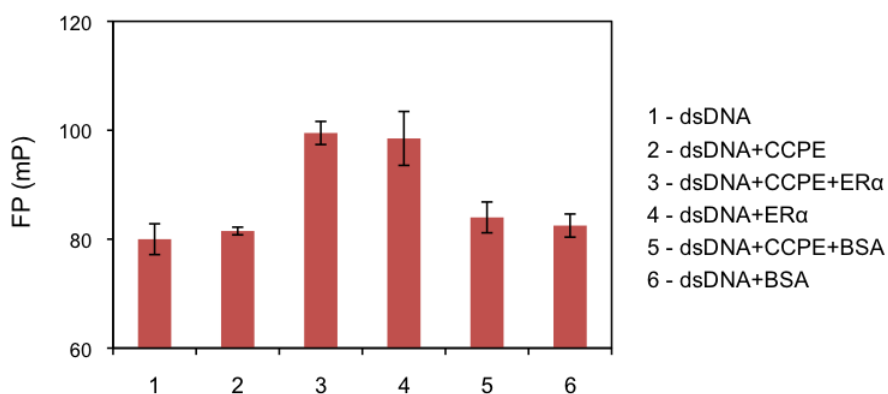


Fig. 7.6. Fluorescence polarisation of FAM-labelled dsDNA in the presence and absence of CCPE, ER α and BSA.

7.4 Conclusions

In the present work, we have developed a three step analytical assay capable of characterizing the binding of transcription factors to dsDNA that contains their binding sites. The system is made of dsDNA, CCPE and GO and exploits the exceptional optical properties of CCPE (*i.e.* strong fluorescence, light-harvesting and high quantum yield) and the superquenching capabilities of GO. The assay relies on the decrease of electrostatic repulsion between GO and dsDNA-CCPE upon protein binding, which increases the fluorescence quenching. ER α has been used as case study and two related transcription factors, *i.e.* FoxA1 and AP-2 γ , are used as controls. Those control experiments confirm that the protein-DNA binding and the protein positive charge are the two assay key factors, which provide double selectivity against other proteins. FP measurements prove that the adsorption of dsDNA on CCPE does not interfere in the protein binding. The fast and the easy-to-use nature of the hybrid system, which does not rely on complex surface modifications or enzyme-based signal generation, and its high accuracy make of this assay a promising analytical method for large-scale protein-DNA biomedical research.

Chapter 8

Conclusions and Future Work

This chapter offers an integrated view of the whole work described in the previous chapters and different opportunities and directions to further continue with this research.

8.1 Conclusions

The work described in this thesis focuses on the development of new metal nanoparticle-based techniques to face current challenges in the field of biosensing and bio-inspired materials. To achieve those objectives, the research has been performed in three stages: (1) synthesis and growth mechanism studies of anisotropic gold nanoparticles, (2) development of novel sensing assays for medical diagnosis and (3) expansion to other biological applications.

In the first stage, a new synthetic protocol for the growth of AuNRs has been developed. The motivation of this work stems from the controversy surrounding the factors that promote the anisotropic growth in the AuNR synthesis. Early reports hypothesized that the surfactant acted as soft-template,^{57,203} since CTAB had been reported assembling into rod-like micelles under specific conditions.²¹⁰ Nevertheless, new reports published in the following years supported the role of silver ion as a main anisotropic promoter factor,^{247,416} overshadowing the contributions of CTAB. *Chapter 3* presents the effect of Hofmeister salts, which interact and change the rheological properties of CTAB micelles, in the growth of AuNRs. This research proves that high control over the AuNR dimensions and optical properties can be achieved by introducing low concentrations of Hofmeister salts into the seed-mediated protocol second step, where the AuNRs grow from seeds. Furthermore, the first cryo-TEM imaging of the surfactant micelles under growth conditions allowed to observe that the CTAB micelles were mainly sphere-shaped in all growth solutions. The addition of salt increased the overall micelle size by increasing the non-spherical micelle population, although spherical shape was still the predominant one. Therefore, the key parameter in controlling the final rod morphology was the micelle packing rather than the micelle rod-shape. Those observations proved that even though silver ion may be the key component in the anisotropic growth, CTAB micelles also play an important role on defining the final morphology of the nanoparticles.

In the second stage, AuNRs (and other anisotropic gold nanoparticles) were employed for sensing and disease prevention. Specifically, two analytical assays have been developed following two novel strategies: (1) in situ growth sensing^{260,263} and (2) inverse sensitivity.³¹⁹

In situ growth sensing assays combine both nanoparticle synthesis and sensing step, where the presence of the analyte in solution controls the growth of the nanoparticles. Previous in situ growth sensing designs relied on enzyme-based signal generation,^{260,263} which increased the design complexity and experimental times.

Chapter 4 describes that the physicochemical changes induced by UV light on a photoresponsive fluid can control the growth and optical properties of AuNRs and AuNWs. Therefore, the growth of those nanoparticles in the photorheological fluid can be used as assay for UV exposure detection. Furthermore, those UV exposure levels are correlated to the minimal dose to induce erythema, expanding the analytical assay to disease prevention tool.

Chapter 5 reports a plasmonic nanosensor with inverse sensitivity (*i.e.* the lower the analyte concentration, the higher the response intensity) for cell-free DNA, a promising circulating biomarker to monitor therapeutic response and disease progression.^{313–315}

The inverse response is achieved by exploiting the unusual dsDNA concentration-dependent AuNR aggregation. The LOD and dynamic range of this technique are easily adjusted by changing the AuNR concentration in solution. The inverse sensitivity response provides higher reliability at low concentration detection. This overcomes one of the main limitations of conventional sensors, which require signal amplification techniques to cover all the physiological cell-free DNA concentration range.

In the third and final stage, the work presented in the previous chapters is expanded into two different directions. First, *Chapter 6* describes a hybrid system built with AuNRs and ERE-containing dsDNA that is capable of measuring the binding of ERs to their response elements. The mechanism behind the system relies on the interprotein interactions between bound ERs, which trigger the rod aggregation and change their optical properties. The combination of binding and non-binding proteins with the hybrid system yields the first method that performs logic operations by mimicking transcription factor's gene regulation. This system is capable of performing six different logic operations (*i.e.* OR, NOT, A IMPLY B, BUFFER, TRUE and FALSE) by changing the design set-up. This overcomes one of the main limitations of traditional nanoscale logic gates, which perform only few logic operations on the same platform.

Second, *Chapter 7* explores the use of alternative plasmonic nanomaterials, such as GO, which presents different physicochemical properties than AuNRs. By combining GO and CPEs, a new analytical assay capable of characterizing the binding of transcription factors to DNA is built. The combination of both CPE optical properties and GO super quenching capabilities results on a promising fast and easy-to-use biosensing technique. This overcomes the main limitations of previous protein-DNA binding analytical assays, such as complex surface modifications,^{156,157} enzyme-based signal generation⁴⁰⁶ and non-specific interaction interferences.⁴⁰²

8.2 Future work

The work presented in the previous chapters can be expanded into different exciting directions.

First, the in situ growth design studied in *Chapter 4* is the first step towards a new kind of portable plasmonic health care tools. Future efforts should be done in the system's set up in order to make it wearable. Some examples already exist in the field of electrochemical^{417,418} and fluorescent⁴¹⁹ biosensors. Additionally, other MNP that absorb in the visible region of the spectrum should be studied in order to facilitate the detection by naked eye.

Second, there are other very promising novel circulating cancer biomarkers (e.g. microRNA,⁴²⁰ circulating exosomes,⁴²¹ circulating tumour cells⁴²² and circulating tumour DNA⁴²³) that are still a challenge in the field of analytical chemistry. Even though the cfDNA inverse sensitivity assay presented in *Chapter 5* is not directly transferable to the other biomarkers, the inverse sensitivity strategy using plasmonic nanomaterials is an encouraging tactic to reach the low limit of detections required for those analytes. The combination of microfluidics and the designs published by Stevens *et al.*^{260,319} is a good starting point for the quantification of biomarkers such as exosomes and circulating tumor cells by inverse sensitivity strategy. However, the experimental times have to be greatly optimized.

Finally, it is expected that the combination of the multi-logic gate platform described in *Chapter 6* with microfluidic technologies could result in a lab-on-chip system capable of performing more demanding logic operations, such as the combination of different logic gates and reset the system for several consecutive operations. This would result on a biosystem capable of performing simple computing tasks.

Appendix: Publications, contributions to conferences and awards

List of publications, conference contributions and awards associated with this thesis.

Publications

- **R. M. Pallares**, M. Bosman, N. T. K. Thanh and X. Su. "Plasmonic multi-logic gate platform based on sequence-specific binding of estrogen receptors and gold nanorods" *Nanoscale*, **8**, 19973. (2016). [Front Cover]
- **R. M. Pallares**, S. H. Lim, N. T. K. Thanh and X. Su. "Growth of anisotropic gold nanoparticles in photoresponsive fluid for UV sensing and erythema prediction" *Nanomedicine*, **11**, 21, 2845. (2016).
- **R. M. Pallares**, X. Su, S. H. Lim and N. T. K. Thanh. "Fine-tuning of gold nanorod dimensions and plasmonic properties using the Hofmeister effects." *Journal of Materials Chemistry C*, **4**, 1, 53. (2016). [Front Cover]
- **R. M. Pallares**, S. L. Kong, T. H. Ru, N. T. K. Thanh, Y. Lu and X. Su. "A plasmonic nanosensor with inverse sensitivity for circulating cell-free DNA quantification." *Chemical Communications*, **51**, 77, 14524. (2015).
- **R. M. Pallares**, L. Sutarlie, N. T. K. Thanh and X. Su. "Hybrid biosensor based on graphene oxide and conjugated polyelectrolytes for studying protein-DNA interaction" (*submitted*).

Conferences

- **R. M. Pallares**, S. L. Kong, T. H. Ru, A. M. Hillmer, M. Bosman, N. T. K. Thanh, Y. Lu and X. Su. "Plasmonic nanosensor with inverse sensitivity for circulating DNA quantification" *5th IMRE Scientific Research Forum*, Singapore, Singapore. (Nov. 2015).
- **R. M. Pallares**, S. L. Kong, T. H. Ru, A. M. Hillmer, M. Bosman, N. T. K. Thanh, Y. Lu and X. Su. "Enzyme-free plasmonic nanosensor with inverse sensitivity for circulating DNA quantification" *5th Molecular Materials Meeting at Singapore*, Singapore, Singapore. (Aug. 2015).
- **R. M. Pallares**, S. H. Lim, N. T. K. Thanh and X. Su. "Growth of anisotropic gold nanoparticles in photorheological fluids" *Faraday Discussion 181: Nanoparticle Synthesis and Assembly*, Lemont, IL, USA. (Apr. 2015).

- **R. M. Pallares**, X. Su, S. H. Lim and N. T. K. Thanh. “Hofmeister effects on the synthesis and fine-tuning of high-quality gold nanorods” *Faraday Discussion 175: Physical Chemistry of Functionalised Biomedical Nanoparticles*, Bristol, UK. (Sept. 2014).

Awards

- Best presentation award at 5th IMRE Scientific Research Forum 2015 (Nov. 2015).

Bibliography

- 1 S. P. Pricker, *Gold Bull.*, 1996, **29**, 53–60.
- 2 J. W. Alexander, *Surg. Infect. (Larchmt.)*, 2009, **10**, 289–292.
- 3 A. J. Lewis and D. T. Walz, *Prog. Med. Chem.*, 1982, **19**, 1–58.
- 4 S. Chernousova and M. Epple, *Angew. Chemie - Int. Ed.*, 2013, **52**, 1636–1653.
- 5 R. Mukerji, G. Mukerji and M. McGurk, *Br. J. Oral Maxillofac. Surg.*, 2006, **44**, 222–228.
- 6 C. J. Nixon, *Trans. R. Acad. Med. Irel.*, 1891, **9**, 111–123.
- 7 H. Møllgaard, *Proc. R. Soc. Med.*, 1927, **20**, 787–796.
- 8 T. G. Benedek, *J. Hist. Med. Allied Sci.*, 2004, **59**, 50–89.
- 9 J. Forestier, *Lancet*, 1932, **219**, 441–444.
- 10 J. Forestier, *Lancet*, 1934, **224**, 646–648.
- 11 P. L. Mottram and S. Feature, *Immunol. Cell Biol.*, 2003, **81**, 350–353.
- 12 M. C. Daniel and D. Astruc, *Chem. Rev.*, 2004, **104**, 293–346.
- 13 M. Brust and C. J. Kiely, *Colloids Surfaces A Physicochem. Eng. Asp.*, 2002, **202**, 175–186.
- 14 K. L. Kelly, E. Coronado, L. L. Zhao and G. C. Schatz, *J. Phys. Chem. B*, 2003, **107**, 668–677.
- 15 K. Saha, S. S. Agasti, C. Kim, X. Li and V. M. Rotello, *Chem. Rev.*, 2012, **112**, 2739–2779.
- 16 H. Jans and Q. Huo, *Chem. Soc. Rev.*, 2012, **41**, 2849.
- 17 V. Myroshnychenko, J. Rodríguez-Fernández, I. Pastoriza-Santos, A. M. Funston, C. Novo, P. Mulvaney, L. M. Liz-Marzán and F. J. García de Abajo, *Chem. Soc. Rev.*, 2008, **37**, 1792–1805.
- 18 P. K. Jain, X. Huang, I. H. El-Sayed and M. A. El-Sayed, *Acc. Chem. Res.*, 2008, **41**, 1578–1586.
- 19 G. Mie, *Ann. Phys.*, 1908, **330**, 377–445.
- 20 L. M. Liz-Marzán, *Langmuir*, 2006, **22**, 32–41.
- 21 J. Pérez-Juste, I. Pastoriza-Santos, L. M. Liz-Marzán and P. Mulvaney, *Coord. Chem. Rev.*, 2005, **249**, 1870–1901.
- 22 M. L. Juan, M. Righini and R. Quidant, *Nat. Photonics*, 2011, **5**, 349–356.
- 23 P. K. Jain, K. S. Lee, I. H. El-Sayed and M. a El-Sayed, *J. Phys. Chem. B*, 2006, **110**, 7238–48.
- 24 H. Chen, X. Kou, Z. Yang, W. Ni and J. Wang, *Langmuir*, 2008, **24**, 5233–5237.
- 25 X. Liu, M. Atwater, J. Wang and Q. Huo, *Colloids Surfaces B Biointerfaces*,

- 2007, **58**, 3–7.
- 26 S. Link and M. El-Sayed, *J. Phys. Chem. B*, 1999, **103**, 4212–4217.
- 27 N. J. Halas, S. Lal, W.-S. Chang, S. Link and P. Nordlander, *Chem. Rev.*, 2011, **111**, 3913–3961.
- 28 K. H. Su, Q. H. Wei, X. Zhang, J. J. Mock, D. R. Smith and S. Schultz, *Nano Lett.*, 2003, **3**, 1087–1090.
- 29 L. A. Austin, B. Kang and M. A. El-Sayed, *Nano Today*, 2015, **10**, 542–558.
- 30 R. A. Alvarez-Puebla and L. M. Liz-Marzán, *Small*, 2010, **6**, 604–610.
- 31 C. C. Huang, Z. Yang, K. H. Lee and H. T. Chang, *Angew. Chemie - Int. Ed.*, 2007, **46**, 6824–6828.
- 32 S. A. Maier, *Plasmonics: Fundamentals and applications*, 2007.
- 33 P. K. Jain and M. A. El-Sayed, *Chem. Phys. Lett.*, 2010, **487**, 153–164.
- 34 G. C. Schatz, M. A. Young and R. P. Duyn, eds. K. Kneipp, M. Moskovits and H. Kneipp, Springer Berlin Heidelberg, Berlin, Heidelberg, 2006, pp. 19–45.
- 35 T. Chung, S. Y. Lee, E. Y. Song, H. Chun and B. Lee, *Sensors*, 2011, **11**, 10907–10929.
- 36 J. A. Creighton and D. G. Eadon, *J. Chem. Soc. Faraday Trans.*, 1991, **87**, 3881–3891.
- 37 P. Kanninen, C. Johans, J. Merta and K. Kontturi, *J. Colloid Interface Sci.*, 2008, **318**, 88–95.
- 38 N. N. M. Adnan, Y. Y. Cheng, N. M. N. Ong, T. T. Kamaruddin, E. Rozlan, T. W. Schmidt, H. T. T. Duong and C. Boyer, *Polym. Chem.*, 2016.
- 39 J. Turkevich, P. C. Stevenson and J. Hillier, *Discuss. Faraday Soc.*, 1951, **11**, 55–75.
- 40 G. Frens, *Nat. Phys. Sci.*, 1973, **241**, 20–22.
- 41 J. Kimling, M. Maier, B. Okenve, V. Kotaidis, H. Ballot and A. Plech, *J. Phys. Chem. B*, 2006, **110**, 15700–15707.
- 42 J. Polte, T. T. Ahner, F. Delissen, S. Sokolov, F. Emmerling, A. F. Thünemann and R. Kraehnert, *J. Am. Chem. Soc.*, 2010, **132**, 1296–1301.
- 43 M. Wuithschick, A. Birnbaum, S. Witte, M. Sztucki, U. Vainio, N. Pinna, K. Rademann, F. Emmerling, R. Kraehnert and J. Polte, *ACS Nano*, 2015, **9**, 7052–7071.
- 44 M. Brust, M. Walker, D. Bethell, D. J. Schiffrin and R. Whyman, *J. Chem. Soc. Chem. Commun.*, 1994, 801.
- 45 M. J. Hostetler, J. E. Wingate, C.-J. Zhong, J. E. Harris, R. W. Vachet, M. R. Clark, J. D. Londono, S. J. Green, J. J. Stokes, G. D. Wignall, G. L. Glish, M. D. Porter, N. D. Evans and R. W. Murray, *Langmuir*, 1998, **14**, 17–30.

- 46 S. W. Chen and R. W. Murray, *Langmuir*, 1999, **15**, 682–689.
- 47 M. J. Hostetler, S. J. Green, J. J. Stokes and R. W. Murray, *J. Am. Chem. Soc.*, 1996, **118**, 4212–4213.
- 48 A. G. Kanaras, F. S. Kamounah, K. Schaumburg, C. J. Kiely and M. Brust, *Chem. Commun. (Camb)*, 2002, 2294–2295.
- 49 A. C. Templeton, S. Chen, S. M. Gross and R. W. Murray, *Langmuir*, 1999, **15**, 66–76.
- 50 Y.-S. Shon, W. P. Wuelfing and R. W. Murray, *Langmuir*, 2001, **17**, 1255–1261.
- 51 S. E. Lohse, J. A. Dahl and J. E. Hutchison, *Langmuir*, 2010, **26**, 7504–7511.
- 52 M. Brust, J. Fink, D. Bethell, D. J. Schiffrin and C. Kiely, *J. Chem. Soc. Chem. Commun.*, 1995, 1655.
- 53 S. D. Perrault and W. C. W. Chan, *J. Am. Chem. Soc.*, 2009, **131**, 17042–17043.
- 54 C. Ziegler and A. Eychmüller, *J. Phys. Chem. C*, 2011, **115**, 4502–4506.
- 55 S. Link and M. a. El-Sayed, *J. Phys. Chem. B*, 2005, **109**, 10531–10532.
- 56 N. R. Jana, L. Gearheart and C. J. Murphy, *Adv. Mater.*, 2001, **13**, 1389–1393.
- 57 B. Nikoobakht and M. A. El-Sayed, *Chem. Mater.*, 2003, **15**, 1957–1962.
- 58 X. Ye, L. Jin, H. Caglayan, J. Chen, G. Xing, C. Zheng, V. Doan-Nguyen, Y. Kang, N. Engheta, C. R. Kagan and C. B. Murray, *ACS Nano*, 2012, **6**, 2804–2817.
- 59 R. M. Pallares, X. Su, S. H. Lim and N. T. K. Thanh, *J. Mater. Chem. C*, 2016, **4**, 53–61.
- 60 L. Vigderman and E. R. Zubarev, *Chem. Mater.*, 2013, **25**, 1450–1457.
- 61 L. Zhang, K. Xia, Z. Lu, G. Li, J. Chen, Y. Deng, S. Li, F. Zhou and N. He, *Chem. Mater.*, 2014, **26**, 1794–1798.
- 62 X. Ye, Y. Gao, J. Chen, D. C. Reifsnyder, C. Zheng and C. B. Murray, *Nano Lett.*, 2013, **13**, 2163–2171.
- 63 X. Ye, C. Zheng, J. Chen, Y. Gao and C. B. Murray, *Nano Lett.*, 2013, **13**, 765–771.
- 64 C. L. Nehl, H. Liao and J. H. Hafner, *Nano Lett.*, 2006, **6**, 683–688.
- 65 P. Senthil Kumar, I. Pastoriza-Santos, B. Rodríguez-González, F. Javier García de Abajo and L. M. Liz-Marzán, *Nanotechnology*, 2008, **19**, 15606.
- 66 S. Wang, Z. Teng, P. Huang, D. Liu, Y. Liu, Y. Tian, J. Sun, Y. Li, H. Ju, X. Chen and G. Lu, *Small*, 2015, **11**, 1801–1810.
- 67 F. Hao, C. L. Nehl, J. H. Hafner and P. Nordlander, *Nano Lett.*, 2007, **7**, 729–732.
- 68 L. Rodríguez-Lorenzo, R. A. Álvarez-Puebla, I. Pastoriza-Santos, S. Mazzucco,

- O. Stéphan, M. Kociak, L. M. Liz-Marzán and F. J. G. De Abajo, *J. Am. Chem. Soc.*, 2009, **131**, 4616–4618.
- 69 P. C. Lee and D. Meisel, *J. Phys. Chem.*, 1982, **86**, 3391–3395.
- 70 P. V Kamat, M. Flumiani and G. V Hartland, *J. Phys. Chem. B*, 1998, **102**, 3123–3128.
- 71 R. S. Sheng, L. Zhu and M. D. Morris, *Anal. Chem.*, 1986, **58**, 1116–1119.
- 72 A. Henglein and M. Giersig, *J. Phys. Chem. B*, 1999, **103**, 9533–9539.
- 73 X. Dong, X. Ji, H. Wu, L. Zhao, J. Li and W. Yang, *J. Phys. Chem. C*, 2009, **113**, 6573–6576.
- 74 M. Chen, Y. G. Feng, X. Wang, T. C. Li, J. Y. Zhang and D. J. Qian, *Langmuir*, 2007, **23**, 5296–5304.
- 75 Y. Sun and Y. Xia, *Science*, 2002, **298**, 2176–2179.
- 76 Y. Sun and Y. Xia, *Adv. Mater.*, 2002, **14**, 833–837.
- 77 R. Jin, *Nanoscale*, 2010, **2**, 343–362.
- 78 Y. Lu and W. Chen, *Chem. Soc. Rev.*, 2012, **41**, 3594–3623.
- 79 O. Varnavski, G. Ramakrishna, J. Kim, D. Lee and T. Goodson, *J. Am. Chem. Soc.*, 2010, **132**, 16–17.
- 80 H. Häkkinen, *Nat. Chem.*, 2012, **4**, 443–455.
- 81 Y. Li, G. Galli and F. Gygi, *ACS Nano*, 2008, **2**, 1896–1902.
- 82 L. Shang, S. Dong and G. U. Nienhaus, *Nano Today*, 2011, **6**, 401–418.
- 83 Y. Yu, Q. Yao, Z. Luo, X. Yuan, J. Y. Lee and J. Xie, *Nanoscale*, 2013, **5**, 4606–20.
- 84 S. Chen, R. S. Ingram, M. J. Hostetler, J. J. Pietron, R. W. Murray, T. G. Schaaff, J. T. Khoury, M. M. Alvarez and R. L. Whetten, *Science (80)*, 1998, **280**, 2098–2101.
- 85 W. Chen and S. Chen, *Angew. Chemie - Int. Ed.*, 2009, **48**, 4386–4389.
- 86 Y. Liu, H. Tsunoyama, T. Akita and T. Tsukuda, *Chem. Commun.*, 2010, **46**, 550–2.
- 87 Y. Liu, H. Tsunoyama, T. Akita, S. Xie and T. Tsukuda, *ACS Catal.*, 2011, **1**, 2–6.
- 88 G. Ramakrishna, O. Varnavski, J. Kim, D. Lee and T. Goodson, *J. Am. Chem. Soc.*, 2008, **130**, 5032–5033.
- 89 M. A. Habeeb Muhammed, A. K. Shaw, S. K. Pal and T. Pradeep, *J. Phys. Chem. C*, 2008, **112**, 14324–14330.
- 90 Z. Wu and R. Jin, *Nano Lett.*, 2010, **10**, 2568–2573.
- 91 S. Link, A. Beeby, S. FitzGerald, M. A. El-Sayed, T. G. Schaaff and R. L. Whetten, *J. Phys. Chem. B*, 2002, **106**, 3410–3415.

- 92 Y. Negishi, Y. Takasugi, S. Sato, H. Yao, K. Kimura and T. Tsukuda, *J. Am. Chem. Soc.*, 2004, **126**, 6518–6519.
- 93 Y. Negishi, K. Nobusada and T. Tsukuda, *J. Am. Chem. Soc.*, 2005, **127**, 5261–5270.
- 94 T. Huang and R. W. Murray, *J. Phys. Chem. B*, 2001, **105**, 12498–12502.
- 95 D. Lee, R. L. Donkers, G. Wang, A. S. Harper and R. W. Murray, *J. Am. Chem. Soc.*, 2004, **126**, 6193–6199.
- 96 M. C. Paau, C. K. Lo, X. Yang and M. M. F. Choi, *J. Phys. Chem. C*, 2010, **114**, 15995–16003.
- 97 J. Zheng and R. M. Dickson, *J. Am. Chem. Soc.*, 2002, **124**, 13982–13983.
- 98 J. Zheng, J. T. Petty and R. M. Dickson, *J. Am. Chem. Soc.*, 2003, **125**, 7780–7781.
- 99 J. T. Petty, J. Zheng, N. V. Hud and R. M. Dickson, *J. Am. Chem. Soc.*, 2004, **126**, 5207–5212.
- 100 H. C. Yeh, J. Sharma, J. J. Han, J. S. Martinez and J. H. Werner, *Nano Lett.*, 2010, **10**, 3106–3110.
- 101 J. Yu, S. A. Patel and R. M. Dickson, *Angew. Chemie - Int. Ed.*, 2007, **46**, 2028–2030.
- 102 B. Adhikari and A. Banerjee, *Chemistry*, 2010, **16**, 13698–705.
- 103 A. Ono, M. Kikawada, R. Akimoto, W. Inami and Y. Kawata, *Opt. Express*, 2013, **21**, 17447.
- 104 G. Maidecchi, G. Gonella, R. Proietti Zaccaria, R. Moroni, L. Anghinolfi, A. Giglia, S. Nannarone, L. Mattera, H. L. Dai, M. Canepa and F. Bisio, *ACS Nano*, 2013, **7**, 5834–5841.
- 105 Y. Ekinici, H. H. Solak and J. F. Löffler, *J. Appl. Phys.*, 2008, **104**.
- 106 M. W. Knight, L. Liu, Y. Wang, L. Brown, S. Mukherjee, N. S. King, H. O. Everitt, P. Nordlander and N. J. Halas, *Nano Lett.*, 2012, **12**, 6000–6004.
- 107 P. G. Etchegoin, E. C. Le Ru and M. Meyer, *J. Chem. Phys.*, 2006, **125**, 164705.
- 108 M. W. Knight, N. S. King, L. Liu, H. O. Everitt, P. Nordlander and N. J. Halas, *ACS Nano*, 2014, **8**, 834–840.
- 109 S. K. Jha, Z. Ahmed, M. Agio, Y. Ekinici and J. F. Löffler, *J. Am. Chem. Soc.*, 2012, **134**, 1966–1969.
- 110 M. H. Chowdhury, K. Ray, S. K. Gray, J. Pond and J. R. Lakowicz, *Proc. Soc. PhotoOptical Instrum. Eng.*, 2010, 7577, 75770O.
- 111 K. Ray, H. Szmecinski and J. R. Lakowicz, *Anal. Chem.*, 2009, **81**, 6049–6054.
- 112 S. K. Ghosh and T. Pal, *Chem. Rev.*, 2007, **107**, 4797–4862.
- 113 R. Liu, R. Liew, J. Zhou and B. Xing, *Angew. Chemie*, 2007, **119**, 8955–8959.

- 114 N. Nath and A. Chilkoti, *Anal. Chem.*, 2002, **74**, 504–509.
- 115 J. Liu and Y. Lu, *J. Am. Chem. Soc.*, 2003, **125**, 6642–6643.
- 116 L. Dykman and N. Khlebtsov, *Chem. Soc. Rev.*, 2012, **41**, 2256–2282.
- 117 C. a Mirkin, R. L. Letsinger, R. C. Mucic and J. J. Storhoff, *Nature*, 1996, **382**, 607–609.
- 118 T. M. H. Lee, *Sensors*, 2008, **8**, 5535–5559.
- 119 N. T. Kim Thanh and Z. Rosenzweig, *Anal. Chem.*, 2002, **74**, 1624–1628.
- 120 L. R. Hirsch, J. B. Jackson, A. Lee, N. J. Halas and J. L. West, *Anal. Chem.*, 2003, **75**, 2377–2381.
- 121 K. A. Willets and R. P. Van Duyne, *Annu. Rev. Phys. Chem.*, 2007, **58**, 267–297.
- 122 J. G. Gordon and S. Ernst, *Surf. Sci.*, 1980, **101**, 499–506.
- 123 C. Nylander, B. Liedberg and T. Lind, *Sensors and Actuators*, 1982, **3**, 79–88.
- 124 J. Homola, *Chem. Rev.*, 2008, **108**, 462–493.
- 125 J. Ye, K. Bonroy, D. Nelis, F. Frederix, J. D’Haen, G. Maes and G. Borghs, *Colloids Surfaces A Physicochem. Eng. Asp.*, 2008, **321**, 313–317.
- 126 N. Verellen, P. Van Dorpe, C. Huang, K. Lodewijks, G. A. E. Vandenbosch, L. Lagae and V. V. Moshchalkov, *Nano Lett.*, 2011, **11**, 391–397.
- 127 A. G. Brolo, R. Gordon, B. Leathem and K. L. Kavanagh, *Langmuir*, 2004, **20**, 4813–4815.
- 128 A. V Whitney, J. W. Elam, S. Zou, A. V Zinovev, P. C. Stair, G. C. Schatz and R. P. Van Duyne, *J. Phys. Chem. B*, 2005, **109**, 20522–20528.
- 129 P. Englebienne, *Analyst*, 1998, **123**, 1599–1603.
- 130 P. Englebienne, M. Verhas and A. Van Hoonacker, *Analyst*, 2001, **126**, 1645–1651.
- 131 E. Smith and G. Dent, *Modern Raman Spectroscopy - A Practical Approach*, John Wiler & Sons, New York, 2005.
- 132 K. Kneipp, H. Kneipp, I. Itzkan, R. R. Dasari and M. S. Feld, *Chem. Rev.*, 1999, **99**, 2957–2976.
- 133 M. J. Banholzer, J. E. Millstone, L. Qin and C. a Mirkin, *Chem. Soc. Rev.*, 2008, **37**, 885–897.
- 134 X. X. Han, B. Zhao and Y. Ozaki, *Anal. Bioanal. Chem.*, 2009, **394**, 1719–1727.
- 135 K. Kneipp, H. Kneipp and J. Kneipp, *Acc. Chem. Res.*, 2006, **39**, 443–450.
- 136 W. E. Doering and S. Nie, *J. Phys. Chem. B*, 2002, **106**, 311–317.
- 137 P. G. Etchegoin and E. C. Le Ru, *Phys. Chem. Chem. Phys.*, 2008, **10**, 6079–89.
- 138 H. Xu, E. Bjerneld, M. Käll and L. Börjesson, *Phys. Rev. Lett.*, 1999, **83**, 4357–

- 4360.
- 139 B. N. J. Persson, *Chem. Phys. Lett.*, 1981, **82**, 561–565.
- 140 A. Otto, *J. Raman Spectrosc.*, 2005, **36**, 497–509.
- 141 R. Thompson, in *Fluorescence sensors and biosensors*, CRC press, Boca Raton, FL, 2005, p. 377.
- 142 K. Aslan, I. Gryczynski, J. Malicka, E. Matveeva, J. R. Lakowicz and C. D. Geddes, *Curr. Opin. Biotechnol.*, 2005, **16**, 55–62.
- 143 X. Kong, E. Nir, K. Hamadani and S. Weiss, *J. Am. Chem. Soc.*, 2007, **129**, 4643–4654.
- 144 V. L. Mosiman, B. K. Patterson, L. Canterero and C. L. Goolsby, *Commun. Clin. Cytom.*, 1997, **30**, 151–156.
- 145 E. Dulkeith, A. C. Morteani, T. Niedereichholz, T. A. Klar, J. Feldmann, S. A. Levi, F. C. J. M. van Veggel, D. N. Reinhoudt, M. Möller and D. I. Gittins, *Phys. Rev. Lett.*, 2002, **89**, 203002.
- 146 J. Gersten and A. Nitzan, *J. Chem. Phys.*, 1981, **75**, 1139–1152.
- 147 E. A. Jares-Erijman and T. M. Jovin, *Nat Biotechnol*, 2003, **21**, 1387–1395.
- 148 T. L. Jennings, M. P. Singh and G. F. Strouse, *J. Am. Chem. Soc.*, 2006, **128**, 5462–5467.
- 149 C. C. Huang and H. T. Chang, *Anal. Chem.*, 2006, **78**, 8332–8338.
- 150 B.-C. Ye and B.-C. Yin, *Angew. Chemie Int. Ed.*, 2008, **47**, 8386–8389.
- 151 E. Oh, M.-Y. Hong, D. Lee, S.-H. Nam, H. C. Yoon and H.-S. Kim, *J. Am. Chem. Soc.*, 2005, **127**, 3270–3271.
- 152 Y. P. Kim, Y. H. Oh, E. Oh, S. Ko, M. K. Han and H. S. Kim, *Anal. Chem.*, 2008, **80**, 4634–4641.
- 153 M. Li, Q. Wang, X. Shi, L. A. Hornak and N. Wu, *Anal. Chem.*, 2011, **83**, 7061–7065.
- 154 J. M. Liu, J. T. Chen and X. P. Yan, *Anal. Chem.*, 2013, **85**, 3238–3245.
- 155 J.-L. Ma, B.-C. Yin, H.-N. Le and B.-C. Ye, *ACS Appl. Mater. Interfaces*, 2015, **7**, 12856–12863.
- 156 S. Lukman, K. M. M. Aung, J. Liu, B. Liu and X. Su, *ACS Appl. Mater. Interfaces*, 2013, **5**, 12725–12734.
- 157 S. Lukman, K. M. Moh Aung, M. G. Liang Lim, S. Hong, S. K. Tan, E. Cheung and X. Su, *RSC Adv.*, 2014, **4**, 8883.
- 158 X. He, H. Liu, Y. Li, S. Wang, Y. Li, N. Wang, J. Xiao, X. Xu and D. Zhu, *Adv. Mater.*, 2005, **17**, 2811–2815.
- 159 N. Zhang, Y. Liu, L. Tong, K. Xu, L. Zhuo and B. Tang, *Analyst*, 2008, **133**, 1176–1181.

- 160 J.-H. Lin, C.-W. Chang and W.-L. Tseng, *Analyst*, 2010, **135**, 104–110.
- 161 M. De, S. Rana, H. Akpınar, O. R. Miranda, R. R. Arvizo, U. H. F. Bunz and V. M. Rotello, *Nat. Chem.*, 2009, **1**, 461–465.
- 162 R. L. Phillips, O. R. Miranda, C.-C. You, V. M. Rotello and U. H. F. Bunz, *Angew. Chemie, Int. Ed.*, 2008, **47**, 2590–2594.
- 163 B. Dubertret, M. Calame and a J. Libchaber, *Nat. Biotechnol.*, 2001, **19**, 365–70.
- 164 P. C. Ray, A. Fortner and G. K. Darbha, *J. Phys. Chem. B*, 2006, **110**, 20745–8.
- 165 R. Bardhan, N. K. Grady, J. R. Cole, A. Joshi and N. J. Halas, *ACS Nano*, 2009, **3**, 744–752.
- 166 Y. Fu, J. Zhang and J. R. Lakowicz, *J. Am. Chem. Soc.*, 2010, **132**, 5540–5541.
- 167 D. Nepal, L. F. Drummy, S. Biswas, K. Park and R. A. Vaia, *ACS Nano*, 2013, **7**, 9064–9074.
- 168 N. S. Abadeer, M. R. Brennan, W. L. Wilson and C. J. Murphy, *ACS Nano*, 2014, **8**, 8392–8406.
- 169 N. Gandra, C. Portz, L. Tian, R. Tang, B. Xu, S. Achilefu and S. Singamaneni, *Angew. Chemie - Int. Ed.*, 2014, **53**, 866–870.
- 170 C. D. Geddes and J. R. Lakowicz, *J. Fluoresc.*, 2002, **12**, 121–129.
- 171 K. Aslan, S. N. Malyn and C. D. Geddes, *J. Fluoresc.*, 2007, **17**, 7–13.
- 172 F. Xie, M. S. Baker and E. M. Goldys, *Chem. Mater.*, 2008, **20**, 1788–1797.
- 173 Y. Cheng, T. Stakenborg, P. Van Dorpe, L. Lagae, M. Wang, H. Chen and G. Borghs, *Anal. Chem.*, 2011, **83**, 1307–1314.
- 174 S. H. Lee, S. M. Wabaidur, Z. A. Allothman and S. M. Alam, *Luminescence*, 2011, **26**, 768–773.
- 175 W. Pompe, G. Rödel, H.-J. Weiss and M. Mertig, *Bio-Nanomaterials: Designing Materials Inspired by Nature*, WILEY-VCH Verlag, Weinheim, Germany, 2013.
- 176 W. Shenton, S. A. Davis and S. Mann, *Adv. Mater.*, 1999, **11**, 449–452.
- 177 R. de la Rica, D. Aili and M. M. Stevens, *Adv. Drug Deliv. Rev.*, 2012, **64**, 967–978.
- 178 W. Wang, T. Yan, S. Cui and J. Wan, *Chem. Commun.*, 2012, **48**, 10228–10230.
- 179 W. Wang, N. Zhao, X. Li, J. Wan and X. Luo, *Analyst*, 2015, **140**, 1672–1677.
- 180 X. Xu, J. Zhang, F. Yang and X. Yang, *Chem. Commun. (Camb.)*, 2011, **47**, 9435–9437.
- 181 S. Bi, Y. Yan, S. Hao and S. Zhang, *Angew. Chemie - Int. Ed.*, 2010, **49**, 4438–4442.
- 182 D. F. Swinehart, *J. Chem. Educ.*, 1962, **39**, 333.

-
- 183 J. Kacher, C. Landon, B. L. Adams and D. Fullwood, *Ultramicroscopy*, 2009, **109**, 1148–1156.
- 184 L. Reimer and H. Kohl, *Transmission Electron Microscopy Physics of Image Formation*, Springer -, 2008, vol. 51.
- 185 C. A. Angell, *Annu. Rev. Phys. Chem.*, 2004, **55**, 559–583.
- 186 J. T. Edward, *J. Chem. Educ.*, 1970, **47**, 261.
- 187 J. D. Clogston and A. K. Patri, in *Characterization of Nanoparticles Intended for Drug Delivery*, ed. E. S. McNeil, Humana Press, Totowa, NJ, 2011, pp. 63–70.
- 188 British standards institution, in *BS 188:1977*.
- 189 A. Guerrero-Martínez, M. Grzelczak and L. M. Liz-Marzán, *ACS Nano*, 2012, **6**, 3655–3662.
- 190 S. Nauert, A. Paul, Y. R. Zhen, D. Solis, L. Vigderman, W. S. Chang, E. R. Zubarev, P. Nordlander and S. Link, *ACS Nano*, 2014, **8**, 572–580.
- 191 L. Vigderman and E. R. Zubarev, *Langmuir*, 2012, **28**, 9034–9040.
- 192 X. Huang, P. K. Jain, I. H. El-Sayed and M. A. El-Sayed, *Lasers Med. Sci.*, 2008, **23**, 217–228.
- 193 L. C. Kennedy, L. R. Bickford, N. A. Lewinski, A. J. Coughlin, Y. Hu, E. S. Day, J. L. West and R. A. Drezek, *Small*, 2011, **7**, 169–183.
- 194 X. Huang, S. Neretina and M. A. El-Sayed, *Adv. Mater.*, 2009, **21**, 4880–4910.
- 195 T. B. Huff, L. Tong, Y. Zhao, M. N. Hansen, J.-X. Cheng and A. Wei, *Nanomedicine*, 2007, **2**, 125–32.
- 196 A. M. Alkilany, L. B. Thompson, S. P. Boulos, P. N. Sisco and C. J. Murphy, *Adv. Drug Deliv. Rev.*, 2012, **64**, 190–199.
- 197 C. Kim, C. Favazza and L. V Wang, *Chem. Rev.*, 2010, **110**, 2756–2782.
- 198 A. S. Stender, K. Marchuk, C. Liu, S. Sander, M. W. Meyer, E. A. Smith, B. Neupane, G. Wang, J. Li, J.-X. Cheng, B. Huang and N. Fang, *Chem. Rev.*, 2013, **113**, 2469–2527.
- 199 H. Wang, T. B. Huff, D. a Zweifel, W. He, P. S. Low, A. Wei and J.-X. Cheng, *Proc. Natl. Acad. Sci. U. S. A.*, 2005, **102**, 15752–15756.
- 200 L. Vigderman, B. P. Khanal and E. R. Zubarev, *Adv. Mater.*, 2012, **24**, 4811–4841.
- 201 R. M. Pallares, S. L. Kong, T. H. Ru, N. T. K. Thanh, Y. Lu and X. Su, *Chem. Commun.*, 2015, **51**, 14524–14527.
- 202 M. E. Stewart, C. R. Anderton, L. B. Thompson, J. Maria, S. K. Gray, J. A. Rogers and R. G. Nuzzo, *Chem. Rev.*, 2008, **108**, 494–521.
- 203 N. R. Jana, L. Gearheart and C. J. Murphy, *J. Phys. Chem. B*, 2001, **105**, 4065–4067.

- 204 M. Liu and P. Guyot-Sionnest, *J. Phys. Chem. B*, 2005, **109**, 22192–22200.
- 205 D. K. Smith and B. A. Korgel, *Langmuir*, 2008, **24**, 644–649.
- 206 S. E. Lohse, N. D. Burrows, L. Scarabelli, L. M. Liz-Marzán and C. J. Murphy, *Chem. Mater.*, 2014, **26**, 34–43.
- 207 S. Si, C. Leduc, M. H. Delville and B. Lounis, *ChemPhysChem*, 2012, **13**, 193–202.
- 208 K. C. Ng and W. Cheng, *Nanotechnology*, 2012, **23**, 105602.
- 209 J. Pérez-Juste, L. M. Liz-Marzán, S. Carnie, D. Y. C. Chan and P. Mulvaney, *Adv. Funct. Mater.*, 2004, **14**, 571–579.
- 210 C. A. Dreiss, *Soft Matter*, 2007, **3**, 956–970.
- 211 S. Kumar, A. Z. Naqvi and Kabir-ud-Din, *Langmuir*, 2000, **16**, 5252–5256.
- 212 L. Abezgauz, K. Kuperkar, P. A. Hassan, O. Ramon, P. Bahadur and D. Danino, *J. Colloid Interface Sci.*, 2010, **342**, 83–92.
- 213 M. G. Cacace, E. M. Landau and J. J. Ramsden, *Q. Rev. Biophys.*, 1997, **30**, 241–277.
- 214 X. C. Jiang and M. P. Pileni, *Colloids Surfaces A Physicochem. Eng. Asp.*, 2007, **295**, 228–232.
- 215 T. Zhang, A. Jiang, J. H. Harrison and S. Chen, *J. Chem. Technol. Biotechnol.*, 2012, **87**, 1098–1103.
- 216 O. R. Miranda, N. R. Dollahon and T. S. Ahmadi, *Cryst. Growth Des.*, 2006, **6**, 2747–2753.
- 217 T. K. Sau and C. J. Murphy, *Langmuir*, 2004, **20**, 6414–6420.
- 218 R. C. Wadams, L. Fabris, R. A. Vaia and K. Park, *Chem. Mater.*, 2013, **25**, 4772–4780.
- 219 Y. Zhang and P. S. Cremer, *Curr. Opin. Chem. Biol.*, 2006, **10**, 658–663.
- 220 M. J. Nicol, C. a Fleming and R. L. Paul, *Extr. Metall. gold*, 1992, 831–905.
- 221 A. L. Underwood and E. W. Anacker, *J. Colloid Interface Sci.*, 1987, **117**, 242–250.
- 222 A. B. Shah, S. T. Sivapalan, B. M. Devetter, T. K. Yang, J. Wen, R. Bhargava, C. J. Murphy and J. M. Zuo, *Nano Lett.*, 2013, **13**, 1840–1846.
- 223 H.-W. Wang, C.-F. Shieh, H.-Y. Chen, W.-C. Shiu, B. Russo and G. Cao, *Nanotechnology*, 2006, **17**, 2689–2694.
- 224 R. Kumar and S. R. Raghavan, *Soft Matter*, 2009, **5**, 797–803.
- 225 K.-T. Yong, Y. Sahoo, M. T. Swihart, P. M. Schneeberger and P. N. Prasad, *Top. Catal.*, 2008, **47**, 49–60.
- 226 K. Kuperkar, L. Abezgauz, K. Prasad and P. Bahadur, *J. Surfactants Deterg.*, 2010, **13**, 293–303.

- 227 E. C. Dreaden, A. M. Alkilany, X. Huang, C. J. Murphy and M. a. El-Sayed, *Chem. Soc. Rev.*, 2012, **41**, 2740.
- 228 S. E. Lohse and C. J. Murphy, *Chem. Mater.*, 2013, **25**, 1250–1261.
- 229 M. E. Helgeson, T. K. Hodgdon, E. W. Kaler and N. J. Wagner, *J. Colloid Interface Sci.*, 2010, **349**, 1–12.
- 230 K. Kuperkar, L. Abezgauz, D. Danino, G. Verma, P. A. Hassan, V. K. Aswal, D. Varade and P. Bahadur, *J. Colloid Interface Sci.*, 2008, **323**, 403–409.
- 231 M. R. Langille, M. L. Personick, J. Zhang and C. A. Mirkin, *J. Am. Chem. Soc.*, 2012, **134**, 14542–14554.
- 232 J. Rodríguez-Fernández, J. Pérez-Juste, P. Mulvaney and L. M. Liz-Marzán, *J. Phys. Chem. B*, 2005, **109**, 14257–14261.
- 233 M. Eguchi, D. Mitsui, H. L. Wu, R. Sato and T. Teranishi, *Langmuir*, 2012, **28**, 9021–9026.
- 234 A. J. Bard, R. Parsons and J. Jordan, *Standard potentials in aqueous solution*, Marcel Dekker, New York, 1985.
- 235 L. S. Brown and T. Holme, *Chemistry for Engineering Students*, Brooks/Cole, Belmont, CA, 2011.
- 236 O. M. Magnussen, *Chem. Rev.*, 2002, **102**, 679–726.
- 237 D. K. Smith, N. R. Miller and B. A. Korgel, *Langmuir*, 2009, **25**, 9518–9524.
- 238 J. Sylvestre, S. Poulin, A. V Kabashin, E. Sacher, M. Meunier, J. H. T. Luong, Ä. P. De Montre and C. Postale, *J. Phys. Chem. B*, 2004, **108**, 16864–16869.
- 239 C. Yu and J. Irudayaraj, *Anal. Chem.*, 2007, **79**, 572–579.
- 240 M. A. El-Sayed, *Acc. Chem. Res.*, 2001, **34**, 257–264.
- 241 C. G. Khoury and T. Vo-Dinh, *J. Phys. Chem. C*, 2008, **112**, 18849–18859.
- 242 J. L. West and N. J. Halas, *Curr. Opin. Biotechnol.*, 2000, **11**, 215–217.
- 243 C. Loo, L. Hirsch, M.-H. Lee, E. Chang, J. West, N. Halas and R. Drezek, *Opt. Lett.*, 2005, **30**, 1012–1014.
- 244 S. S. Shankar, A. Rai, B. Ankamwar, A. Singh, A. Ahmad and M. Sastry, *Nat. Mater.*, 2004, **3**, 482–8.
- 245 S. P. Chandran, M. Chaudhary, R. Pasricha, A. Ahmad and M. Sastry, *Biotechnol. Prog.*, 2006, **22**, 577–583.
- 246 W. Ahmed, C. Glass and J. M. van Ruitenbeek, *Nanoscale*, 2014, **6**, 13222–7.
- 247 M. Grzelczak, J. Pérez-Juste, P. Mulvaney and L. M. Liz-Marzán, *Chem. Soc. Rev.*, 2008, **37**, 1783–1791.
- 248 Z. Chu, C. a Dreiss and Y. Feng, *Chem. Soc. Rev.*, 2013, **42**, 7174–203.
- 249 Y. Feng, Z. Chu and C. A. Dreiss, in *Smart Wormlike Micelles*, Springer Berlin Heidelberg, Berlin, Heidelberg, 2015, pp. 29–40.

- 250 H. Sakai, Y. Orihara, H. Kodashima, A. Matsumura, T. Ohkubo, K. Tsuchiya and M. Abe, *J. Am. Chem. Soc.*, 2005, **127**, 13454–13455.
- 251 A. M. Ketner, R. Kumar, T. S. Davies, P. W. Elder and S. R. Raghavan, *J. Am. Chem. Soc.*, 2007, **129**, 1553–1559.
- 252 F. Kim, J. H. Song and P. Yang, *J. Am. Chem. Soc.*, 2002, **124**, 14316–14317.
- 253 O. R. Miranda and T. S. Ahmadi, *J. Phys. Chem. B*, 2005, **109**, 15724–34.
- 254 Y. Niidome, K. Nishioka, H. Kawasaki and S. Yamada, *Chem. Commun.*, 2003, 2376–2377.
- 255 R. Elghanian, J. J. Storhoff, R. C. Mucic, R. L. Letsinger and C. A. Mirkin, *Science (80)*, 1997, **277**, 1078–1081.
- 256 J. S. Lee, M. S. Han and C. A. Mirkin, *Angew. Chemie - Int. Ed.*, 2007, **46**, 4093–4096.
- 257 J. Liu and Y. Lu, *Nat. Protoc.*, 2006, **1**, 246–252.
- 258 X. Su and R. Kanjanawarut, *ACS Nano*, 2009, **3**, 2751–2759.
- 259 R. Kanjanawarut and X. Su, *Anal. Chem.*, 2009, **81**, 6122–6129.
- 260 R. de la Rica and M. M. Stevens, *Nat. Nanotechnol.*, 2012, **8**, 1759–1764.
- 261 D. Cecchin, R. de la Rica, R. E. S. Bain, M. W. Finnis, M. M. Stevens and G. Battaglia, *Nanoscale*, 2014, **6**, 9559–9562.
- 262 X. M. Nie, R. Huang, C. X. Dong, L. J. Tang, R. Gui and J. H. Jiang, *Biosens. Bioelectron.*, 2014, **58**, 314–319.
- 263 M. Coronado-Puchau, L. Saa, M. Grzelczak, V. Pavlov and L. M. Liz-Marzán, *Nano Today*, 2013, **8**, 461–468.
- 264 G. A. Mansoori, P. Mohazzabi, P. McCormack and S. Jabbari, *World Rev. Sci. Technol. Sustain. Dev.*, 2007, **4**, 226–257.
- 265 R. M. Lucas, *Eye Contact Lens*, 2011, **37**, 168–75.
- 266 P. M. Farr, J. E. Besag and B. L. Diffey, *J. Invest. Dermatol.*, 1988, **91**, 454–457.
- 267 A. R. Young, *Pigment Cell Res.*, 2004, **17**, 2–9.
- 268 Y. Matsumura and H. N. Ananthaswamy, *Expert Rev Mol Med*, 2002, **4**, 1–22.
- 269 A. A. Vink and L. Roza, *J. Photochem. Photobiol. B Biol.*, 2001, **65**, 101–104.
- 270 T. D. Thacher and B. L. Clarke, *Mayo Clin. Proc.*, 2011, **86**, 50–60.
- 271 ASTM International, *Stand. Tables Ref. Sol. Spectr. Irradiances Direct Norm. Hemispherical 37° Tilted Surf.*, 2012.
- 272 K. A. Rawat and S. K. Kailasa, *Sensors Actuators B Chem.*, 2016, **222**, 780–789.
- 273 B. S. B. Kasibabu, J. R. Bhamore, S. L. D'souza and S. K. Kailasa, *RSC Adv.*, 2015, **5**, 39182–39191.
- 274 K. A. Rawat and S. K. Kailasa, *RSC Adv.*, 2016, **6**, 11099–11108.

- 275 K. A. Rawat and S. K. Kailasa, *Microchim. Acta*, 2014, **181**, 1917–1929.
- 276 G. V. N. Rao, in *Advanced x-ray techniques in research and industry*, ed. A. K. Singh, IOS Press, Amsterdam, 2005, p. 562.
- 277 G. R. Bors, W.; Buettner, in *Vitamin C in health and disease*, ed. L. Packer, Marcel Dekker, Inc, New York, 1997, pp. 75–94.
- 278 Q. Wei, J. Ji and J. Shen, *J. Nanosci. Nanotechnol.*, 2008, **8**, 5708–5714.
- 279 Y. G. Kim, S. K. Oh and R. M. Crooks, *Chem. Mater.*, 2004, **16**, 167–172.
- 280 C. Giacomelli, K. Ckless, D. Galato, F. S. Miranda and A. Spinelli, *J. Braz. Chem. Soc.*, 2002, **13**, 332–338.
- 281 R. Amorati, G. F. Pedulli, L. Cabrini, L. Zambonin and L. Landi, *J. Agric. Food Chem.*, 2006, **54**, 2932–2937.
- 282 E. de S. Gil, T. A. Enache and A. M. Oliveira-Brett, *Comb. Chem. High Throughput Screen.*, 2013, **16**, 92–97.
- 283 B. C. Smith, *Infrared spectral interpretation: a systematic approach*, CRC press, Boca Raton, FL, 1998.
- 284 V. Arjunan, R. Anitha, S. Thenmozhi, M. K. Marchewka and S. Mohan, *J. Mol. Struct.*, 2016, **1113**, 42–54.
- 285 V. Arjunan, R. Anitha, M. K. Marchewka, S. Mohan and H. Yang, *J. Mol. Struct.*, 2015, **1080**, 122–136.
- 286 S. D. M. Allen, M. J. Almond, J. L. Bruneel, A. Gilbert, P. Hollins and J. Mascetti, *Spectrochim. Acta - Part A Mol. Biomol. Spectrosc.*, 2000, **56**, 2423–2430.
- 287 K. Hanai, A. Kuwae, T. Takai, H. Senda and K. K. Kunimoto, *Spectrochim. Acta - Part A Mol. Biomol. Spectrosc.*, 2001, **57**, 513–519.
- 288 Haynes W. M., *CRC Handbook of Chemistry and Physics*, CRC press: Boca Raton, 93rd Editi., 2006.
- 289 Z. Grodzińska-Zachwieja, *J. Chromatogr. A*, 1982, **241**, 217–222.
- 290 C. L. Yaws, *The Yaws Handbook of Physical Properties for Hydrocarbons and Chemicals: Physical Properties for More Than 41,000 Organic and Inorganic Chemical Compounds*, Gulf Publishing Company, Houston, 2005.
- 291 C. Sandris, *Tetrahedron*, 1968, **24**, 3569–3582.
- 292 M. M. T. Khan and a. E. Martell, *J. Am. Chem. Soc.*, 1967, **89**, 4176–4185.
- 293 M. M. T. Khan and A. E. Martell, *J. Am. Chem. Soc.*, 1969, **91**, 4668–4672.
- 294 G. Gramlich, J. Zhang and W. M. Nau, *J. Am. Chem. Soc.*, 2002, **124**, 11252–11253.
- 295 C. Makote, R. D.; Chatterjee, *Indian J. Chem. Sect. A*, 1999, **38**, 783–791.
- 296 D. Njus, V. Jalukar, J. Zu and P. M. Kelley, *Am. J. Clin. Nutr.*, 1991, **54**.
- 297 M. Friedman and H. S. Jürgens, *J. Agric. Food Chem.*, 2000, **48**, 2101–2110.

- 298 M. Vairamani, M. Saraswathi and G. K. V. Rao, *Org. Mass Spectrom.*, 1990, **25**, 274–276.
- 299 K. A. Connors and J. M. Lipari, *J. Pharm. Sci.*, 1976, **65**, 379–383.
- 300 B. . Lucas, R.; McMichael, T.; Smith, W.; Armstrong, Geneva, 2006, pp. 4–5.
- 301 S. Madronich, R. L. McKenzie, L. O. Björn and M. M. Caldwell, *J. Photochem. Photobiol. B Biol.*, 1998, **46**, 5–19.
- 302 R. McKenzie, D. Smale and M. Kotkamp, *Photochem. Photobiol. Sci.*, 2004, **3**, 252–256.
- 303 A. Heidenreich, G. Aus, M. Bolla, S. Joniau, V. B. Matveev, H. P. Schmid and F. Zattoni, *Eur. Urol.*, 2008, **53**, 68–80.
- 304 G. Ploussard and A. de la Taille, *Nat. Rev. Urol.*, 2010, **7**, 101–109.
- 305 S. Hu, J. A. Loo and D. T. Wong, *Proteomics*, 2006, **6**, 6326–6353.
- 306 E. R. Sauter, W. Zhu, X.-J. Fan, R. P. Wassell, I. Chervoneva and G. C. Du Bois, *Br. J. Cancer*, 2002, **86**, 1440–1443.
- 307 I. M. Thompson, D. K. Pauler, P. J. Goodman, C. M. Tangen, M. S. Lucia, H. L. Parnes, L. M. Minasian, L. G. Ford, S. M. Lippman, E. D. Crawford, J. J. Crowley and C. a Coltman, *N. Engl. J. Med.*, 2004, **350**, 2239–2246.
- 308 J. R. Prensner, M. A. Rubin, J. T. Wei and A. M. Chinnaiyan, *Sci. Transl. Med.*, 2012, **4**, 127rv3.
- 309 S. Holdenrieder, P. Stieber, L. Y. S. Chan, S. Geiger, A. Kremer, D. Nagel and Y. M. D. Lo, *Clin. Chem.*, 2005, **51**, 1544–1546.
- 310 D. L. Peters and P. J. Pretorius, *Clin. Chim. Acta*, 2011, **412**, 806–811.
- 311 P. B. Gahan and M. Stroun, *Cell Biochem. Funct.*, 2010, **28**, 529–538.
- 312 H. D. Halicka, E. Bedner and Z. Darzynkiewicz, *Exp. Cell Res.*, 2000, **260**, 248–256.
- 313 V. Swarup and M. R. Rajeswari, *FEBS Lett.*, 2007, **581**, 795–799.
- 314 T. L. Wu, D. Zhang, J. H. Chia, K. C. Tsao, C. F. Sun and J. T. Wu, *Clin. Chim. Acta*, 2002, **321**, 77–87.
- 315 A. K. Pathak, M. Bhutani, S. Kumar, A. Mohan and R. Guleria, *Clin. Chem.*, 2006, **52**, 1833–1842.
- 316 R. de la Rica and M. M. Stevens, *Nat. Nanotechnol.*, 2012, **8**, 1759–1764.
- 317 W. C. Law, K. T. Yong, A. Baev and P. N. Prasad, *ACS Nano*, 2011, **5**, 4858–4864.
- 318 A. Barik, L. M. Otto, D. Yoo, J. Jose, T. W. Johnson and S. H. Oh, *Nano Lett.*, 2014, **14**, 2006–2012.
- 319 L. Rodríguez-Lorenzo, R. de la Rica, R. a. Álvarez-Puebla, L. M. Liz-Marzán and M. M. Stevens, *Nat. Mater.*, 2012, **11**, 604–607.

- 320 L. G. Lee, C. H. Chen and L. a Chiu, *Cytometry*, 1986, **7**, 508–17.
- 321 G. Kawamura, Y. Yang and M. Nogami, *J. Phys. Chem. C*, 2008, **112**, 10632–10636.
- 322 Z. Ma, L. Tian, T. Wang and C. Wang, *Anal. Chim. Acta*, 2010, **673**, 179–184.
- 323 X.-J. Zheng, J.-D. Qiu, L. Zhang, Z.-X. Wang and R.-P. Liang, *Chem. Commun.*, 2013, **49**, 3546–8.
- 324 R. Kanjanawarut and X. Su, *Biointerphases*, 2010, **5**, FA98–A104.
- 325 R. Kanjanawarut, B. Yuan and X. D. Su, *Nucleic Acid Ther.*, 2013, **23**, 273–280.
- 326 S. Jahr, H. Hentze, S. Englisch, D. Hardt, F. O. Fackelmayer, R.-D. Hesch and R. Knippers, *Cancer Res.*, 2001, **61**, 1659–1665.
- 327 Qiagen, *Qiagene Protoc.*, 2012, 72.
- 328 T. E. Skvortsova, E. Y. Rykova, S. N. Tamkovich, O. E. Bryzgunova, a V Starikov, N. P. Kuznetsova, V. V Vlassov and P. P. Laktionov, *Br. J. Cancer*, 2006, **94**, 1492–5.
- 329 G. L. Long and J. D. Winefordner, *Anal. Chem.*, 1983, **55**, 712A–724A.
- 330 D. L. Liao, G. S. Wu and B. Q. Liao, *Colloids Surfaces A Physicochem. Eng. Asp.*, 2009, **348**, 270–275.
- 331 J. Nygren, N. Svanvik and M. Kubista, *Doktorsavhandlingar vid Chalmers Tek. Hogsk.*, 1999, 39–51.
- 332 X. Li, J. Qian, L. Jiang and S. L. He, *Appl. Phys. Lett.*, 2009, **94**.
- 333 N. Umetani, J. Kim, S. Hiramatsu, H. A. Reber, O. J. Hines, A. J. Bilchik and D. S. B. Hoon, *Clin. Chem.*, 2006, **52**, 1062–1069.
- 334 B. Taback, S. J. O'Day and D. S. Hoon, *Ann. N. Y. Acad. Sci.*, 2004, **1022**, 17–24.
- 335 H. Schwarzenbach, J. Stoehlmacher, K. Pantel and E. Goekkurt, *Ann. N. Y. Acad. Sci.*, 2008, **1137**, 190–196.
- 336 E. R. Zaher, M. M. Anwar, H. M. a Kohail, S. M. El-Zoghby and M. S. Abo-El-Eneen, *Indian J. Cancer*, 2013, **50**, 175–83.
- 337 N. Umetani, A. E. Giuliano, S. H. Hiramatsu, F. Amersi, T. Nakagawa, S. Martino and D. S. B. Hoon, *J. Clin. Oncol.*, 2006, **24**, 4270–4276.
- 338 G. Sozzi, D. Conte, L. Mariani, S. Lo Vullo, L. Roz, C. Lombardo, M. A. Pierotti and L. Tavecchio, *Cancer Res.*, 2001, **61**, 4675–4678.
- 339 B. Shapiro, M. Chakrabarty, E. M. Cohn and S. a Leon, *Cancer*, 1983, **51**, 2116–2120.
- 340 S. A. Leon, B. Shapiro, D. M. Sklaroff and M. J. Yaros, *Cancer Res.*, 1977, **37**, 646–650.
- 341 A. P. de Silva and S. Uchiyama, *Nat. Nanotechnol.*, 2007, **2**, 399–410.

- 342 A. P. De Silva and N. D. McClenaghan, *Chem. - A Eur. J.*, 2004, **10**, 574–586.
- 343 U. Pischel, *Angew. Chemie - Int. Ed.*, 2007, **46**, 4026–4040.
- 344 X. L. Xu, F. W. Lin, W. Xu, J. Wu and Z. K. Xu, *Chem. - A Eur. J.*, 2015, **21**, 984–987.
- 345 F. Pu, E. Ju, J. Ren and X. Qu, *Adv. Mater.*, 2014, **26**, 1111–1117.
- 346 A. Saghatelian, N. H. Völcker, K. M. Guckian, V. S. Y. Lin and M. R. Ghadiri, *J. Am. Chem. Soc.*, 2003, **125**, 346–347.
- 347 Y. He and H. Cui, *Chem. - A Eur. J.*, 2013, **19**, 13584–13589.
- 348 X. Liu, R. Aizen, R. Freeman, O. Yehezkeli and I. Willner, *ACS Nano*, 2012, **6**, 3553–3563.
- 349 R. Gui, H. Jin, Z. Wang, F. Zhang, J. Xia, M. Yang, S. Bi and Y. Xia, *Nanoscale*, 2015, **7**, 8289–8293.
- 350 B. M. G. Janssen, M. Van Rosmalen, L. Van Beek and M. Merckx, *Angew. Chemie - Int. Ed.*, 2015, **54**, 2530–2533.
- 351 A. Ogawa and M. Maeda, *Chem. Commun.*, 2009, 4666–4668.
- 352 D. Liu, W. Chen, K. Sun, K. Deng, W. Zhang, Z. Wang and X. Jiang, *Angew. Chemie Int. Ed.*, 2011, **50**, 4103–4107.
- 353 J. Du, S. Yin, L. Jiang, B. Ma and X. Chen, *Chem. Commun.*, 2012, 4196–4198.
- 354 Y. Xianyu, Z. Wang, J. Sun, X. Wang and X. Jiang, *Small*, 2014, **10**, 4833–4838.
- 355 Y. Lu and J. Liu, *Acc. Chem. Res.*, 2007, **40**, 315–323.
- 356 Y. Zhang, W. Liu, W. Zhang, S. Yu, X. Yue, W. Zhu, D. Zhang, Y. Wang and J. Wang, *Biosens. Bioelectron.*, 2015, **72**, 218–224.
- 357 R. M. Zadegan, M. D. E. Jepsen, L. L. Hildebrandt, V. Birkedal and J. Kjems, *Small*, 2015, **11**, 1811–1817.
- 358 R. Orbach, B. Willner and I. Willner, *Chem. Commun. (Camb.)*, 2015, **51**, 4144–4160.
- 359 Y. Li, W. Li, K.-Y. He, P. Li, Y. Huang, Z. Nie and S.-Z. Yao, *Nanoscale*, 2016, **8**, 8591–8599.
- 360 V. Kumar, S. Green, G. Stack, M. Berry, J. R. Jin and P. Chambon, *Cell*, 1987, **51**, 941–951.
- 361 C. M. Klinge, *Nucleic Acids Res.*, 2001, **29**, 2905–2919.
- 362 J. A. Edgar, A. M. McDonagh and M. B. Cortie, *ACS Nano*, 2012, **6**, 1116–1125.
- 363 M. Quinten, *J. Clust. Sci.*, 1999, **10**, 319–358–358.
- 364 T. Ung, L. M. Liz-Marzán and P. Mulvaney, *Colloids Surfaces A Physicochem. Eng. Asp.*, 2002, **202**, 119–126.
- 365 S. Yamashita and Y. Okada, *J. Histochem. Cytochem.*, 2005, **53**, 13–21.
- 366 O. D. Velev, E. W. Kaler and A. M. Lenhoff, *Biophys. J.*, 1998, **75**, 2682–2697.

- 367 S. Mosselman, J. Polman and R. Dijkema, *FEBS Lett.*, 1996, **392**, 49–53.
- 368 X. Su, C. Y. Lin, S. J. O’Shea, H. F. Teh, W. Y. X. Peh and J. S. Thomsen, *Anal. Chem.*, 2006, **78**, 5552–5558.
- 369 Z. Cai, G. Chen, X. Huang and M. Ma, *Sensors Actuators, B Chem.*, 2011, **157**, 368–373.
- 370 C. Zhu, L. Liu, Q. Yang, F. Lv and S. Wang, *Chem. Rev.*, 2012, **112**, 4687–4735.
- 371 B. S. Gaylord, A. J. Heeger and G. C. Bazan, *Proc. Natl. Acad. Sci. U. S. A.*, 2002, **99**, 10954–10957.
- 372 Q.-H. Xu, B. S. Gaylord, S. Wang, G. C. Bazan, D. Moses and A. J. Heeger, *Proc. Natl. Acad. Sci. U. S. A.*, 2004, **101**, 11634–9.
- 373 B. S. Gaylord, A. J. Heeger and G. C. Bazan, *J. Am. Chem. Soc.*, 2003, **125**, 896–900.
- 374 X. Duan, Z. Li, F. He and S. Wang, *J. Am. Chem. Soc.*, 2007, **129**, 4154–4155.
- 375 F. Feng, F. He, L. An, S. Wang, Y. Li and D. Zhu, *Adv. Mater.*, 2008, **20**, 2959–2964.
- 376 C. Li, M. Numata, M. Takeuchi and S. Shinkai, *Angew. Chemie - Int. Ed.*, 2005, **44**, 6371–6374.
- 377 X. Liu, Y. Tang, L. Wang, J. Zhang, S. Song, C. Fan and S. Wang, *Adv. Mater.*, 2007, **19**, 1471–1474.
- 378 F. He, Y. Tang, S. Wang, Y. Li and D. Zhu, *J. Am. Chem. Soc.*, 2005, **127**, 12343–12346.
- 379 K. P. Loh, Q. Bao, G. Eda and M. Chhowalla, *Nat. Chem.*, 2010, **2**, 1015–1024.
- 380 X. J. Xing, X. G. Liu, Y. He, Y. Lin, C. L. Zhang, H. W. Tang and D. W. Pang, *Biomacromolecules*, 2013, **14**, 117–123.
- 381 S. He, B. Song, D. Li, C. Zhu, W. Qi, Y. Wen, L. Wang, S. Song, H. Fang and C. Fan, *Adv. Funct. Mater.*, 2010, **20**, 453–459.
- 382 Z. Liu, J. T. Robinson, X. Sun and H. Dai, *J. Am. Chem. Soc.*, 2008, **130**, 10876–10877.
- 383 M. Hassan, M. Walter and M. Moseler, *Phys. Chem. Chem. Phys.*, 2014, **16**, 33–7.
- 384 J. Balapanuru, J. X. Yang, S. Xiao, Q. Bao, M. Jahan, L. Polavarapu, J. Wei, Q. H. Xu and K. P. Loh, *Angew. Chemie - Int. Ed.*, 2010, **49**, 6549–6553.
- 385 F. Li, J. Chao, Z. Li, S. Xing, S. Su, X. Li, S. Song, X. Zuo, C. Fan, B. Liu, W. Huang, L. Wang and L. Wang, *Anal. Chem.*, 2015, **87**, 3877–3883.
- 386 X. Gu, G. Yang, G. Zhang, D. Zhang and D. Zhu, *ACS Appl. Mater. Interfaces*, 2011, **3**, 1175–1179.

- 387 L. Wang, K. Y. Pu, J. Li, X. Qi, H. Li, H. Zhang, C. Fan and B. Liu, *Adv. Mater.*, 2011, **23**, 4386–4391.
- 388 L. Cai, R. Zhan, K. Y. Pu, X. Qi, H. Zhang, W. Huang and B. Liu, *Anal. Chem.*, 2011, **83**, 7849–7855.
- 389 D. S. Latchman, *Int. J. Biochem. Cell Biol.*, 1997, **29**, 1305–1312.
- 390 S. Hori, T. Nomura and S. Sakaguchi, *Science (80-)*, 2003, **299**, 1057–61.
- 391 A. Nepveu, *Gene*, 2001, **270**, 1–15.
- 392 G. M. Cooper and R. E. Hausman, *The Cell: A Molecular Approach*, 2007.
- 393 A. J. Shaywitz and M. E. Greenberg, *Annu. Rev. Biochem.*, 1999, **68**, 821–861.
- 394 S. Shirodkar, M. Ewen, J. A. DeCaprio, J. Morgan, D. M. Livingston and T. Chittenden, *Cell*, 1992, **68**, 157–166.
- 395 S. Gordon, G. Akopyan, H. Garban and B. Bonavida, *Oncogene*, 2006, **25**, 1125–1142.
- 396 S. Safe and M. Abdelrahim, *Eur. J. Cancer*, 2005, **41**, 2438–2448.
- 397 M. W. Mayo and A. S. Baldwin, *Biochim. Biophys. Acta*, 2000, **1470**, M55–M62.
- 398 J. J. Schott, D. W. Benson, C. T. Basson, W. Pease, G. M. Silberbach, J. P. Moak, B. J. Maron, C. E. Seidman and J. G. Seidman, *Science (80-)*, 1998, **281**, 108–111.
- 399 C. Guijarro and J. Egido, *Kidney Int.*, 2001, **59**, 415–424.
- 400 P. J. Barnes and M. Karin, *N. Engl. J. Med.*, 1997, **336**, 1066–1071.
- 401 D. A. van Heel, I. A. Udalova, A. P. De Silva, D. P. McGovern, Y. Kinouchi, J. Hull, N. J. Lench, L. R. Cardon, A. H. Carey, D. P. Jewell and D. Kwiatkowski, *Hum. Mol. Genet.*, 2002, **11**, 1281–1289.
- 402 Y. N. Tan, X. Su, E. T. Liu and J. S. Thomsen, *Anal. Chem.*, 2010, **82**, 2759–2765.
- 403 F. Li, H. Pei, L. Wang, J. Lu, J. Gao, B. Jiang, X. Zhao and C. Fan, *Adv. Funct. Mater.*, 2013, **23**, 4140–4148.
- 404 J. S. Carroll, X. S. Liu, A. S. Brodsky, W. Li, C. A. Meyer, A. J. Szary, J. Eeckhoutte, W. Shao, E. V. Hestermann, T. R. Geistlinger, E. A. Fox, P. A. Silver and M. Brown, *Cell*, 2005, **122**, 33–43.
- 405 S. K. Tan, Z. H. Lin, C. W. Chang, V. Varang, K. R. Chng, Y. F. Pan, E. L. Yong, W. K. Sung, W. K. Sung and E. Cheung, *EMBO J.*, 2011, **30**, 2569–81.
- 406 L. J. Ou, P. Y. Jin, X. Chu, J. H. Jiang and R. Q. Yu, *Anal. Chem.*, 2010, **82**, 6015–6024.
- 407 R. S. Dias and B. Lindman, *DNA Interactions with Polymers and Surfactants*, Wiley-Interscience, Hoboken, New Jersey, 2007.
- 408 Y. Wang, Z. Li, J. Wang, J. Li and Y. Lin, *Trends Biotechnol.*, 2011, **29**, 205–

- 212.
- 409 Cell Signaling Technology, FoxA1 (Human), <http://www.phosphosite.org/proteinAction?id=14681&showAllSites=true> .
- 410 Cell Signaling Technology, AP-2 gamma (Human), <http://www.phosphosite.org/proteinAction?id=2411101&showAllSites=true> .
- 411 B. J. Cheskis, S. Karathanasis and C. R. Lyttle, *J. Biol. Chem.*, 1997, **272**, 11384–11391.
- 412 J. Liu, S. Fu, B. Yuan, Y. Li and Z. Deng, *J. Am. Chem. Soc.*, 2010, **132**, 7279–7281.
- 413 W. A. Lea and A. Simeonov, *Expert Opin. Drug Discov.*, 2011, **6**, 17–32.
- 414 K. M. M. Aung, S. Y. New, S. Hong, L. Sutarlie, M. G. L. Lim, S. K. Tan, E. Cheung and X. Su, *Anal. Biochem.*, 2014, **448**, 95–104.
- 415 P. Yi, M. D. Driscoll, J. Huang, S. Bhagat, R. Hilf, R. A. Bambara and M. Muyan, *Mol. Endocrinol.*, 2002, **16**, 674–693.
- 416 C. J. Murphy, T. K. San, a M. Gole, C. J. Orendorff, J. X. Gao, L. Gou, S. E. Hunyadi and T. Li, *J. Phys. Chem. B*, 2005, **109**, 13857–13870.
- 417 J. R. Windmiller and J. Wang, *Electroanalysis*, 2013, **25**, 29–46.
- 418 A. J. Bhandodkar and J. Wang, *Trends Biotechnol.*, 2014, **32**, 363–371.
- 419 P. Anzenbacher, F. Li and M. A. Palacios, *Angew. Chemie - Int. Ed.*, 2012, **51**, 2345–2348.
- 420 P. S. Mitchell, R. K. Parkin, E. M. Kroh, B. R. Fritz, S. K. Wyman, E. L. Pogossova-Agadjanyan, A. Peterson, J. Noteboom, K. C. O'Briant, A. Allen, D. W. Lin, N. Urban, C. W. Drescher, B. S. Knudsen, D. L. Stirewalt, R. Gentleman, R. L. Vessella, P. S. Nelson, D. B. Martin and M. Tewari, *Proc. Natl. Acad. Sci. U. S. A.*, 2008, **105**, 10513–8.
- 421 D. Duijvesz, T. Luider, C. H. Bangma and G. Jenster, *Eur. Urol.*, 2011, **59**, 823–831.
- 422 M. Cristofanilli, G. T. Budd, M. J. Ellis, A. Stopeck, J. Matera, M. C. Miller, J. M. Reuben, G. V Doyle, W. J. Allard, L. W. M. M. Terstappen and D. F. Hayes, *N. Engl. J. Med.*, 2004, **351**, 781–91.
- 423 C. Bettegowda, M. Sausen, R. J. Leary, I. Kinde, Y. Wang, N. Agrawal, B. R. Bartlett, H. Wang, B. Luber, R. M. Alani and others, *Sci. Transl. Med.*, 2014, **6**, 224ra24–224ra24.

